Dissertation in Astronomy

# Using astrophotonics to design new components for future telescopes

By

Theodoros Anagnos

Thesis Supervisors:
Prof. Dr. Andreas Quirrenbach
Dr. Robert J. Harris &
Dr. Christian Schwab

Thesis dissertation members:
Prof. Dr. Andreas Quirrenbach
Prof. Dr. Jochen Heidt
Associate Prof. Dr. Alex Fuerbach
Prof. Dr. Björn Malte Schäfer
PD. Dr. Christian Fendt

A thesis submitted to,
the Combined Faculties of the Natural Sciences and Mathematics
of Heidelberg University, Germany
for the degree of Doctor of Natural Sciences
and
the Macquarie University, Department of Physics and Astronomy, Australia,
for the degree of Doctor of Philosophy

27 April 2020

# Abstract

With the Extremely Large Telescopes (ELTs) currently under construction we are entering a new era of challenging requirements, which drive spectrograph designs towards techniques that more efficiently use a facility's light feed. If the spectrograph can operate close to the diffraction limit, this reduces the footprint of the instrument compared to a conventional high resolution spectrograph and mitigates problems and cost issues caused by the use of large optics. By using adaptive optics (AO) to address the wavefront distortions caused by the Earth's atmospheric turbulence, we can provide diffraction-limited starlight to the telescope's focal plane. Using astrophotonic spatial reformatters and custom optical fibers to manage the AO output, we can increase the starlight coupled into the instrument. In the first part of the thesis, simulation models are compared to manufactured and on-sky tested astrophotonic reformatters. Re-designing of the structures allowed their simulated performance to be further optimised. This is complemented by the laboratory characterisation of multiple different reformatters. In the second part of the thesis, everything discussed thus far is combined, leading to the design, manufacture and on-sky test of a novel instrument concept. This new instrument is composed of a multi-core fiber (MCF) with 3D printed micro-optics on its cores, which increase the coupling of light into them. The custom fiber is used to feed starlight from the Subaru Coronagraphic Extreme Adaptive Optics (SCExAO) instrument at the 8.2 m Subaru telescope in Hawaii to a diffraction-limited high resolution spectrograph. The results are promising and highlight the instrument's potential to change the paradigm with which high resolution spectrographs are built, in particular in the near infrared (NIR), for telescopes equipped with powerful AO systems. This study complements recent work in the field and provides crucial insight for optimising future astrophotonic devices.

# Zusammenfassung

In der neuen Ära von extrem großen Teleskopen die sich derzeit im Bau befinden, treiben die extremen Anforderungen das Design von Spektrographen in Richtung von Technologien, die das vorhandene Licht am effizientesten nutzen. Der Betrieb nahe der Beugungsgrenze reduziert den Platzbedarf eines Instruments im Vergleich zu einem herkömmlichen Spektrographen mit hohem Auflösungsvermögen und verringert Probleme und Kosten, die durch die Verwendung großer Optiken andernfalls verursacht werden. Wellenfrontfehler durch atmosphärische Turbulenzen auf der Erde können mit adaptiver Optik behoben werden; solche Systeme stellen beugungsbegrenzte Abbildungen von Sternen für angeschlossene Instrumente bereit. Dies verringert die scheinbare Größe eines punkförmigen Objekts, da die Anzahl der räumlichen Lichtmoden reduziert wird. Durch die Verwendung von astrophotonischen räumlichen Reformatierern und maßgeschneiderten optischen Fasern die an die AO gekoppelt sind, kann die Einkopplungseffizienz von Sternenlicht in das Instrument wesentlich verbessert werden. Im ersten Teil der Arbeit werden Simulationsmodelle mit vorhandenen und am Himmel getesteten astrophotonischen Reformatierern verglichen. Die geometrische Neugestaltung der Strukturen ermöglichte es, deren simulierte Leistung weiter zu optimieren. Dies wird ergänzt durch die Laborcharakterisierung mehrerer verschiedener Reformatierer. Im zweiten Abschnitt der Dissertation wurde alles bisher Besprochene kombiniert, was zur Konstruktion, Herstellung und on-sky Tests eines neuartigen Instrumentenkonzepts führte. Dieses neue Instrument besteht aus einer Mehrkernfaser mit 3D-gedruckter Mikrooptik auf seinen Kernen, welche den Wirkungsgrad der Lichtkopplung erhöht. Diese maßgeschneiderten Fasern werden verwendet um Sternenlicht vom SCExAO System am Subaru 8,2 m Teleskop einem beugungsbegrenzten Spektrographen mit hohem Auflösungsvermögen zuzuführen. Die Ergebnisse am Himmel sind vielversprechend und unterstreichen das Potenzial des Instruments. Diese Studie ergänzt die jüngsten Forschungsarbeiten auf diesem Gebiet und zeigt entscheidende Erkentnisse für die Optimierung zukünftiger astrophotonischer Geräte.

# Statement of Originality

This thesis is being submitted to Macquarie University and Heidelberg University in accordance with the Cotutelle agreement dated 27.4.2020.

To the best of my knowledge and belief, the thesis contains no material previously published or written by another person except where due reference is made in the thesis itself.

Theodoros Anagnos

## Publications

### Journal (peer reviewed)

**2020**

1. **Th. Anagnos**, M. Trappen, B. C. Kuo Tiong, T. Feger, S. Yerolatsitis, R. J. Harris, S. Vievard, J. Lozi, T. A. Birks, N. Jovanovic, O. Guyon, I. Gris-Sánchez, S. G. Leon-Saval, B. Norris, M. Blaicher, Y. Xu, C. Betters, C. Koos, D. W. Coutts, C. Schwab & A. Quirrenbach, *"First on-sky demonstration of the 3D-printed Mono-Mode Multi-core fiber spectrograph (3D-M3)"*, 2020, MNRAS, in prep..
2. S. Y. Haffert, R. J. Harris, A. Zanutta, F. A. Pike, A. Bianco, E. Redaelli, A. Benot, D. G. MacLachlan, C. A. Ross, I. Gris-Sánchez, M. Trappen, Y. Xu, M. Blaicher, P. Maier, G. Riva, C. Kulcsár, N. A. Bharmal, E. Gendron, L. Staykov, T. J. Morris, S. Barboza, N. Muench, L. Bardou, L. Prengere, H. F. Raynaud, P. Hottinger, **T. Anagnos**, J. Osborn, C. Koos, R. R. Thomson, T. A. Birks, I. Snellen, and C. Keller, *"The Multi-Core fiber-fed Integral-Field Unit (MCIFU) I. A diffraction-limited integral-field spectrograph for extreme adaptive optics systems."*, 2020, in prep..
3. **Th. Anagnos**, T. Feger, S. Gross, R. J. Harris, I. Spaleniak1, N. Jovanovich, B. C. Kuo Tiong, A. Quirrenbach, D. W. Couts, C. Schwab, & M. J. Withford, *"Broadband characterisation of astrophotonic spatial reformatter for diffraction-limited spectroscopy"*, 2020, MNRAS, in prep..

**2018**

1. **Th. Anagnos**, R. J. Harris, M. K. Corrigan, A. P. Reeves, M. J. Townson, D. G. MacLachlan, R. R. Thomson, T. J. Morris, C. Schwab, A. Quirrenbach, *"Simulation and Optimization of an Astrophotonic Reformatter"*, 2018, MNRAS, 478, 4881.

## Proceedings

### Peer reviewed

**2018**

1. R. J. Harris, **Th. Anagnos** and P. Hottinger, *"Astrophotonic technologies for small telescopes"*, Contrib. Astron. Obs. Skalnaté Pleso 49, 119-124, 2019, (`https://www.ta3.sk/caosp/Eedition/FullTexts/vol49no2/pp119-124.pdf`).

### Not peer reviewed

**2020**

1. **Th. Anagnos** et al., *"An innovative fiber injection system upgrade with 3D-printed microlenses for the RHEA at Subaru"*, 2020, Proc. SPIE, in prep..

**2018**

1. **Th. Anagnos**, R. J. Harris, M. K. Corrigan, A. P. Reeves, M. J. Townson, D. G. MacLachlan, R. R. Thomson, T. J. Morris, C. Schwab, A. Quirrenbach, *"Optimizing astrophotonic spatial reformatters using simulated on-sky performance"*, 2018, Proc. SPIE, 10706, 107062H
2. M. K. Corrigan, T. J. Morris, R. J. Harris, **Th. Anagnos**, *"Demonstration of a photonic lantern low order wavefront sensor using an adaptive optics testbed"*, 2018, Proc. SPIE, 10703, 107035H.
3. R. J. Harris, J. Tepper, J. J. Davenport, E. Pedretti, D. M. Haynes, P. Hottinger, **Th. Anagnos**, A. Shankar Nayak, Y. Herrero Alonso, P. Jyoti Deka, S. Minardi, A. Quirrenbach, L. Labadie and R. Haynes, *"NAIR: Novel Astronomical Instrumentation through photonic Reformatting"*, 2018, Proc. SPIE, 10706, 107060L.

"The copyright of this thesis rests with the author. Information derived from it should be acknowledged".

# Acknowledgements

Here I wish to express how grateful I am that I've met many people over my Ph.D journey and had an awesome time with them. It is rather hard to do so in only one page and for anybody I end up missing I am truly sorry. My supervisors Prof. Andreas Quirrenbach, Dr. Robert J. Harris and Dr. Christian Schwab, for the countless meetings and discussions improving my projects. Rob, my supervisor but mostly my friend, for his enormous patience in repeating advice and his crucial feedback for my work. To Prof. apl. Christian Fendt who always offered his help as a scientific coordinator of IMPRS-HD. To my mates and colleagues at MQ, Tobi and Blaise, who really help a lot to keep the ball rolling and had an awesome year spent together in Oz. To Olivier, Nem, Julien, Seb, the cool SCExAO team for giving me the chance to use their state-of-the-art instrument. To Diana, Katy, Melanie and Sarah who had the patient and kindness to proof red my thesis and improve it. To all of my colleagues-friends in LSW and MQ giving me advice along my PhD and we had really a blast together. To my bachelor thesis supervisor, emeritus Prof. John H. Seiradakis, who was my inspiration to get into astronomy and continue, but unfortunately he is not with us anymore. To my father and my partner for their ever there support and finally to anybody I've missed, accept my apologies.

*To the people who share their knowledge*

# Acronyms

**AO** adaptive optics

**BPM** beam propagation method

**EE** ensquared energy

**ELT** Extremely Large Telescope

**ExAO** extreme adaptive optics

**FBG** fiber bragg grating

**FOV** field of view

**FRD** focal ratio degradation

**FSR** free spectral range

**FWHM** full width half maximum

**GUI** graphical user interface

**HR** hybrid reformatter

**IFS** integral field spectroscopy

**IFU** integral field unit

**IRD** InfraRed Doppler spectrograph

**LBT** Large Binocular Telescope

**LED** light-emitting diode

**mas** milli-arcseconds

**MCF** multi-core fiber

**MFD** mode field diameter

**MLA** micro-lens array

| | |
|---|---|
| **MMF** | multi-mode fiber |
| **MM** | multi-mode |
| **NIR** | near infrared |
| **NA** | numerical aperture |
| **OAP** | off-axis parabola |
| **PD** | photonic dicer |
| **PGMEA** | propylene-glycol-methyl-ether-acetate |
| **PIAA** | Phase-Induced Amplitude Apodization |
| **PL** | photonic lantern |
| **PSF** | point spread function |
| **PyWFS** | pyramid wavefront sensor |
| **QE** | quantum efficiency |
| **RHEA** | Replicable High-resolution Exoplanet and Asteroseismology Spectrograph |
| **RMS** | root-mean-square |
| **RV** | radial velocity |
| **SCExAO** | Subaru Coronagraphic Extreme Adaptive Optics |
| **SEM** | scanning electron microscopy |
| **SNR** | signal to noise ratio |
| **SMF** | single-mode fiber |
| **SM** | single-mode |
| **TE** | transverse electric |
| **TM** | transverse magnetic |
| **ULI** | ultra-fast laser inscription |

**VPH** volume phase holographic

**VSI** vertically-scanned white-light interferometry

**WFS** wavefront sensor

**WHT** William Herschel Telescope

**3D-M3** 3D-printed Mono-Mode Multi-core fiber spectrograph

# Contents

**Abstract** **i**

**Statement of Originality** **ii**

**Acknowledgements** **vii**

**1 Prolegomenon** **1**

1.1 Outline . . . . . . . . . . . . . . . . . . . . . . . . . . . . . . . . . . . 1

**2 Background Theory** **3**

2.1 Introduction . . . . . . . . . . . . . . . . . . . . . . . . . . . . . . . . 3

2.2 Motivation . . . . . . . . . . . . . . . . . . . . . . . . . . . . . . . . . 3

2.3 Principles of spectroscopy . . . . . . . . . . . . . . . . . . . . . . . . 6

2.4 Astrophotonics . . . . . . . . . . . . . . . . . . . . . . . . . . . . . . . 15

2.4.1 Optical fibers: Basic properties . . . . . . . . . . . . . . . . . . . 15

2.4.2 Fibers in instrumentation . . . . . . . . . . . . . . . . . . . . . . 18

2.4.3 Spatial reformatters . . . . . . . . . . . . . . . . . . . . . . . . . 25

2.4.4 Propagated light simulation - wave model analysis . . . . . . . . . . . . . 29

**3 The photonic dicer** **31**

3.1 Methods . . . . . 32

3.1.1 `Soapy` Configuration . . . . . 32

3.1.2 `BeamPROP` Configuration . . . . . 33

3.1.3 Throughput calculation . . . . . 36

3.1.4 Photonic dicer plane optimisation . . . . . 37

3.2 Results . . . . . 37

3.2.1 Throughput performance results . . . . . 37

3.2.2 Optimisation results . . . . . 43

3.2.3 Modal noise results . . . . . 44

3.3 Discussion . . . . . 46

3.3.1 Adaptive Optics performance . . . . . 46

3.3.2 F-ratio calibration . . . . . 46

3.3.3 Evanescent field coupling . . . . . 47

3.3.4 Modal noise . . . . . 49

3.4 Conclusions . . . . . 51

**4 The Hybrid reformatter** **53**

4.1 Methods . . . . . 54

4.1.1 `Soapy` set-up . . . . . 54

4.1.2 `BeamPROP` set-up . . . . . 55

4.1.3 Throughput measurement . . . . . 57

4.2 Simulation results . . . . . 57

4.2.1 Output power performance results . . . . . . . . . . . . . . . . . . . . . . . 57

4.2.2 Optimisation results . . . . . . . . . . . . . . . . . . . . . . . . . . . . . . . 59

4.2.3 Modal noise results . . . . . . . . . . . . . . . . . . . . . . . . . . . . . . . 59

4.3 Discussion . . . . . . . . . . . . . . . . . . . . . . . . . . . . . . . . . . . 61

4.3.1 Throughput performance . . . . . . . . . . . . . . . . . . . . . . . . . . . . 61

4.3.2 Coupling of evanescent field . . . . . . . . . . . . . . . . . . . . . . . . . . 61

4.3.3 Modal noise . . . . . . . . . . . . . . . . . . . . . . . . . . . . . . . . . . . 62

4.4 Conclusions . . . . . . . . . . . . . . . . . . . . . . . . . . . . . . . . . . 64

**5 Astrophotonic reformatters in the visible spectral band 65**

5.1 Methods . . . . . . . . . . . . . . . . . . . . . . . . . . . . . . . . . . . . 66

5.1.1 Setup architecture . . . . . . . . . . . . . . . . . . . . . . . . . . . . . . . 66

5.1.2 Inscribed devices architecture . . . . . . . . . . . . . . . . . . . . . . . . . 66

5.1.3 Fabrication process . . . . . . . . . . . . . . . . . . . . . . . . . . . . . . . 69

5.1.4 Throughput measurement setup . . . . . . . . . . . . . . . . . . . . . . . . 69

5.2 Results . . . . . . . . . . . . . . . . . . . . . . . . . . . . . . . . . . . . . 72

5.2.1 Data acquisition and reduction . . . . . . . . . . . . . . . . . . . . . . . . 72

5.2.2 Laboratory throughput results . . . . . . . . . . . . . . . . . . . . . . . . . 74

5.2.3 Astrophotonic reformatters – Optimising the pitch . . . . . . . . . . . . . 77

5.2.4 Optimising the transition reformatting plane length . . . . . . . . . . . . 77

5.2.5 Optimising the off-axis lateral step devices . . . . . . . . . . . . . . . . . 78

5.2.6 Simulated `BeamPROP` comparison . . . . . . . . . . . . . . . . . . . . . . 79

5.3 Discussion . . . . . . . . . . . . . . . . . . . . . . . . . . . . . . . . . . . 80

5.3.1 Multi-mode waveguide performance . . . . . . . . . . . . . . . . . . . . . . 80
5.3.2 Butt-coupled fiber into the astrophotonic reformatter . . . . . . . . . . . 83
5.4 Conclusions . . . . . . . . . . . . . . . . . . . . . . . . . . . . . . . . . . . . 84

**6 3D-printed Mono-Mode Multi-core fiber spectrograph (3D-M3) 85**

6.1 Methods . . . . . . . . . . . . . . . . . . . . . . . . . . . . . . . . . . . . . . 86
6.1.1 Instrument architecture . . . . . . . . . . . . . . . . . . . . . . . . . . . 86
6.1.2 The SCExAO infrastructure . . . . . . . . . . . . . . . . . . . . . . . . . 88
6.1.3 Simulations . . . . . . . . . . . . . . . . . . . . . . . . . . . . . . . . . . 89
6.1.4 Micro-optics manufacturing process . . . . . . . . . . . . . . . . . . . . 89
6.1.5 Fibre injection unit . . . . . . . . . . . . . . . . . . . . . . . . . . . . . 91
6.1.6 Throughput setup . . . . . . . . . . . . . . . . . . . . . . . . . . . . . . . 92
6.1.7 Spectroscopic setup . . . . . . . . . . . . . . . . . . . . . . . . . . . . . . 93
6.2 Results . . . . . . . . . . . . . . . . . . . . . . . . . . . . . . . . . . . . . . . 94
6.2.1 Laboratory throughput results . . . . . . . . . . . . . . . . . . . . . . . 94
6.2.2 On-sky spectroscopic results . . . . . . . . . . . . . . . . . . . . . . . . 97
6.2.3 Adaptive optics performance . . . . . . . . . . . . . . . . . . . . . . . . . 102
6.3 Discussion . . . . . . . . . . . . . . . . . . . . . . . . . . . . . . . . . . . . . 106
6.3.1 Opto-mechanical parts limitations . . . . . . . . . . . . . . . . . . . . . . 106
6.4 Conclusions . . . . . . . . . . . . . . . . . . . . . . . . . . . . . . . . . . . . 106

**7 Conclusions and future work 108**

7.1 Synopsis . . . . . . . . . . . . . . . . . . . . . . . . . . . . . . . . . . . . . . 108
7.2 Further Work . . . . . . . . . . . . . . . . . . . . . . . . . . . . . . . . . . . 110

# List of Tables

3.1 Simulation `Soapy` input parameters . . . 34

3.2 Comparison of ULI inscription parameters used in Thomson et al. and Harris et al. . . . 35

3.3 Simulation domain initial parameters of `RSoft` for the photonic dicer (PD). . . . 36

3.4 Fractional throughput results comparing theoretical simulations and on-sky conditions. The incorrect results for real measured input data + `BeamPROP` show a factor of two overestimation because `BeamPROP` assumes zero phase if phase information is not provided; this highlights the importance of having phase information of the input beam in the simulations. . . . 42

3.5 Evanescent field contribution results (See section 3.3.3) . . . 47

4.1 `Soapy` input parameters for simulation . . . 55

4.2 Comparison of ULI inscription parameters used in Thomson et al. (2011) and MacLachlan et al. (2017). . . . 56

4.3 Percentage results of throughput from simulations in comparison with the on-sky conditions. . . . 61

5.1 Internal configuration parameters for both of the optical chips. See figure 5.2 for a visual representation. . . . 68

5.2 Table of the optical components used on the lab characterisation. All listed parts are from the Thorlabs online catalogue. . . . 71

5.3 Throughput performance of the chip#1 at the wavelengths of 600 and 800 nm. . 75

5.4 Throughput performance of the chip#2 at the wavelengths of 600 and 800 nm. . 75

# List of Figures

2.1 Illustration of a conventional astronomical spectrograph design. The starlight is focused by the telescope ($D_{\mathrm{Tel}}$) onto the entrance slit ($D_{\mathrm{Slit}}$) of the spectrograph, where it is collimated by an optic and chromatically dispersed by the diffraction grating. After that, the starlight is focused down to the detector by another optic ($L_{\mathrm{Cam}}$). . . . . . . . . . . . . . . . . . . . . . . . . . . . . . . . . 7

2.2 Example of **(left)** a non-blazed diffraction grating where the grooves are placed in parallel with the phase of the grating where the most of the energy is concentrated at the zeroth order. **(right)** A blazed reflective diffraction grating where the grooves are inclined by the blaze angle $\theta_{\mathrm{B}}$ with respect to the grating face where the majority of the energy is concentrated towards higher orders. Figures include the light rays path before and after the grating. . . . . . . . . . . . . . . 9

2.3 Illustration example of the angular ($d\beta/d\lambda$) and linear ($dx/d\lambda$) dispersion of a transmission grating. . . . . . . . . . . . . . . . . . . . . . . . . . . . . . 10

2.4 Schematic presentation of the free spectral range (FSR) concept. The top panel (a) shows the spectrum of a conventional spectrograph as in Figure 2.1, where the orders overlap near their edges. The middle panel (b) shows the same spectrum as before but separates each order to highlight the overlapped regions of the spectrum. The bottom panel (c) illustrates the output spectrum of an échelle spectrograph using another dispersing element (grating, prism) used for cross-dispersion of the orders, such that no overlap is happening. . . . . . . . . . . . 12

2.5 Example architecture of an échelle spectrograph using a prism as cross-disperser. 13

2.6 Illustration of various types of integral field spectroscopy (IFS) systems with their corresponding output spectra. All 4 methods produce a datacube with position and spectrum information. Image courtesy Allington-Smith & Content. 14

2.7 Illustration of a typical multi-mode fiber (MMF) cross section, with a top-hat refractive index profile. numerical aperture (NA) is also manifested in the figure. 16

2.8 Illustration of focal ratio ($f/\#$) of a lens. . . . . . . . . . . . . . . . . . . . . . . . 18

2.9 Graphical illustration of the intensity of the (a) $transverseelectric(\mathrm{TE})_{PL}$ modes of a circular and (b) $\mathrm{TE}_{MN}$ modes of a square profile waveguide (Wikipedia 2019). Below each mode pattern the $P$ and $L$ number are given. These stand for the number of half-wavelengths along the radius and half-perimeter correspondingly for the circular waveguide and along the width and height correspondingly for the square waveguide. transverse magnetic (TM) modes are the same but rotated by 90°. . . . . . . . . . . . . . . . . . . . . . . . . . . . . . . . . . . 21

2.10 Illustration of focal ratio degradation (FRD) issue for the case of (a) an ideal fiber, and (b) for a MMF with FRD, making the output light-cone (right-one) wider than the entrance one (left-one). Image courtesy: Dr. Tobias Feger. . . . . 22

2.11 Illustration of FRD effect compared to an ideal MMF (NA=0.25) without it. The deviation of the output $f/\#$ as a function of injected $f/\#$ into the fiber is larger for a slower injected beam. Image courtesy: Barden et al.. . . . . . . . . . 23

2.12 Graphical illustration of (a) the position of the injected beam to a typical MMF (Thorlabs - AFS105/125),(b) fiber near-field output with poor scrambling, (c) fiber near-field output with better scrambling. Image courtesy Olaya et al. (2012). 24

2.13 Illustration of a photonic lantern (PL) where the multi-mode (MM) input, the transition zone and the single-mode (SM) sections are presented. Image courtesy: Birks et al. (2015). . . . . . . . . . . . . . . . . . . . . . . . . . . . . . . . . . 26

2.14 (a) Illustration of a PL pair connected back-to-back together, having their MM cross-sections at the input and the output, while in between them, fiber bragg grating (FBG) filters are inscribed into the single-mode fibers (SMFs). (b) Example of a Chinese paper lantern. Image courtesy: Birks et al. (2015) . . . . . . 27

2.15 Illustration of (a) a PL manufactured by tapering down individual SMFs surrounded by a lower refractive index tube, (b) Micrographs of the built PL at different cross-sections along the taper transition, where the seven individual fibers are distinguished at the leftmost frame while on the rightmost the have merged together to form the MM input, (c) cross-section of a 1×7 tapered-down coupler. Images courtesy: Birks et al. (2015). . . . . . . . . . . . . . . . . . . . 28

2.16 Illustration of (a) the ultra-fast laser inscription (ULI) method where the created waveguides are represented with blue colour, (b) (left) the PL manufactured by Thomson et al. (2011) with 16-waveguides in a square formation and (right) two identical PLs connected back-to-back. Image courtesy: Birks et al. (2015). . . . 28

3.1 Illustration of the `Soapy` graphical user interface (GUI) including description of its individual display panels. Image courtesy: Reeves (2016). . . . . . . . . . . . 33

3.2 Illustration of the photonic dicer structure as it appears in `RSoft` CAD. . . . . . 34

3.3 Colour map showing the refractive index profile of a noisy waveguide of the photonic dicer. . . . . . . . . . . . . . . . . . . . . . . . . . . . . . . . . . . . 35

3.4 The photonic dicer 3D design in the `RSoft` CAD environment. The colours indicate the 5 different transition planes used to reform the square input (green colour) to a linear slit output (grey colour). . . . . . . . . . . . . . . . . . . . . . 36

3.5 Graphical illustration of Soapy output beam to the square entrance of the photonic dicer (red square) at the right side of the sub-frames, with its corresponding slit output of photonic dicer on the left of the sub-frames, (a-b) with close-loop AO correction at two different times, (c-d) same as before but for the case of open-loop correction AO mode. Colours indicate the relative normalised intensity of the light. . . . . . . . . . . . . . . . . . . . . . . . . . . . . . . . . . . . 38

3.6 Graphical illustration of light propagation through the photonic dicer as displayed by `RSoft`'s simulation CAD environment. (a-b) cross-section of photonic dicer plane where the waveguides reform towards a linear array output (see Figure 3.4), (c-d) Top and side view of the same simulation as the light propagates on the z-axis. Colours indicate the relative normalised intensity here. . . . . . . 39

3.7 Histogram plot of throughput measurements in the three different AO modes, with each mode containing 12,000 simulation results binned by a factor of 60. In order of correction, red shows closed-loop, green tip-tilt correction and blue shows open-loop. . . . . . . . . . . . . . . . . . . . . . . . . . . . . . 40

3.8 Throughput measurements of the simulated photonic dicer slit end versus the amount of light coupled at 321 mas (the square entrance of the device as configured in `BeamPROP`). This is shown for the simulated data of `Soapy` (bold colour) and on-sky results (transparent) in all three AO operating modes. Note that the number of points are binned by a factor of 60 into 200 points from the 12,000, for each AO mode. . . . . . . . . . . . . . . . . . . . . . . . . . . . . . 41

3.9 The relation of closed-loop and tip-tilt AO mode ratios of ensquared energy as a function of spatial scale (square box centred), plotted for both simulated (`Soapy`) and on-sky averaged data (real). The photonic dicer square entrance size is represented by the blue vertical line. . . . . . . . . . . . . . . . . . . . . . . . 42

3.10 Co-added computed power enclosed inside the 36 waveguides as a function of the propagating length. Vertical solid black lines indicate the 5 transition planes of the device as it was originally built, and vertical dashed black lines represent the optimised locations of the planes. This is shown for the three AO operating modes in three different colours (constant lines for default photonic dicer (a) and dashed lines (b) for the optimised version correspondingly). Computed powers are normalised according to the maximum of each AO modes. Averaged frames of all three AO modes were used as an input. Power fluctuations are discussed in section 3.3.3. . . . . . . . . . . . . . . . . . . . . . . . . . . . . . 43

3.11 Top panel: Near field averaged image (intensity) of the slit from `BeamPROP` simulations (@1550 nm). Middle panel: MFD of the slit profile including 1$\sigma$ errors from individual frames. Bottom panel: Near field barycentre shifts across the slit. 44

3.12 Throughput performance of the photonic dicer as a function of wavelength for low spectral resolution scanning with steps of 0.1 nm (R $\sim$ 15,500), and high spectral resolution scanning with steps of 0.01 nm (R $\sim$ 155,000). **Inset:** High spectral resolution magnified. . . . . . . . . . . . . . . . . . . . . . . . . . . 45

3.13 (a-c) Colour map images (logarithm of intensities) of the `Soapy` closed AO mode input data at the left together with the corresponding reformatted output of the photonic dicer at the right, for 3 different ensquared energy coupled to device spatial simulation domain, ((a) - full field) and ((b) - cut field) 42.05 % of the full frame, ((c) - cut-inside field) 57.94 % of the full frame. The simulated spatial domain for each of the 6 frames is 438×138 μm. . . . . . . . . . . . . . . . . . . 48

3.14 Top panel: Near field averaged image (intensity) of the separated slit from `BeamPROP` simulations. Middle panel: MFD of the slit profile including 1$\sigma$ errors from individual frames. Bottom panel: Measurements of barycentre movement across the slit from individual frames. . . . . . . . . . . . . . . . . . . . . . . . . 50

3.15 Top panel: Typical near field image of the 50 μm MMF output from `BeamPROP` simulations. Bottom panel: Measurements of barycentre movement along the fibre y-axis (blue) and x-axis (red) from individual frames. . . . . . . . . . . . . 51

4.1 The Hybrid Reformatter's 3D structure, without the initial photonic lantern section included in the plot as visualised in the `RSoft`'s CAD environment. The colours show the 3 different transition planes used. . . . . . . . . . . . . . . . . 56

4.2 Histogram distribution of throughput measurements from simulations shown for three different AO modes. Red colour represents the closed-loop AO mode of correction, green shows the tip-tilt correction and blue shows open-loop correction. 58

4.3 The distribution of closed-loop and tip-tilt AO mode ensquared energy ratios as a function of the entrance's spatial scale (circular radius centred), plotted for simulated (`Soapy`) averaged (Intensity) data. The vertical blue line represents the circular entrance size of the PL section of the hybrid reformatter (HR). . . . 58

4.4 Top: Averaged (intensity) near-field images of the slit output from `BeamPROP` simulations (@1550 nm). Middle: mode field diameter (MFD) profile size measurements of the slit with 1$\sigma$ errors from the individual images. Bottom: Barycentric variations across the slit of the device calculated from the dataset. . . . . . . . 60

4.5 **(a)**: Top panel: Typical near-field image (intensity) of the 8.2 μm single-mode fiber output from `BeamPROP` simulations. Bottom panel: Barycentric movement measurements along the fiber x-axis (red) and y-axis (blue) derived from individual images. **(b)**: Top panel: Common near-field image (intensity) of the 50 μm octagonal fiber output from `BeamPROP` simulations. Bottom panel: Barycentric movement measurements along the fiber x-axis (red) and y-axis (blue) derived from individual images. . . . . . . . . . . . . . . . . . . . . . . . . . . . . . . 63

5.1 Instrument schematic concept composed of an SMF-28, the astrophotonic reformatter and the spectrograph. Image adapted from Tobias Feger. . . . . . . . . 67

5.2 Laser inscribed astrophotonic components layout inside the two optical chip substrates. M1-4 represent the position reference marks, MM is the linear compilation of the SM waveguides in a pentagon formation, RF1-4 are the photonic reformatters with a combination of different pitch in input and output plane of their individual waveguides, RF5-8 stand for the photonic reformatters with a different length in transition final plane (Δy) towards the slit output and RF9-11 stand for the devices with a lateral displacement step from their on-axis entrance plane (Δx). All the components are inscribed at a depth of D = 200 μm (internal configuration parameters of the devices are listed in Table 5.1.) . . . . . . . . . . 68

5.3 Microscope image of the input-output plane of the inscribed substrates (Eagle2000 glass) featuring five inscribed devices fabricated and characterised. In this chip#2 the individual SM waveguides were written with 40 nJ pulse energy with a translation speed of 500 mm/minute. . . . . . . . . . . . . . . . . . . . . . 70

5.4 Schematic illustration of the throughput test apparatus for the optical chip substrates. An SMF-28 fiber was used to transfer light from the light source to the optical chip. A combination of a variety of focal length lenses (L2) were used with the collimation lens (L1) to modify the injected focal ratio into the sample entrance. A system of L3-L4 lenses were used to focus the output beam into the detector chip (D). This was used to calibrate the output of the chips with the injected beam. The detailed optical components that were used are listed in Table 5.2. The optical chips were mounted on a 5-axis stage and the lens system with the detector on a separate 3-axis stage. . . . . . . . . . . . . . . . . . . . . . 71

5.5 Throughput test apparatus in the laboratory for measuring the performance of the optical chip substrates. The SMF-28 (yellow) transfers the light from the light-emitting diode (LED) to the collimation optical element (L1) where it is focused into the chip with the optical lens (L2). Both chips are attached side by side on the 5-axis translation stage. A combination or re-imaging optics (L3, L4) are used to focus the output of the chips into the detector (D). The detailed optical components that were used are listed in Table 5.2. . . . . . . . . . . . . 72

5.6 Examples of input and output images produced by the photonic reformatters. Here the RF-4 reformatter in chip#1 is shown with the corresponding injected beam of f#9.3 @600 nm. **Left panel**: The injected beam with a red circle showing the collecting area of the RF-4 input and its cross section profile on the top sub-figure. **Right panel**: The resulted output slit intensity of RF-4 astrophotonic reformatter with its intensity profile along the slit plotted on the top sub-figure. . . . . . . . . . . . . . . . . . . . . . . . . . . . . . . . . . 73

5.7 Throughput laboratory measurements of the RF-4 astrophotonic reformatter in the optical chip#1 and chip#2 versus the injected beam's $f\#$. This is shown for the wavelengths of 600 and 800 nm. . . . . . . . . . . . . . . . . . . . . . . . 76

5.8 Throughput lab results of the output slit ends for the devices RF-1-4 from both of the optical chips versus the injected $f\#$. This is shown for the wavelengths of (a) 600 and (b) 800 nm. . . . . . . . . . . . . . . . . . . . . . . . . . . . . 77

5.9 Throughput lab results of the output slit ends for the devices RF-5-8 from both of the optical chips versus the injected $f\#$. This is shown for (a) 600 and (b) 800 nm. . . . . . . . . . . . . . . . . . . . . . . . . . . . . . . . . . . . . . . . 78

5.10 Throughput lab results of the output slit ends for the devices RF-9-11 from both of the optical chips versus the injected $f\#$. This is shown for the wavelength of 600 nm. . . . . . . . . . . . . . . . . . . . . . . . . . . . . . . . . . . . . . . . 79

5.11 The RF-4 device of the chip#1 3D design as appears in the `RSoft` CAD environment. The colours indicate the four different transition planes used. Red colour represents the entrance and blue the exit pseudo-slit. . . . . . . . . . . . . . . . 80

5.12 Throughput simulation results of the RF-4 astrophotonic reformatter. Top panel (a) shows the intensity of the propagated light through the device at a plane of the simulation domain where on the right the total throughput (black line) and the partial throughput of each of the individual waveguides are shown. Bottom panel (b) shows the output intensity of the slit end. This is shown for the wavelength of 600 nm. . . . . . . . . . . . . . . . . . . . . . . . . . . . . . 81

5.13 Near-field intensity distributions for the MM devices across both chips and wavelengths. (a)Chip#1 @600 nm, (b)Chip#1 @800 nm, (c)Chip#2 @600 nm, (d)Chip#2 @800 nm. All of the x-y axes of the images display the pixel numbers. 82

5.14 Illustration example of a pigtailed assembly composed of the SMF-28, the glass ferrule, the glass substrate and the supporting microscope slide underneath of them all. The device is illuminated using a HeNe laser coupled into the SMF-28 fiber entrance. Input and output planes of the chip are displayed in inset images. Image courtesy of Tobias Feger. . . . . . . . . . . . . . . . . . . . . . . . . . 83

6.1 Microscope image of the polished multi-core fiber in its ferrule. The cores are visible in a hexagonal formation with a pitch of 40 μm. The fiber has a 5.3 μm mode field diameter @980 nm ($1/e^2$) and a cladding diameter of $\sim$ 220 μm. Here, the cores are back-illuminated with a white light source. Numbers in red are used for core referencing below. . . . . . . . . . . . . . . . . . . . . . . . . 87

6.2 Schematic illustration of the NIR bench of the SCExAO facility. The 3D-printed fiber is shown at top left of the layout diagram. The beam's optical path from the AO188 to the integral field unit (IFU) is represented with purple and red colour. . . . . . . . . . . . . . . . . . . . . . . . . . . . . . . . . . . . . . . 88

6.3 scanning electron microscopy image of the 3D printed micro-lens array structure on top of the multi-core fiber ferrule. All 19 cores were 3D printed, though only the inner 7 were used for the on-sky run. . . . . . . . . . . . . . . . . . . . . . . 90

6.4 Illustration of the fibre-injection opto-mechanic setup on the SCExAO NIR bench. the 3D-printed multi-core fiber is using blue protection cable while the multi-mode fiber for calibration purposes, uses the orange one. . . . . . . . . . . 91

6.5 Throughput setup for measuring the efficiency of the 3D printed multi-core fiber. Calibration is achieved using a multi-mode fiber, lenses (L1-L2-L3) for collimation and focusing of the beam, beamsplitter (BS) and CMOS detector (D) for sampling the light output. . . . . . . . . . . . . . . . . . . . . . . . . . . . . 92

6.6 Spectroscopic setup of the 3D-printed Mono-Mode Multi-core fiber spectrograph using only off-the-shelf components. The footprint of the breadboard is 300 × 600 mm. The light injected from the 3D printed fiber (P1) was collimated by an optic (P2) before it was chromatically dispersed from an échelle grating (P3), cross-dispersed using a transmission grating (P4) and focused down using an optic (P5) on to the detector (P6). . . . . . . . . . . . . . . . . . . . . . . . . 94

6.7 Throughput efficiency for each of the 7 cores of the fiber (see Figure 6.1 for the correspondence of core# to position on the fiber). Injected $f\#$ was fixed to $f\#57.5$ by positioning the carriage and the fiber to the desired location. . . . . . 96

6.8 Throughput efficiency of the central core as a function of lateral displacement for SCExAO data compared to simulations from `Zemax`. Results are normalised to the maximum throughput and error-bars are smaller than the data points. . . 96

6.9 Illustration of time vs. airmass/altitude of the observation at 6:01 UTC -10 on the 17th of Oct. 2019 from Mauna Kea Observatory (green vertical region), for $\gamma$ Geminorum (solid blue line) and the moon (red dashed). Exposure started at the very end of observing time, close to sunrise. . . . . . . . . . . . . . . . . . . . 97

6.10 **Top panel:** Comparison spectra of $\gamma$ Geminorum from the 7 individual cores of the MCF at wavelength range of 925-935 nm where the many absorption features are visible. Each of the spectra is self-normalised and offset in respect to its intensity for clarity. **Bottom panel:** 2D detector image of a part of a spectral order from $\gamma$ Geminorum. Visible are all the 7 cores with sampled starlight. Notice the rotated pattern of the MCF formed by absorption features marked in red circles. On both axes numbers represent the detector pixels 4.8x4.8 µm. . . 99

6.11 Full frame spectrum of $\gamma$ Geminorum. . . . . . . . . . . . . . . . . . . . . . . . 101

6.12 Full spectrum derived from the sum of all of the fiber cores observing $\gamma$ Geminorum overplotted against a PHOENIX synthetic star spectrum akin to the target (Husser et al. 2013). The observed spectrum is influenced by the numerous telluric lines of the earth while the synthetic spectrum has no influence of the them. . . . . . . . . . . . . . . . . . . . . . . . . . . . . . . . . . . . . . . . . 102

6.13 Flux performance of the 3D printed MCF as observed on-sky compared to the expected performance. . . . . . . . . . . . . . . . . . . . . . . . . . . . . . . . 102

6.14 **Top panel:** Intensity line profile of the apodized injected point spread function normalised to its peak using the Phase-Induced Amplitude Apodization optics, for the on-sky and laboratory data. A Gaussian fit was performed on the on-sky data. **Bottom panel:** 2D image of the point spread function (PSF) in linear (left) and logarithmic (right) colour scale for better clarity. The exposure time was ∼0.83 sec. . . . . . . . . . . . . . . . . . . . . . . . . . . . . . . . . . . . . 104

6.15 **Top sub-figure:** Centre of mass shift of the on-sky beam during the observation. Over-plotted with two circles are the full width half maximum (FWHM) of the on-sky beam and the laboratory, over time right after the time of observation. The average is represented with the black dashed line. **Bottom sub-figure:** The ratio of on-sky to the laboratory FWHM on both detector axes over time. . 105

# Chapter 1

# Prolegomenon

## 1.1 Outline

The main purpose of this thesis is to explore areas of photonics that have high potential for more efficient astronomical observations and its applications to future astronomical observations.

In more detail, the focus is on the applications of astrophotonic technology in high resolution spectroscopy, and how it compares to current instrumentation. I begin by simulating the performance of an astrophotonic component called the photonic dicer (PD), tested previously on-sky. I use my model to optimise its simulated performance and test its stability and noise contribution to astronomical observations. I test the developed technique on a previously optimised version of the PD the hybrid reformatter (HR), also characterised on-sky, exploring areas of improvement and further optimisations. In the optimisation I look at various parameters of these astrophotonic devices for making them more efficient by 6-10% for conventional high resolution spectrographs to suit astronomical observations. I characterise two inscribed optical chips with various reformatter devices, on-sky and in a lab environment. Lastly I model, manufacture and test on-sky the 3D printed micro-lenses on top of a custom-made optical fiber, aiming to optimise the throughput and coupling to a diffraction limited spectrograph in the near infrared wavelength regime, coupled in Subaru Coronagraphic Extreme Adaptive

Optics (SCExAO). I conclude that the optimal astrophotonic component for high resolution spectroscopy is dependent on the science case.

Chapter 2 provides the necessary theory of spectroscopy from the perspective of astrophotonics. It begins with the description of the most common astronomical instrumentation techniques used to date, and continues with an introduction to the field of astrophotonics and its most commonly-used component, the fiber-waveguide. This chapter is based on the existing literature.

Chapter 3 presents the simulations performed on the PD. Through geometrical re-designing of the reformatter, the throughput and noise properties of the component are explored and optimised using two sophisticated simulation tools in conjunction. This chapter is largely drawn from Anagnos et al. (2018a).

Following that, in Chapter 4 a similar procedure from the previous chapter is been used to simulate a HR. This astrophotonic component is also tested on-sky, and is more highly-optimised than the standard reformatter. Results are in agreement with literature while an optimisation of its performance is also achieved. It is largely drawn from Anagnos et al. (2018b).

In Chapter 5 the lab characterisation of various astrophotonic reformatters in the visible wavelengths is presented. These were manufactured by the Optofab facility at Macquarie University in Sydney Australia, including 22 different waveguide geometries at the input and the output and with different manufacturing parameters. It is primarily based on Anagnos et al. (2020b, in prep.).

Chapter 6 synthesises the insights gathered in the previous chapters to present the design and manufacture of a custom astrophotonic component. This is a combination of 3D printed microlenses on top of a custom multi-core fiber (MCF) feeding a diffraction limited spectrograph. It is based on Anagnos et al. (2020a, MNRAS, in prep.).

Finally, chapter 7 summarises the results of all previous chapters and highlights further work on the route powerful astrophotonic-enabled spectroscopy at major astronomical observatories.

# Chapter 2

# Background Theory

## 2.1 Introduction

In this chapter, I develop the necessary theory of spectroscopy and astrophotonics, focusing on astronomical spectroscopy and its current applications. Furthermore, I will concentrate on astronomical spectrographs that make use of dispersive optics (e.g. prism, diffraction grating) to chromatically disperse the incoming light. More attention will be given to the spectrographs used in high-resolution spectroscopy. There are various other spectrograph architectures (e.g., Allington-Smith 2007), though they are beyond the scope of this thesis and won't be covered here. Emphasis, as well, will be given to the potential of current astrophotonic devices that have been developed as test-devices, and their potential application to the next generation of ELTs. The chapter has parts drawn from Anagnos et al. (2018a) & Anagnos et al. (2020a, MNRAS, in prep.).

## 2.2 Motivation

A plethora of intrinsic and extrinsic information can be collected through astronomical spectroscopy, such as distance, motion properties, chemical characteristics as well as the existence of nearby companions (Massey & Hanson 2013).

Almost half a century ago, the first fiber fed instruments began supplementing existing astronomical spectrographs. Instead of being directly attached to the primary focus of the telescope, the optical fibers took the light from the primary focus to a remotely located instrument. This relaxes the mechanical constraints due to varying gravity vectors and the measurement precision can be increased as the instrument can be stabilised and controlled far better in the controlled laboratory environment as opposed to in the telescope dome. The fibers in these instrument were typically large diameter multi-mode fibers (MMFs), in order to couple all the light from a seeing-limited image (Hill et al. 1980; Hill 1988).

A contemporary development of these fiber spectrographs was integral field spectroscopy (IFS). IFS makes use of at least two spatial samples to investigate small regions of the telescope's image plane (e.g. adjacent or extended objects) (Allington-Smith 2006). The spectra from different locations of the telescope's image plane are positioned on the same detector, but physically displaced to avoid cross contamination. The advantages of using fibers for IFS were soon realised, allowing spatial information of the target object to be recorded in a simple way, as well as greater flexibility to reformat the obtained spectra to fit the limited detector space than other existing methods.

Nowadays, using multiple MMFs with a relative large core diameter above 50 µm to form an integral field unit (IFU) that couples seeing-limited starlight is a relatively standard practice (e.g. Ge et al. 1998; Croom et al. 2012; Bryant et al. 2016; Tozzi et al. 2018).

These versatile workhorses have enabled many discoveries, however, these instruments are large, due to conservation of étendue, which means they are costly and difficult to stabilise. The ability to reduce the size would open up new avenues and reduce costs. Another important factor is that these instruments do not realise the full spatial resolution the telescope optics can provide as they work at the seeing limit, which limits the angular resolution to values of approximately one arcsecond, while a 4 m telescope, for example, has a diffraction limit resolution of 51 milli-arcseconds (mas) at 1 micron wavelength. One solution is to use smaller core diameter fibers, or single-mode fibers (SMFs) and has been proposed for several types of instruments (e.g. Leon-Saval et al. 2012; Tamura et al. 2012; Crepp et al. 2016; Rains et al. 2016). The main roadblock is that coupling starlight into SMFs from large telescopes with a primary diameter over 4 m with a seeing-limited output is extremely inefficient.

Various efforts have been attempted to increase the coupling into SMFs, with great success in recent years (e.g., Coudé du Foresto & Ridgway 1992; Coudé du Foresto et al. 2000; Ghasempour et al. 2012; Harris et al. 2015; Bechter et al. 2016; Crepp et al. 2016; Cvetojevic et al. 2017; Jovanovic et al. 2017; Anagnos et al. 2018a; Bechter et al. 2020). This is in a large part due to the adaptive optics (AO) systems, which reduce the PSF size and wavefront deformation to acceptable levels. In particular, extreme adaptive optics (ExAO) systems have demonstrated Strehl ratios [1] in excess of 90% (close to diffraction-limit) in the H-band and for a small angular separation (e.g., Dekany et al. 2013; Agapito et al. 2014; Macintosh et al. 2014; Jovanovic et al. 2015; Vigan et al. 2016; Guyon et al. 2020), allowing close to optimum coupling. ExAO systems are also able to maintain a constant PSF position, in better than median seeing on-sky conditions, essential for efficient coupling.

Using SMFs also enables astronomers to take advantage of the diffraction-limited imaging provided by AO. Together these can open up science cases not available to conventional instruments. Examples include spatially resolving the surface of barely resolved stellar photospheres and molspheres using the Subaru telescope and SCExAO. The target list for a 8 m class telescope in the northern hemisphere (i.e. Subaru telescope) of such stars, include in alphabetical order, Aldebaran (Alpha Tauri) with an angular size of ∼19 mas, Antares (Alpha Scorpii) ∼40 mas, Arcturus (Alpha Bootis) ∼21 milli-arcseconds (mas), Betelgeuse (Alpha Orionis) ∼50 mas and Mira (Omicron Ceti) ∼50 mas. This population are all giants whose their mass loss mechanism is considered complex through their cool (∼2000 K) molecular wind (∼10 km $s^{-1}$) and their hot corona (∼10,000 K) (Tsuji 2008). A spectrograph with a resolving power of several tens of thousand is enough to distinguish the differential spectral velocities of the surface that are of the order of a few km $s^{-1}$ order. For the case of a single observation such a spectrograph will provide useful information regarding the photosphere of the star in high resolution, while with sequential observation data it can provide information on the differential rotation of the surface probing the magnetic field properties and the mass loss of the target (e.g., Lobel et al. 1999, 2004; Ohnaka 2009; Khouri 2018; Ohnaka & Morales Marín 2018; Wood et al. 2019).

---

[1] https://www.telescope-optics.net/Strehl.htm

Further science applications involve the study of Mira variables that belong in the red giant category where the mass loss kinematics are of special importance as well as their dust and wind properties (e.g. Norris et al. 2012). Moreover, such observations can unveil the orbital parameters from sub-arcsecond companions such as the unevenly bright yet well resolved Mira AB system which is the closest wind accretion binary (e.g. Karovska et al. 2011; Ramstedt et al. 2014; Vlemmings et al. 2015). Additionally, such observations can contribute on studying the stellar chromospheres by observing of chromospherically sensitive lines, such as the Ca II H & K lines, the hydrogen lines in the infrared (IR) regime and the He I IR triplet lines at 1083 nm, that present a useful indicator of chromospheric activity (Fuhrmeister, B. et al. 2019). Lastly, if the spectrograph is highly stabilised, it will enable precise radial velocity (RV) spectroscopic measurements which are a key tool in the search for extrasolar planets in our cosmic neighbourhood. This is of particular importance in the NIR regime, where the achievable precision lags behind the one of visible range spectrographs, yet, most stars in our neighbourhood are so-called M dwarfs which emit most of their light in the near NIR.

Whilst SM IFUs open these new science cases, as with regular fiber IFUs, they suffer from an issue with fill fraction. Due to the need for a cladding region around the central core, fiber IFUs can only sample a certain percentage of the light at the focal plane. Originally, this was on the order of 60-65%, though recent developments have increased this to 73% (Croom et al. 2012). To solve this, microlenses can be attached to the IFU, increasing the fill fraction (e.g., Courtes 1982; Bacon et al. 1995). However, aligning these arrays and fiber bundles is difficult as the alignment tolerances are or the order of micrometers.

## 2.3 Principles of spectroscopy

Over the last decades, spectroscopy has demonstrated its value in the field of astronomy by facilitating a large number of discoveries. Spectroscopic measurements have applications to an enormous range of sky-targets, from dust on scales of µm up to the scales of whole exoplanets, and galaxies, spanning thousands of parsecs. Spectroscopy allows for the analysis of the collected light by decomposing it into its component wavelengths, by comparison to known spectral lines (emission or absorption). With the spectral information, a wealth of other parameters such as the target's chemical composition,

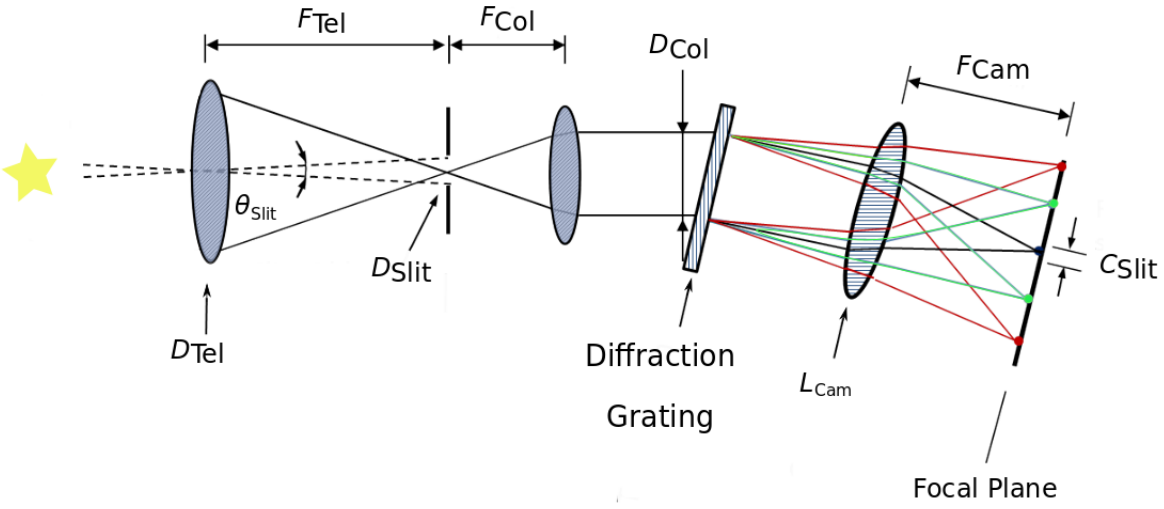

Figure 2.1: Illustration of a conventional astronomical spectrograph design. The starlight is focused by the telescope ($D_{\mathrm{Tel}}$) onto the entrance slit ($D_{\mathrm{Slit}}$) of the spectrograph, where it is collimated by an optic and chromatically dispersed by the diffraction grating. After that, the starlight is focused down to the detector by another optic ($L_{\mathrm{Cam}}$).

temperature, relative motion to another object, distance and many other inherent parameters can be derived.

The simple basic architecture of a dispersive spectrograph consists of a slit through which a certain sky angular region (starlight) enters the instrument. After its collimation by an optic (e.g. lens, parabolic mirror) it gets chromatically separated using a dispersive element such as a grating or prism. Usually, in order to achieve the minimum instrument size, the dispersive element is positioned in the pupil plane of the instrument, collecting all the on- and off-axis beams. Finally, the starlight is focused onto to the detector using another optical element. In order to measure the relative intensity of the light and correlate its position to a wavelength, a mapping of position is generated using a source of known wavelength or spectral pattern, such as Thorium-Argon, Mercury, Argon, Krypton or Neon lamps (Zuiderwijk & Knapen 1989), frequency combs (Picqu & Hnsch 2019), or a Fabry - Pérot Etalon (Gurevich et al. 2014). In addition to that, observation of stars with a known spectrum (Moehler, S. et al. 2014) or iodine cells (Marcy & Butler 1992) can be used for the wavelength calibration of the spectrum. Figure 2.1 presents a graphical representation of such a spectrograph using a transmission grating to chromatically disperse the light.

To begin with, the fundamental grating equation (Hecht 2002) that represents the behaviour of the collimated beam after the grating influence is given by

$$d(\sin\alpha + \sin\beta) = m\lambda_{\mathrm{c}}, \tag{2.1}$$

where $d$ is the grating ruling density given in lines/mm, $\alpha$ and $\beta$ are the incident and the diffracted angle from the grating, respectively, $m$ is the diffraction order and $\lambda_{\mathrm{c}}$ is the central wavelength of observation. If a reflective grating is used instead, the positive sign changes to negative. Figure 2.2 presents the cross section of two example types of diffraction gratings; on the left part of the figure a standard non-blazed grating is illustrated where the grooves are placed perpendicular to the grating facet. The majority of the diffracted beam's energy is contained in the $0^{\mathrm{th}}$ order in this configuration, while for the case of a blazed reflective diffraction grating (see right panel of Figure 2.2), the majority of the energy is concentrated towards the higher orders, due to the inclined grooves of the grating angled by $\theta_{\mathrm{B}}$. In the case where the blaze angle is optimal for a certain wavelength of interest, the grating is mostly placed to operate in quasi-Littrow mode ($\alpha \approx \beta \approx \theta_{\mathrm{B}}$) where it is more efficient.

The grating introduces an angular dispersion to the incoming light that is given by differentiating the equation 2.1 with respect to the wavelength and is independent of the optical parameters of the camera optics. The angular dispersion is given by

$$\frac{d\beta}{d\lambda} = \frac{m}{d\cos\beta} = \frac{\sin\alpha + \sin\beta}{\lambda\cos\beta}. \tag{2.2}$$

In order to achieve a higher angular dispersion, either the diffraction angle ($\beta$) should be decreased or another grating with higher ruling density should be selected. Operating the instrument at the well-known quasi-Littrow configuration, where $\alpha \approx \beta \approx \theta_{\mathrm{B}}$, modifies the equation 2.2 into

$$\frac{d\beta}{d\lambda} = \frac{2\tan\theta_{\mathrm{B}}}{\lambda}. \tag{2.3}$$

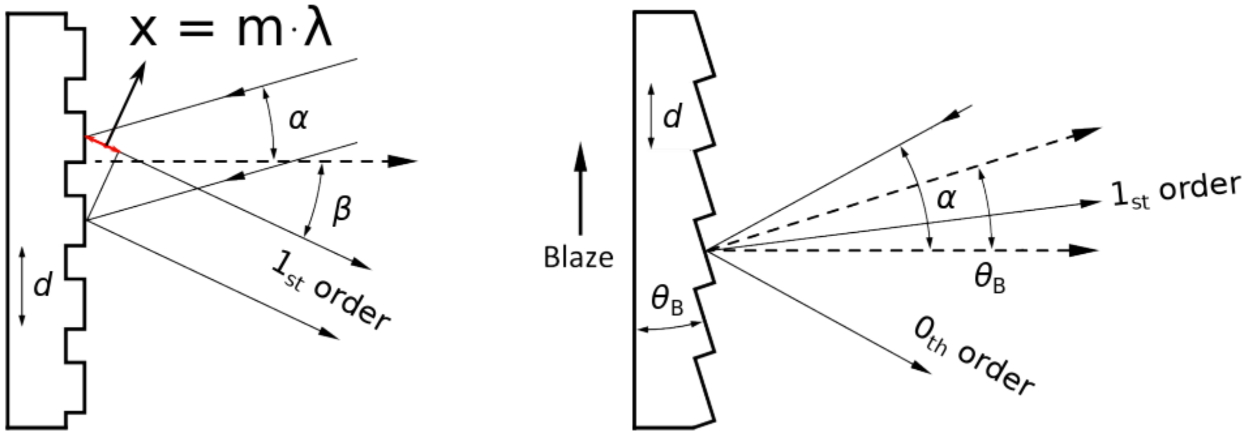

Figure 2.2: Example of **(left)** a non-blazed diffraction grating where the grooves are placed in parallel with the phase of the grating where the most of the energy is concentrated at the zeroth order. **(right)** A blazed reflective diffraction grating where the grooves are inclined by the blaze angle $\theta_{\mathrm{B}}$ with respect to the grating face where the majority of the energy is concentrated towards higher orders. Figures include the light rays path before and after the grating.

Including the effect of the camera optic system ($L_{\mathrm{Cam}}$) parameters into the dispersion formula, one can derive the linear dispersion of the spectrum in the focal plane as illustrated in Figure 2.3. Given that $d\beta \cdot F_{\mathrm{Cam}} = dx$, where $F_{\mathrm{Cam}}$ is the focal length of the camera lens, the relationship of the physical separation of different wavelengths at the detector/focal plane is given by

$$\frac{dx}{d\lambda} = F_{\mathrm{Cam}} \frac{d\beta}{d\lambda} = F_{\mathrm{Cam}} \frac{\sin\alpha + \sin\beta}{\lambda \cos\beta}. \tag{2.4}$$

Another important parameter of a slit input spectrograph under the atmospheric perturbations of the night sky, is the spectral resolving power (Raskin, G. et al. 2011). This is the parameter used to describe the smallest wavelength increment that can be distinguished by the instrument and is given by

$$R = \frac{\lambda}{\Delta\lambda}, \tag{2.5}$$

where $\lambda$ is the central wavelength of the observation and $\Delta\lambda$ is the smallest resolvable difference between wavelengths.

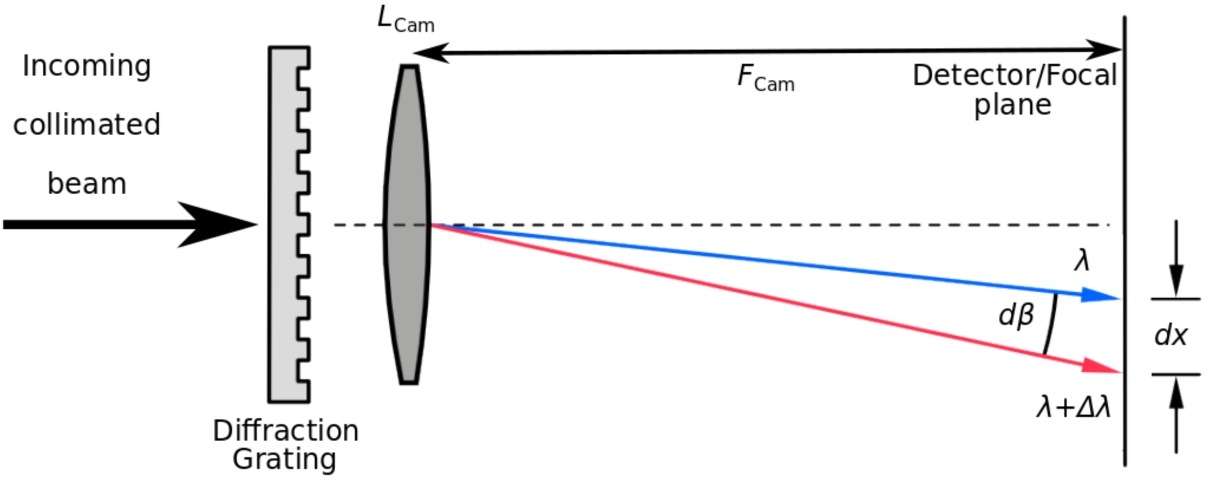
Incoming
collimated
beam
Diffraction
Grating
$L_{\mathrm{Cam}}$
$F_{\mathrm{Cam}}$
Detector/Focal plane
$\lambda$
$d\beta$
$\lambda+\Delta\lambda$
$dx$

Figure 2.3: Illustration example of the angular ($d\beta/d\lambda$) and linear ($dx/d\lambda$) dispersion of a transmission grating.

Taking into account the effect of the instrumental broadening of a spectral line for the case of an ideally small slit width, the angular half-width of the profile (between the central maximum and the first minimum) is given by (Hecht 2002)

$$\Delta\beta = \frac{\lambda}{S\cos\beta}, \tag{2.6}$$

where $S = D_{\mathrm{Col}}/\cos\beta$ is the length of the projected collimated beam ($D_{\mathrm{Col}}$) onto the grating surface.

Combining equations 2.3 and 2.5 according to the Rayleigh criterion, the maximum ideal resolving power for the Littrow configuration is

$$\begin{aligned} R_{\max} &= \frac{\lambda}{\Delta\lambda} = \frac{2S\sin\theta_{\mathrm{B}}}{\lambda}, \\ R_{\max} &= \frac{2D_{\mathrm{Col}}\tan\theta_{\mathrm{B}}}{\lambda}. \end{aligned} \tag{2.7}$$

The derived equation 2.7 is valid for the case of a point source diffraction-limited instrument under no atmospheric perturbations. However, in reality this equation changes to meet the perturbations of the Earth's atmosphere in the incoming wavefront.

The projected into detector slit width ($C_{\text{Slit}}$) is given by

$$\begin{aligned} C_{\text{Slit}} &= AD_{\text{Slit}}\frac{F_{\text{Cam}}}{F_{\text{Col}}} = A\frac{\theta_{\text{Slit}}D_{\text{Tel}}F_{\text{Cam}}}{D_{\text{Col}}}, \\ A &= \frac{\cos\alpha}{\cos\beta} \end{aligned} \tag{2.8}$$

where $A$ is the anamorphic magnification of the collimated beam before and after the grating influence, $D_{\text{Slit}}$ is the width of the slit entrance, $F_{\text{Col}}$ is the focal length of the collimating front lens, $D_{\text{Tel}}$ is the diameter of the telescope's primary mirror and $\theta_{\text{Slit}}$ is the corresponding sky angular dimension of the slit width.

The resolving power under by the combination of equation 2.4, 2.6 and 2.8, is given by

$$R = \frac{\lambda}{\Delta\lambda} = \frac{\lambda D_{\text{Col}}}{\theta_{\text{Slit}}D_{\text{Tel}}}, \tag{2.9}$$

which changes for the case of a grating spectrograph as

$$R = \frac{S(\sin\alpha + \sin\beta)}{\theta_{\text{Slit}}D_{\text{Tel}}}, \tag{2.10}$$

and for the Littrow configuration is given by

$$R = \frac{2D_{\text{Col}}\tan\theta_{\text{B}}}{\theta_{\text{Slit}}D_{\text{Tel}}}. \tag{2.11}$$

### Free Spectral Range

In order to reach high resolving power for a spectrograph that uses a diffraction grating as a dispersive element, another crucial factor is the free spectral range (FSR). This parameter estimates the location at which two neighbouring spectral orders overlap in the focal plane, as seen in Figure 2.4. The greater the FSR, the more the physical and wavelength spacing between adjacent spectral orders.

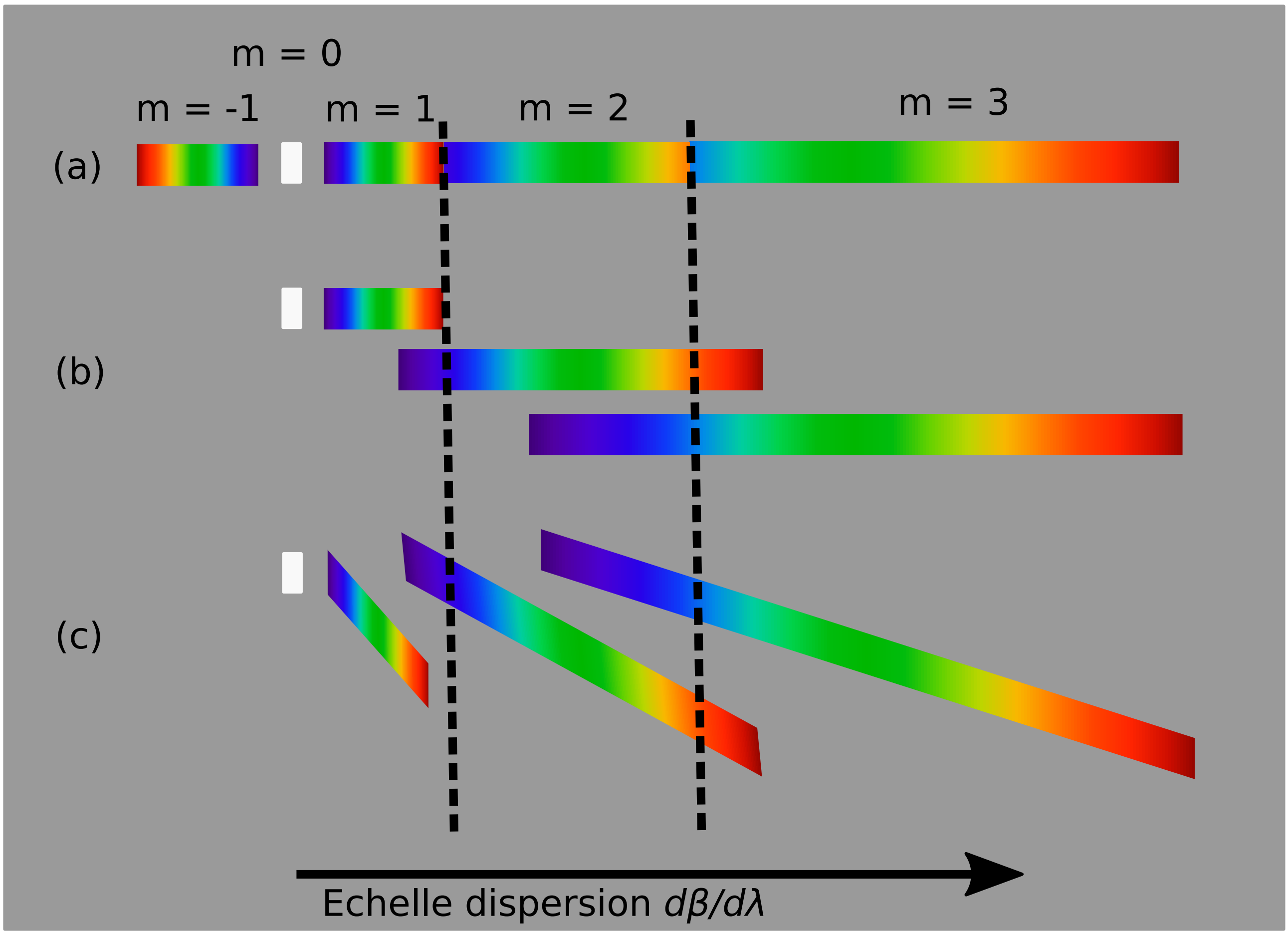

Figure 2.4: Schematic presentation of the FSR concept. The top panel (a) shows the spectrum of a conventional spectrograph as in Figure 2.1, where the orders overlap near their edges. The middle panel (b) shows the same spectrum as before but separates each order to highlight the overlapped regions of the spectrum. The bottom panel (c) illustrates the output spectrum of an échelle spectrograph using another dispersing element (grating, prism) used for cross-dispersion of the orders, such that no overlap is happening.

In order to derive the formula for the FSR, starting from equation 2.1 and addressing the case where two different wavelengths ($\lambda$ and $\lambda + \Delta\lambda_{\mathrm{FSR}}$) from neighbour orders ($m+1$ and $m$, correspondingly) overlap, the formula rearranges to

$$\begin{aligned} d(\sin\alpha + \sin\beta) &= (m+1)\lambda = m(\lambda + \Delta\lambda_{\mathrm{FSR}}), \\ \Delta\lambda_{\mathrm{FSR}} &= \frac{\lambda}{m}. \end{aligned} \tag{2.12}$$

According to the equation 2.12, there is an inverse relation of FSR with the spectral order. Hence, FSR and spectral order are inversely proportional quantities.

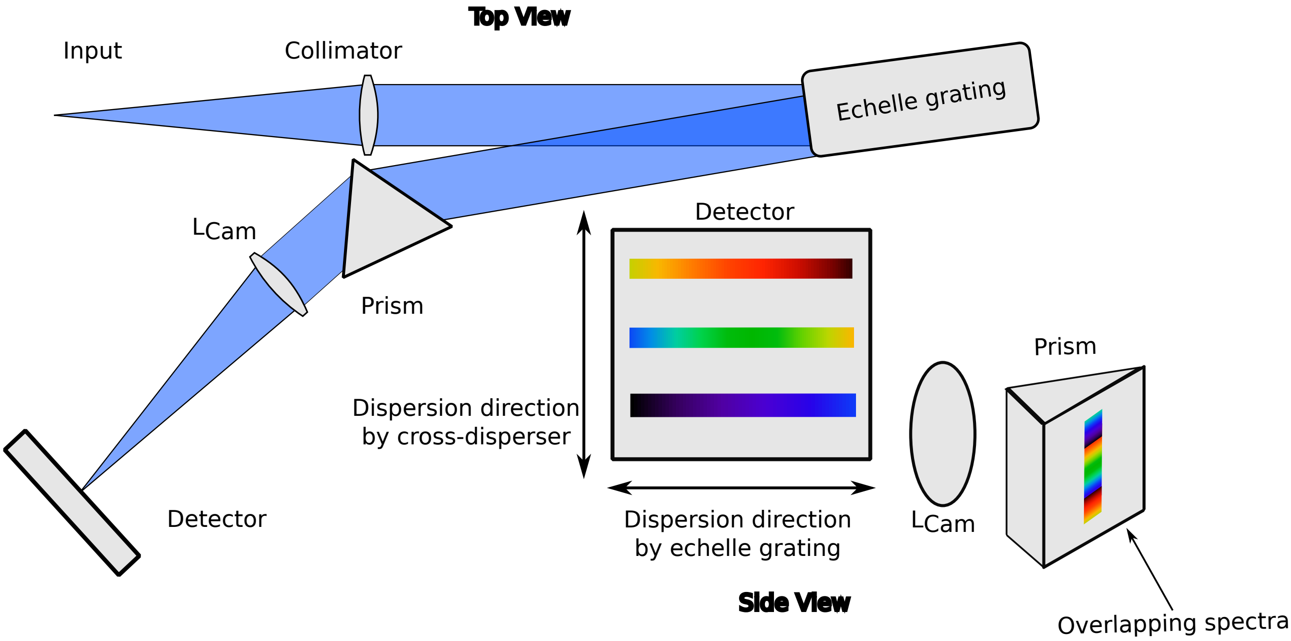
Top View
Input
Collimator
Echelle grating
LCam
Prism
Detector
Detector
Dispersion direction
by cross-disperser
Dispersion direction
by echelle grating
Prism
LCam
Overlapping spectra
Side View

Figure 2.5: Example architecture of an échelle spectrograph using a prism as cross-disperser.

### Cross-dispersion of the spectrum

Over the past decades, many suggestions have been proposed for mediating the FSR issue; for instance by using detectors that can resolve the sampled energy/wavelength (e.g., Szypryt 2017; Peacock et al. 1996; Romani et al. 1999) or using filters for windowing the transmitted wavelengths. However, the above-mentioned suggestions are either in a state of development, or majorly limit the throughput and bandwidth of the instrument where even the slightest fraction is quite important.

Due to the above limitations, the common solution to the FSR problem is to add another dispersive optical element before or after the main dispersive optical element and perpendicular to the dispersion direction of the collimated beam, in order to separate the orders efficiently. This technique is known as cross-dispersion. Depending on the purpose of the instrument, available funds, detector size, order separation, bandwidth and throughput of the instrument, different optical elements can be used to cross-disperse the spectrum, such as a prism, a low dispersive grating, a combination of them both which is called a grism, or a volume phase holographic (VPH) grating.

### Fiber-fed spectroscopy

Conventionally, spectrographs have been attached directly to the telescope, such that the slit of the instrument samples the starlight into the focus of the telescope. Alternatively, the possibility of using

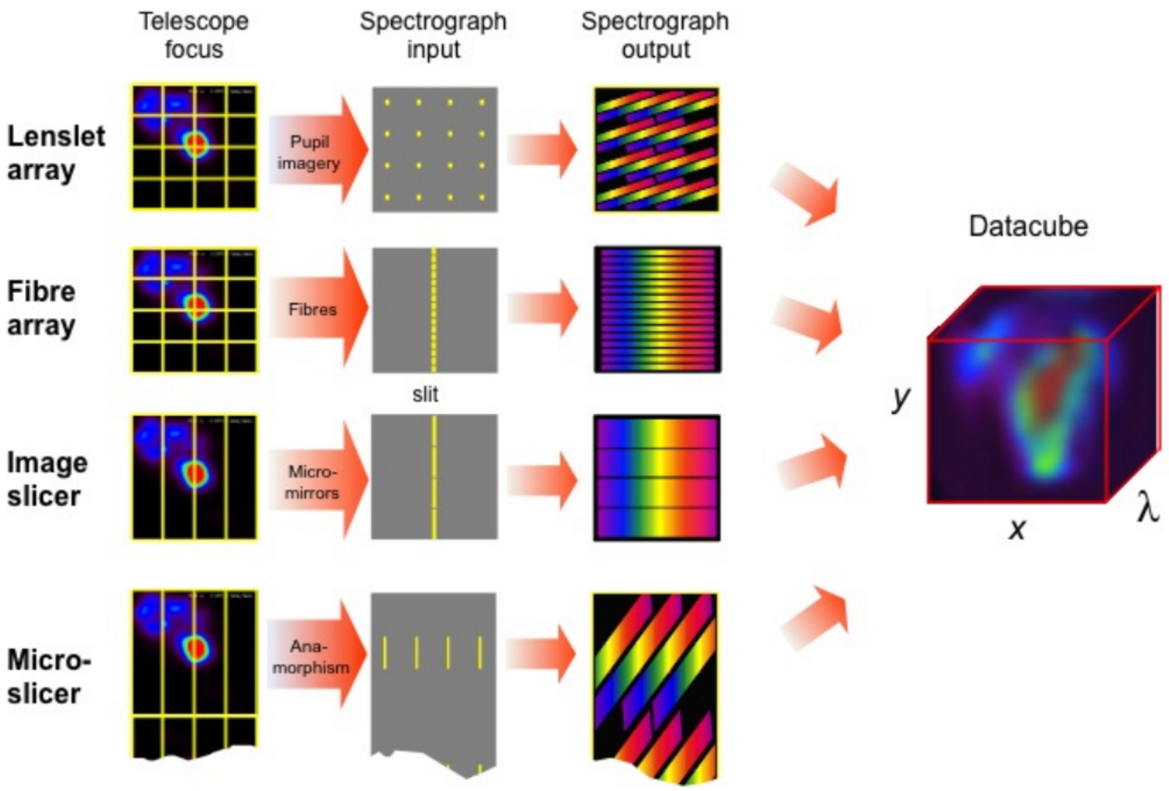
Telescope focus
Spectrograph input
Spectrograph output
Lenslet array
Pupil imagery
Fibre array
Fibres
slit
Image slicer
Micro-mirrors
Micro-slicer
Ana-morphism
Datacube
y
x
λ

Figure 2.6: Illustration of various types of IFS systems with their corresponding output spectra. All 4 methods produce a datacube with position and spectrum information. Image courtesy Allington-Smith & Content.

optical fibers to link the telescope with the spectrograph allows the instrument itself to be detached and therefore located remotely in a well-controlled and calibrated environment. This method increases the stability, precision and accuracy of the measurements by placing the spectrograph in a more stable environment than the dome of the telescope.

Furthermore, if many fibers are installed, the spatial information of the image in the focal plane can be retained as is illustrated in Figure 2.6. This figure illustrates the possible configuration of fibers used for IFS, where the spatial information of the input is retained, similarly to other methods that do not use fibres (e.g., Parry 1998; Parry 2006; Brown et al. 2014). In more detail, in the top system of Figure 2.6, lenslet arrays slice the focal plane field of the telescope to produce a number of spectra equal the number of lenslets in the array. Immediately below, fibers replace the lenslets and reformat the input to a linear array at the spectrograph's entrance. The final two images show two other conventional ways using image slicers and micro-slicers to reformat the focal plane in different geometrical arrangements for feeding the instrument. This way, multiple inputs of the sky can be spectrally analysed at the same time on the same detector.

## 2.4 Astrophotonics

Over the last decade, interest has been growing towards the exploitation of small compact optical components of photonic technology to be used in astronomical instrumentation (Bland-Hawthorn & Kern 2009). These components show potential over a broad area of applications, targeting the reduction of overall cost and size. Some examples are: optical fibers with relatively large cores known as multi-mode fibers (MMFs) that are being used to transport the light from the telescope to the instrumentation for measurements in a remote controlled environment (Barden et al. 1981), inscription of precise wavelength filters for OH suppression of sky emission lines (Bland-Hawthorn et al. 2011; Trinh et al. 2013), components for spectroscopy (e.g., Cvetojevic et al. 2009, 2012), for interferometry (Le Coarer et al. 2007; Le Bouquin, J.-B. et al. 2011), spatial reformatters (Thomson et al. 2010; Jovanovic et al. 2012; Spaleniak et al. 2013; Harris et al. 2015), and integrated dispersive spectrophotometers (Watson 1995). In the following sections, an introduction of astrophotonic devices such as fibers and spatial reformatters as well as their parameters and capabilities will be presented.

### 2.4.1 Optical fibers: Basic properties

Optical fibers and waveguides in general, propagate light through them according to their specific geometric parameters and materials optimised for the wavelength of the light to be propagated. To calculate and simulate the properties of this propagation for further improvement or study, there are 2 models used: the geometrical-ray and the wave model.

#### Geometrical propagation model

Light of certain wavelength is confined and guided through an optical fiber according to Snell's law. This law of physics known as Snell-Descartes law or law of total internal reflection, is a mathematical expression that describes the correlation of incident and refraction light-wave angle during its propagation through isotropic media of varying refractive indices.

In general, optical fibers consist of a cylindrical in cross section, higher refractive index core $n_{\text{core}}$ surrounded by a lower refractive index cladding $n_{\text{cladding}}$ as shown in Figure 2.7.

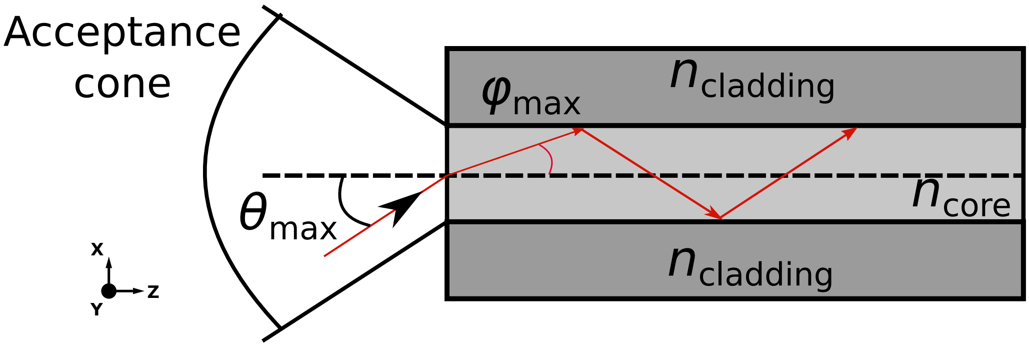

Figure 2.7: Illustration of a typical MMF cross section, with a top-hat refractive index profile. NA is also manifested in the figure.

According to the geometrical-ray model of light-propagation through the waveguide, total internal reflection is taking place at the core-cladding boundary when: $n_{\text{core}} \sin \pi/2 - \phi \geq n_{\text{cladding}}$. As the incident angle $\theta$ of the ray is a function of the angle $\phi$ by $\sin\theta = n_{\text{core}} \sin\phi \leq \sqrt{n_{\text{core}}^2 - n_{\text{cladding}}^2}$, the criterion for total internal reflection is given by

$$\theta \leq \sin^{-1}\sqrt{n_{\text{core}}^2 - n_{\text{cladding}}^2} \equiv \theta_{\text{max}}, \tag{2.13}$$

where $\theta_{\text{max}}$ represents the maximum angle - cone that a ray can be coupled into the fiber and is known as the numerical aperture (NA). Typically, NA varies between ∼0.1-0.25 for a multi-mode fiber (MMF) and is ≤0.2 for a SMF and a few-mode fiber (further explanation below).

### Wave propagation model

When exploring the wave-nature of light and how it propagates through a medium, not only does the geometrical propagation model have to be considered, but also the wave propagation model. Even in cases where the incident angle of the light into the fiber is less than the $\theta_{\text{max}}$, there is no propagation of the light through it. That's due to light beam's correlation of the incident angle of propagation with constructive/destructive interference according to the Maxwell's equations of electromagnetic wave analysis field.

Any light-ray that undergoes total internal reflection inside the fiber's core suffers phase shifts ($\Phi$), also known as Goos-Hänchen shifts (Marcuse 1974; Tamir et al. 2013), given by (Okamoto 2010, p. 3)

$$\Phi = -2\tan^{-1}\sqrt{\frac{2\Delta}{\sin^2\phi} - 1}, \tag{2.14}$$

where the relative refractive-index difference $\Delta \cong (n_{\text{core}} - n_{\text{cladding}})/n_{\text{core}}$.

Accounting for the phase matching conditions of the propagated wavefronts, we can derive that (Okamoto 2010, p. 4)

$$\tan(kn_{\text{core}}\alpha\sin\phi - \frac{m\pi}{2}) = \sqrt{\frac{2\Delta}{\sin^2\phi} - 1}, \tag{2.15}$$

where $k = 2\pi/\lambda$ is the wavenumber of the propagated beam. According to equation 2.15, only certain propagation angles are affected by the fiber's core radius $\alpha$, refractive indices of the core and the cladding as well as the wavelength of the propagated light (Marcuse 1989). The solutions of equation 2.15 describe the field distribution of the propagating beam commonly known as the mode. The accepted propagation constant values $\beta = kn_{\text{core}}\cos\phi$ are the eigenvalues.

The fundamental mode is the field distribution that is derived from the equation 2.15 given $m = 0$ and with the minimum propagation angle $\phi$, whereas the modes with higher angles and $m \geq 1$ are called higher order modes.

### $V$-number of a fiber

A crucial parameter concerning fiber is the normalised frequency, known also as the waveguide frequency, waveguide parameter or $V$ number. For the case of MMF with a top-hat refractive index profile, a cylindrical core cross section and a limited refractive index difference ($\Delta n$), the $V$ is given by

$$V = \frac{2\pi\alpha}{\lambda}NA = \frac{2\pi\alpha}{\lambda}\sqrt{n^2_{\text{core}} - n^2_{\text{cladding}}}, \tag{2.16}$$

where $\alpha$ is the radius of the fiber's core. Using this formula, an estimate of the number of spatial modes an MMF can be calculated as well as a rough criterion for whether an waveguide is single-moded ($V \leq 2.4$ for a circular cross-section fiber) or not.

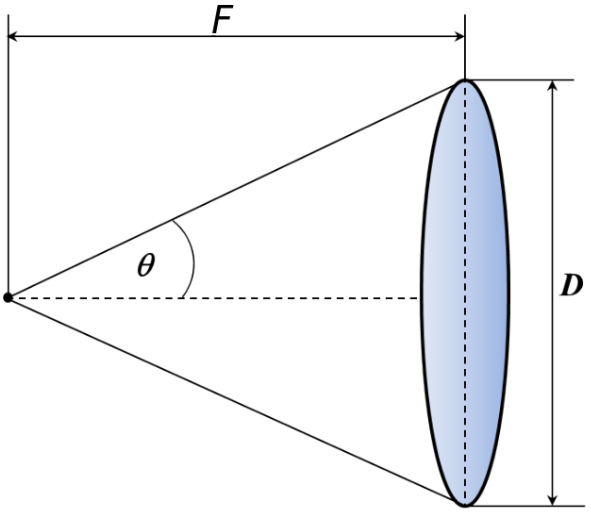

Figure 2.8: Illustration of focal ratio ($f/\#$) of a lens.

### Numerical Aperture in optics

In the context of optics, the NA is the cone angle of the light coupled into the fiber illustrated graphically in Figure 2.8 and is expressed as

$$NA = \sin\theta \sim \frac{1}{F}\frac{D}{2}, \tag{2.17}$$

where $D$ is the diameter of the lens, $F$ the focal length of it, and $\theta$ the half-angle of the cone of light that enters/exits the lens.

A useful parameter of optics is the focal ratio f/# that's inversely related to NA by

$$f/\# = \frac{F}{D} \sim \frac{1}{2 \cdot \mathrm{NA}}. \tag{2.18}$$

## 2.4.2 Fibers in instrumentation

Optical fibers have been used in astronomy since the 1970s and ever since they have shown their potential in the field with many applications such as IFS, spectroscopy, photometry, multi-object spectroscopy, interferometry, and high-precision radial velocity spectroscopy (Parry 1998).

One of their initial major contributions was the decoupling of the instrument from the telescope into a remote environment controlled room for more stability in measurements.

### Single-mode fibers

Fibers that permit only the propagation of the fundamental spatial mode (neglecting the polarisation direction) on a certain wavelength, thus fulfilling the condition derived from equation 2.15 for $m = 0$ are called single-mode fibers (SMFs).

Their core diameter is on the order of few microns ($\sim 3 - 10$ μm) depending on the wavelength that is designed to be single-mode (SM), and their refractive index difference ($\Delta n$) between core and cladding is on the order of $\sim 10^{-3}$.

They have inherent spatial stability of their fundamental mode while the only variable is the intensity profile at the output. Thus, they have neither modal noise (explained in Section 2.4.2) nor focal ratio degradation (FRD). Their output beam distribution is a cosine with an exponential drop off, but can be approximated as a Gaussian.

However, it's quite hard to optimise the coupling of light into them due to the minimal size of their core, and a non-optimal and unstable injection system leads to major losses.

An estimate of an SMF mode field diameter (MFD) size can be can be derived from Marcuse's formula (Marcuse 1977), provided that $V$ is on the region between $V \sim 0.8 - 2.5$ and a top-hat refractive index profile

$$\frac{w}{a} \sim 0.65 + \frac{1.6191}{V^{3/2}} + \frac{2.879}{V^6}, \tag{2.19}$$

where $w$ is the MFD, and $\alpha$ is fiber's core radius.

### Multi-mode fibers

As their name implies, multi-mode fibers are optical waveguides supporting more than one guided mode (per polarisation direction) on a certain wavelength. Usually, their core size is or the order of $\sim 10 - 400$ μm and their NA is larger than of SMF, between $\sim$ 0.1-0.5.

The material of their core is often pure silica while the surrounding material, called the cladding, is index-raised with various dopants, such as fluorine, germania, phosphorus pentoxide and aluminosilicate. Around this structure, there is an additional buffer for protection of the fiber.

For the case of a step-index MMF and large values of $V$ and number of modes ($N_{\mathrm{MM}}$), an approximation to estimate the number of modes is given by (Snyder & Love 1984)

$$N_{\mathrm{MM}} = \frac{V^2}{4}. \tag{2.20}$$

For the case of optical fibers with a circular or square cross section, the modes are called TE and TM. As their name implies, there is a lack of either electric TE or magnetic TM fields in the propagation direction. Following that, the specific mode geometry is described by two suffix numbers; $\mathrm{TE}_{PL}$ and $\mathrm{TM}_{PL}$.

For a circular profile core where the mode geometry has circular symmetry, $P$ denotes the number of half-wavelengths along the radius, while $L$ stands for the number of half-wavelengths along the half-perimeter. Graphical presentation of the modal pattern is illustrated in Figure 2.9a. For the square cross section waveguides, the modal pattern is expressed by $\mathrm{TE}_{MN}$ and $\mathrm{TM}_{MN}$, where $M$ and $N$ stand for the number of half-wavelengths along the width and the height of the waveguide, correspondingly. In Figure 2.9b, the $\mathrm{TE}_{MN}$ modes of a square waveguide are presented.

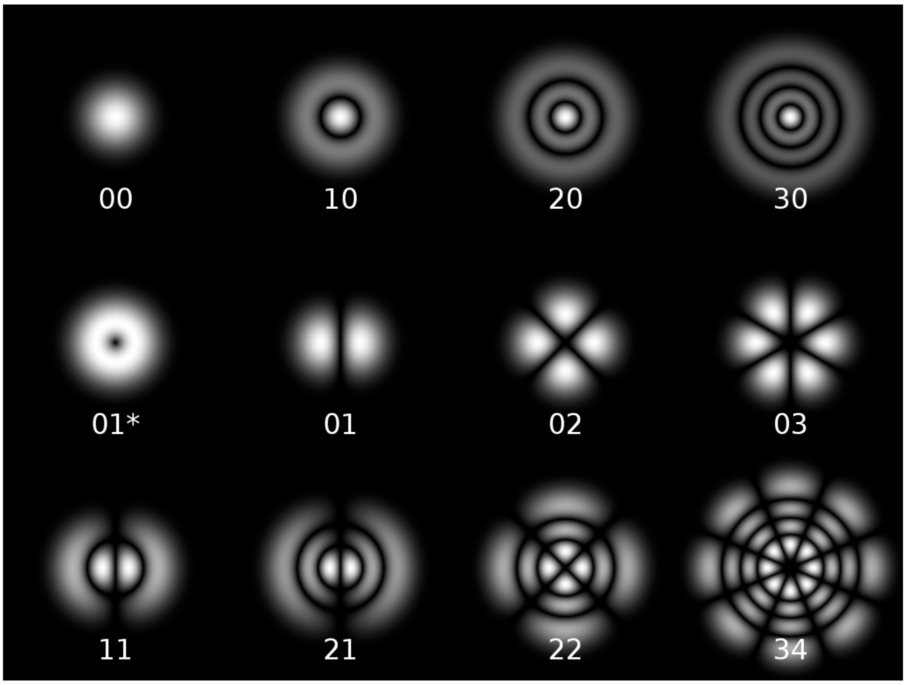
00
10
20
30
01*
01
02
03
11
21
22
34

(a)

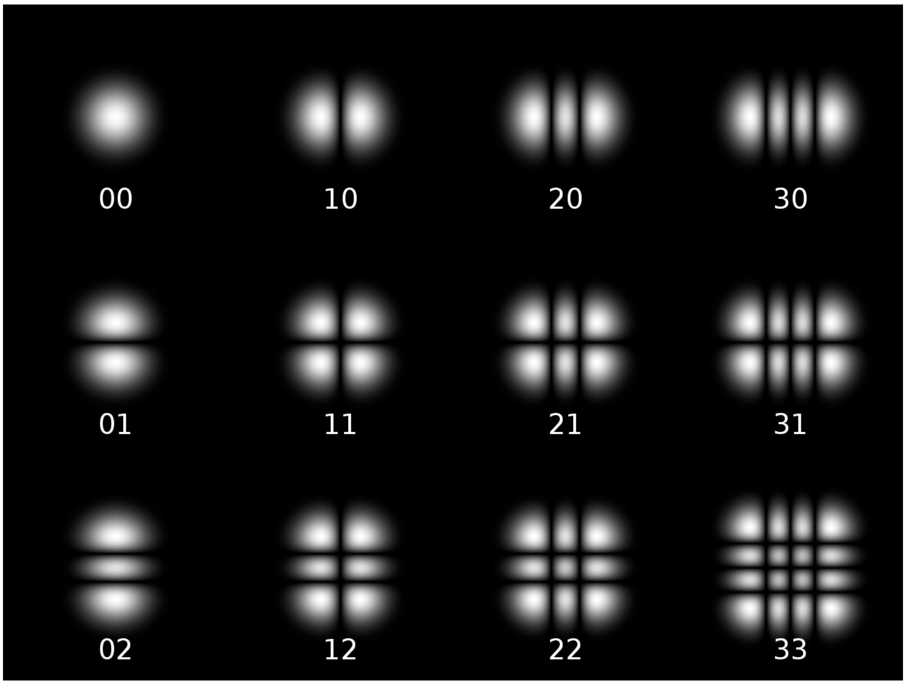
00
10
20
30
01
11
21
31
02
12
22
33

(b)

Figure 2.9: Graphical illustration of the intensity of the (a) $\mathrm{TE}_{PL}$ modes of a circular and (b) $\mathrm{TE}_{MN}$ modes of a square profile waveguide (Wikipedia 2019). Below each mode pattern the $P$ and $L$ number are given. These stand for the number of half-wavelengths along the radius and half-perimeter correspondingly for the circular waveguide and along the width and height correspondingly for the square waveguide. TM modes are the same but rotated by 90°.

### Focal ratio degradation

Focal ratio degradation (FRD) is the effect where the injected beam with a certain focal ratio to a fiber, degrades and increases at the output (graphical illustration is presented in Figures 2.10 & 2.11). It is caused by micro-irregularities in the structure of the fiber as well as additional mechanical stress on it, or improper polishing of the fiber (Ramsey 1988). In regards to the propagating modes into the fiber, the imperfection of the fiber's structure causes energy exchange between these modes, leading to FRD as well. In the case of a SMF where there is only one mode (neglecting polarisation), there is no energy transfer, thus there is no FRD issue.

For astronomical spectroscopic measurements, the focal ratio of the telescope to that of the instrument is matched using a variety of optics (Barden 1998). When a MMF is used to transfer the light from the telescope to the instrument, the optical design has to adapt to the fiber properties and its FRD in order to avoid the overfill of light into the collimator of the instrument which would result in loss of light.

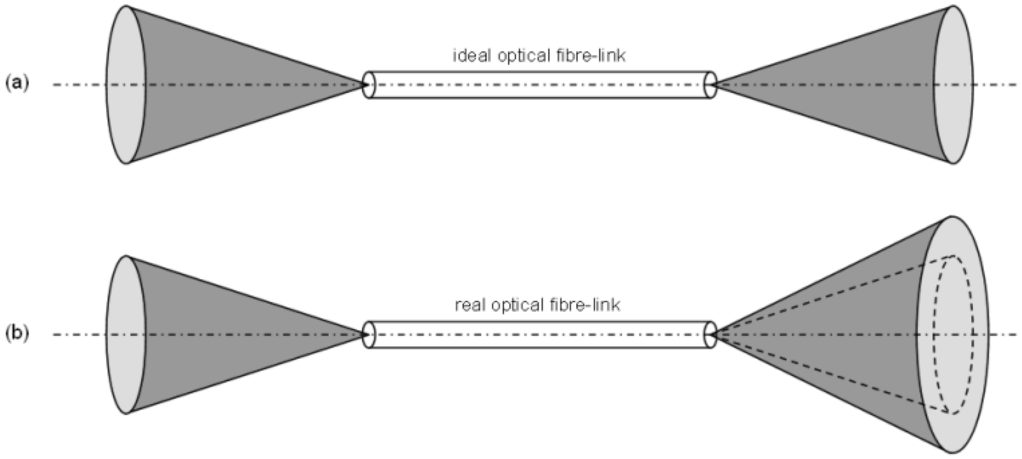

Figure 2.10: Illustration of FRD issue for the case of (a) an ideal fiber, and (b) for a MMF with FRD, making the output light-cone (right-one) wider than the entrance one (left-one). Image courtesy: Dr. Tobias Feger.

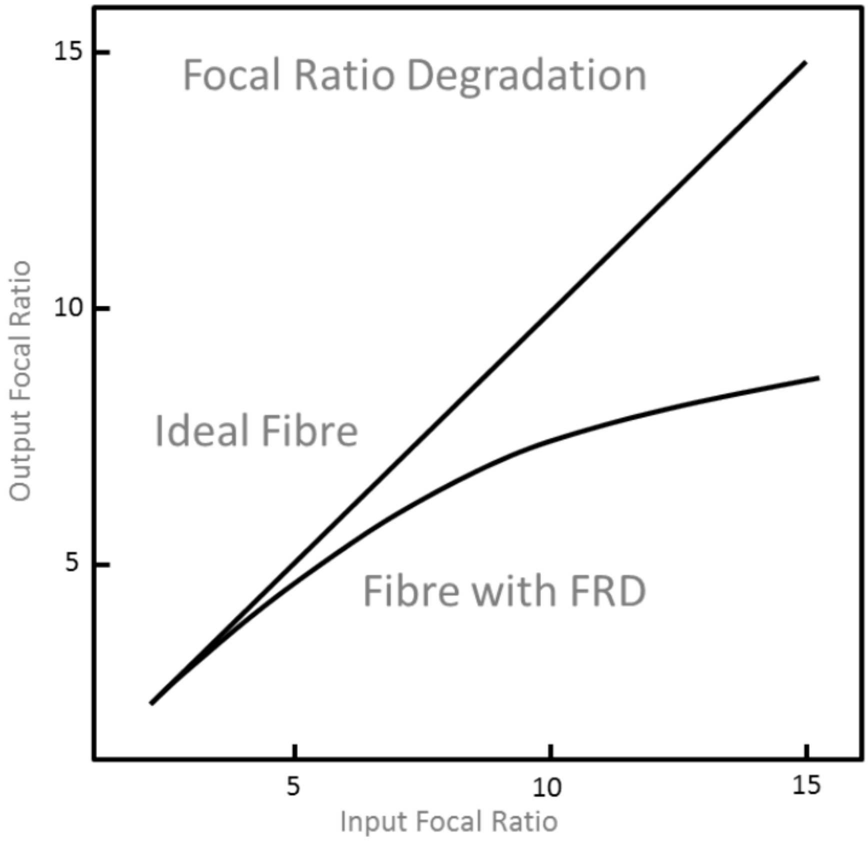

Figure 2.11: Illustration of FRD effect compared to an ideal MMF (NA=0.25) without it. The deviation of the output $f/\#$ as a function of injected $f/\#$ into the fiber is larger for a slower injected beam. Image courtesy: Barden et al..

### Spectral modal noise

In contrast to SMF where there is no modal noise at all, it is present in MMFs. Modal noise is created by the temporally varying output of such fibers due to interference between the propagating modes at a narrow bandwidth (Tremblay et al. 1981). The formed speckle pattern at the output of the MMF has variable levels of contrast depending on the (temporal) coherency of the light (Rawson et al. 1980). Once injected into the spectrograph, this causes a shift on the measured barycenter on a given wavelength is caused. This leads to noise in the measured wavelengths of spectral lines, and places a major limit on the precision of spectroscopic measurements while using MMF (e.g., Lemke et al. 2011; Perruchot et al. 2011; McCoy et al. 2012; Bouchy et al. 2013; Iuzzolino et al. 2014; Halverson et al. 2015). Furthermore, instabilities of the environment of the MMF (e.g. stress, temperature variations) affect the speckle pattern and place an upper limit on the achieved signal-to-noise ratio that is essential for high resolution spectroscopic measurements.

### Fiber mechanical agitation

One of the most commonly used methods to mitigate the spectral modal noise influence on the measurements is by using mechanical fiber agitators that shake the fiber in many different ways (azimuthally, radially) during the exposure (e.g., Olaya et al. 2012; Petersburg et al. 2018). By using this technique, the speckle patters are mixed together and the final, time averaged spectrum becomes smoother as illustrated in Figure 2.12.

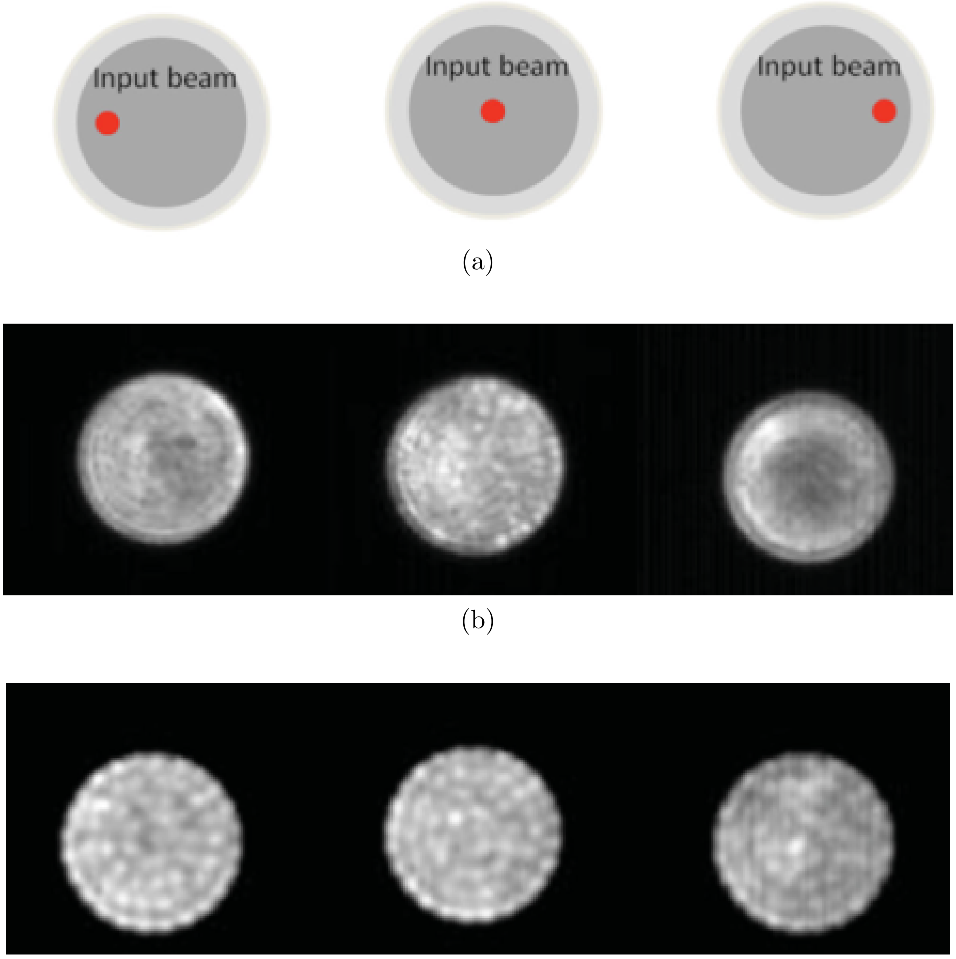

(a)

(b)

(c)

Figure 2.12: Graphical illustration of (a) the position of the injected beam to a typical MMF (Thorlabs - AFS105/125),(b) fiber near-field output with poor scrambling, (c) fiber near-field output with better scrambling. Image courtesy Olaya et al. (2012).

### 2.4.3 Spatial reformatters

The approximate number of spatial modes required for an efficient sampling of the FWHM of the telescope's PSF is proportional to the $D_\mathrm{T}^2$ given by (Harris et al. 2016)

$$M_\# \sim \left(\frac{\pi \chi D_\mathrm{T}}{4\lambda}\right)^2, \tag{2.21}$$

where this is valid for a circular cross-section fiber neglecting polarisation, and for a fully illuminated fiber in order to excite all the modes of the fiber.

As telescopes are built with ever-larger primary mirrors, the number of electromagnetic modes (tens of modes for a ∼4 m telescope in the H-band) increases and new observation techniques should be applied for sampling the PSF without high light losses. Observing towards the infrared wavelengths and using AO systems considerably reduces the number of modes compared to the seeing limited case. If multiple SMFs are used to sample all these spatial modes, the output field mode will be spatially stable, not suffering from modal noise. However, their relative small core size places major restrictions on the region of collected telescope light at its focal point, eliminating the benefits of this option. Alternatively, using an MMF improves the coupling of the light while having a relatively large fill factor area at telescopes focal point. However, the temporal instability of a field mode output suffering from modal noise and temporally varying speckle pattern increases the uncertainty of measurements, requires larger opto-mechanical components with careful calibration procedures and limits the spectral resolving power.

Aside from MMFs and SMFs, there are astrophotonic components that combine the advantages from these two regimes of fibers, the single-mode and the multi-mode. These devices retain a large sampling input and a more efficient coupling compared to SMFs, while they provide a more stable output than the MMFs offering a potential advantage to specific applications in astronomical observations. Namely, these are the astrophotonic components that are known as spatial reformatters, that fulfil the above benefits by geometrical positioning of the waveguides for a more efficient coupling of the starlight at their entrance, while the spatial shape of the input is reformatted to the required geometry at the exit.

### Photonic Lantern

Dictated by the second law of thermodynamics (or the conservation of degrees of freedom and consequent increase of the entropy) a SMF cannot sample more than one electro-magnetic spatial mode without huge loss. Conversely, coupling MM-light into waveguides with at least equal number of modes is possible. One spatial reformatter that satisfies these conditions is called the photonic lantern (PL). It is composed of at least two individual SM waveguides at one end while at the other end they form a MM cross section combined together. The first PLs were manufactured more than a decade ago (Leon-Saval et al. 2005). This was composed out of many individual SM waveguides merged together adiabatically to form a large MM waveguide (see Figure 2.13). Although it does not retain the spatial information of the image similar to a conventional image slicer, it offers a low-loss conversion between SM and MM systems (and vice versa). It also has the potential to sample the MM light from a telescope and reformat it to a linear pseudo-slit close to diffraction-limit for high resolution spectroscopic measurements.

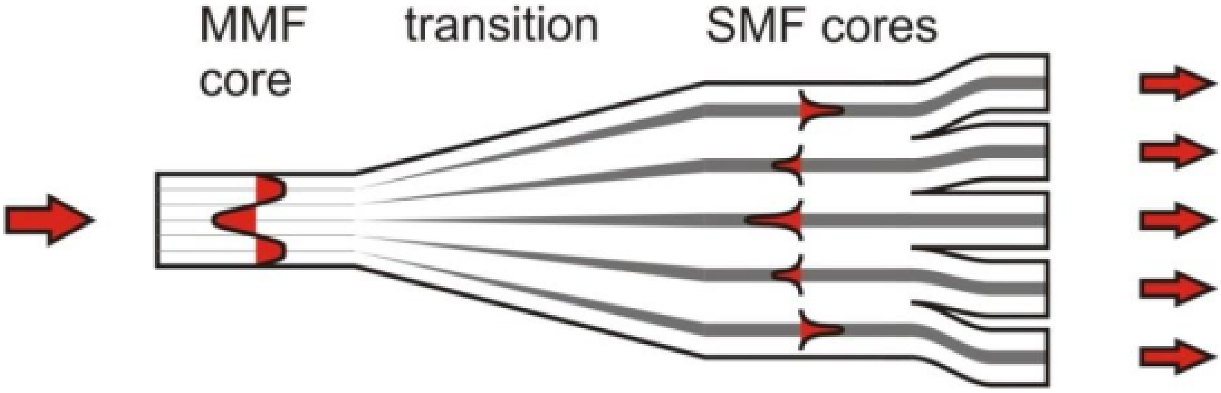

Figure 2.13: Illustration of a PL where the MM input, the transition zone and the SM sections are presented. Image courtesy: Birks et al. (2015).

Originally, the manufacture of the PL was motivated by the desire to have precise wavelength filters inscribed into the waveguides - known as fiber bragg gratings (FBGs) for the suppression of atmospheric OH emission lines (Bland-Hawthorn et al. 2008; Trinh et al. 2013). Their name was inspired by the Chinese lantern (see Figure 2.14).

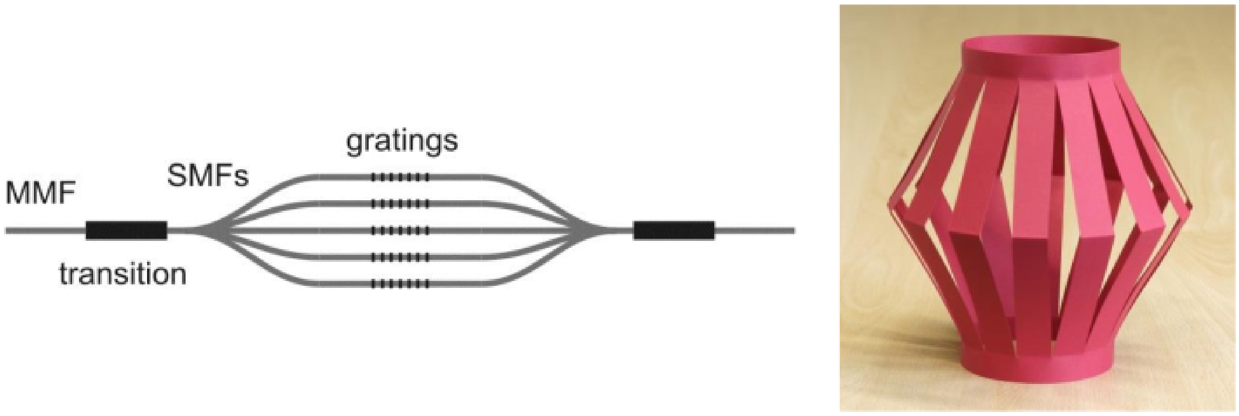

(a) (b)

Figure 2.14: (a) Illustration of a PL pair connected back-to-back together, having their MM cross-sections at the input and the output, while in between them, FBG filters are inscribed into the SMFs. (b) Example of a Chinese paper lantern. Image courtesy: Birks et al. (2015)

### Manufacturing methods and principles

There are currently two ways of manufacturing a PL (Birks et al. 2015). One way is by tapering down individual fibers so that the diameter of their cores decreases to the point where the propagating light cannot be further confined into their cores. Consequently, cross-talk between adjacent cores starts to happen and the light propagates through the cladding where it's surrounded by a lower refractive index material, forming an effective MM fiber core and creating the transition zone that bridges both SM and MM ends adiabatically (e.g., Leon-Saval et al. 2005; Noordegraaf et al. 2009, 2010). A schematic diagram and a real example can be seen in Figure 2.15.

The other way involves the rather novel direct laser inscription technique that modifies locally the refractive index of the substrate material in the 3D space by making use of ultra-fast pulsed laser system creating artificial integrated waveguides (e.g., Davis et al. 1996; Glezer et al. 1996; Thomson et al. 2009; Thomson et al. 2010; Harris et al. 2015). As a result of inscribing these waveguides close to each other, cross-talk starts to take place at this transition zone while the end of this section acts as the MM input/output of the PL. Using this technique, the individual waveguides can be inscribed with accuracy in the 3D space. Schematic descriptions of the technique, as well as a concept design of combined PLs structures, are presented in Figure 2.16.

In order to make an efficient (little loss of light) PL, there are two paramount requirements dictated by photonic theory. The first requirement is to keep the number of modes balanced for the MM and SM sections. In other words, that means the number of supported spatial modes on the MM end should be

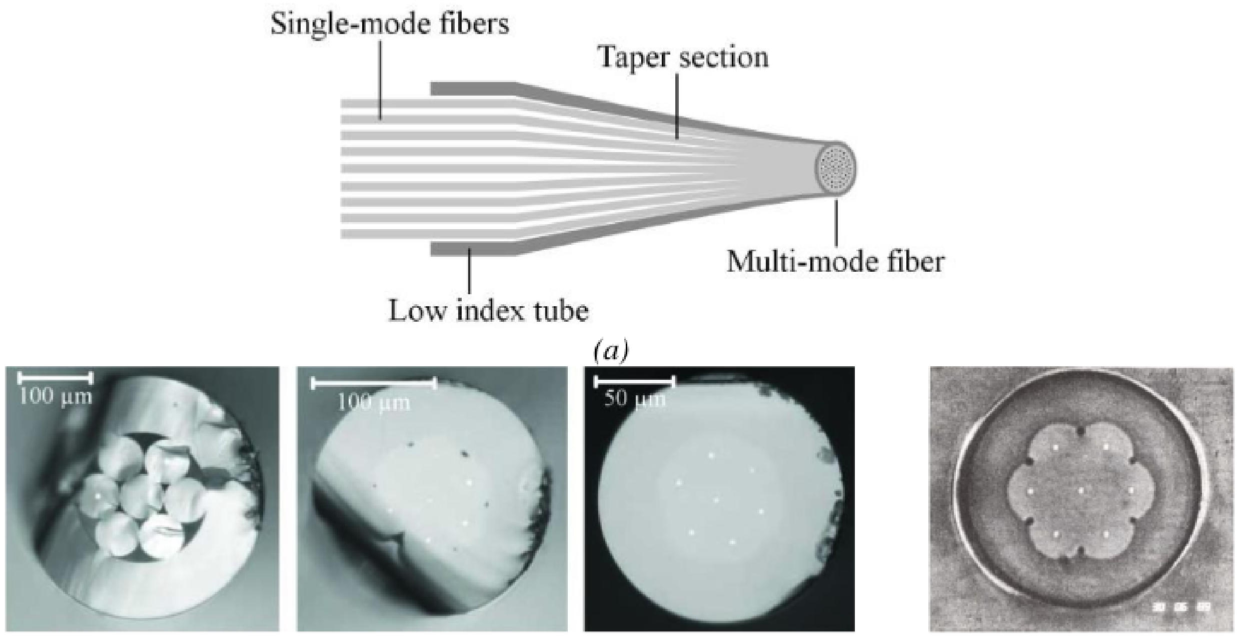
Single-mode fibers
Taper section
Multi-mode fiber
Low index tube
100 µm
100 µm
50 µm

(a)

(b)

(c)

Figure 2.15: Illustration of (a) a PL manufactured by tapering down individual SMFs surrounded by a lower refractive index tube, (b) Micrographs of the built PL at different cross-sections along the taper transition, where the seven individual fibers are distinguished at the leftmost frame while on the rightmost the have merged together to form the MM input, (c) cross-section of a 1×7 tapered-down coupler. Images courtesy: Birks et al. (2015).

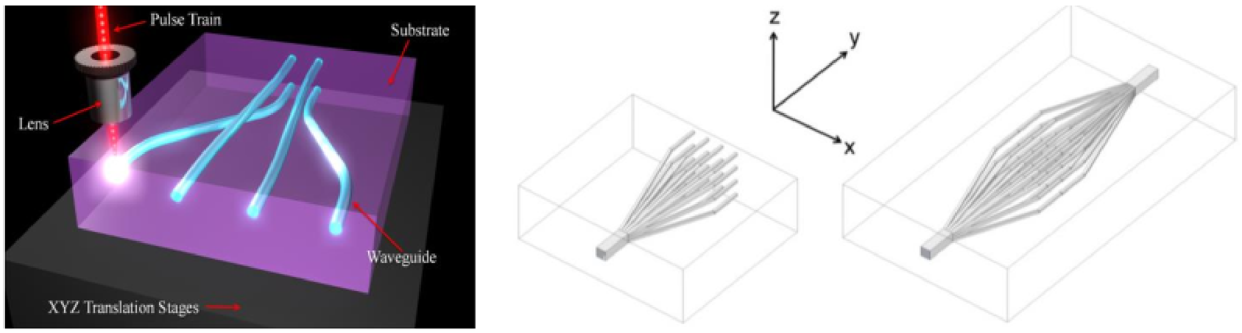
Pulse Train
Substrate
Lens
Waveguide
XYZ Translation Stages
z
y
x

(a)

(b)

Figure 2.16: Illustration of (a) the ULI method where the created waveguides are represented with blue colour, (b) (left) the PL manufactured by Thomson et al. (2011) with 16-waveguides in a square formation and (right) two identical PLs connected back-to-back. Image courtesy: Birks et al. (2015).

equal to the number of SM waveguides at the other end. The second crucial requirement to limit the loss of light in the device, is to have a well-designed transition zone between both sections, ensuring that is adiabatic. The term adiabatic refers to a gradual enough transition of the core size and the in-between distance of the individual waveguides from the MM end to the SM end. During this reverse process, the propagated light becomes more confined to the fiber's core the bigger its diameter or the more the distance between the fibers, leaving none in the higher-order cladding modes. Following this gradual transition phase of the waveguide's transformation, the spatial mode remains the same despite the local changes during the transition phase (Snyder & Love 1984; Love 1987; Bilodeau et al. 1988; Chang et al. 2003). A schematic description of the above is presented in Figure 2.13.

### 2.4.4 Propagated light simulation - wave model analysis

Simulation tools are of paramount importance in designing optical components, saving manufacturing time and cost while optimising performance. One of the most important tools especially for mediums such as fibers and integrated optics, is the well-known beam propagation method (BPM) which simulates the propagated light through them, showing their ideal potential (Roey et al. 1981). BPM approximates numerical solutions of the exact wave equation for a slowly varying geometry of waveguides and shares many similarities with the parabolic equation, which is more applicable to hydro-acoustics field (Radder 1979). It is limited to the monochromatic wave equation solution of a scalar field (neglects polarization phenomena) and for a narrow range of propagation angles (paraxiality). However, using particular approximations these limitations may be removed.

Starting with the Helmholtz equation for monochromatic waves fields in 3D space

$$\begin{gathered}\nabla^2\phi + k(x,y,z)^2\phi = 0,\\ \frac{\partial^2\phi}{\partial x^2} + \frac{\partial^2\phi}{\partial y^2} + \frac{\partial^2\phi}{\partial z^2} + k(x,y,z)^2\phi = 0,\end{gathered} \tag{2.22}$$

where the scalar electric field is $E(x,y,z,t) = \phi(x,y,z)e^{-i\omega t}$, the spatially independent wavenumber is $k(x,y,z) = k_0 n(x,y,z)$, the refractive index distribution of the medium is $n(x,y,z)$ and $k_0 = 2\pi/\lambda$ is the wavenumber in the free space.

After the factorisation of the quickly varied phase of the field ($\phi$) as it propagates along to the z-axis, the field is given by

$$\phi(x,y,z) = A(x,y,z)e^{i\bar{k}z}, \tag{2.23}$$

where the $A$ is the slowly-varying field and $\bar{k}$ is the average phase variation of the field constant (reference wavenumber). Substituting equation 2.23 to equation 2.22 it changes to

$$\frac{\partial^2 A}{\partial z^2} + \frac{\partial A}{\partial z}2\bar{k}i + \frac{\partial^2 A}{\partial x^2} + \frac{\partial^2 A}{\partial y^2} + A(k^2 - \bar{k}^2) = 0. \tag{2.24}$$

Staring with an input field $A(x,y,z) = 0$, one can solve the equation 2.24 iteratively and derive the electric field (amplitude and phase) in space (z>0).

Implementation of the BPM is offered commercially by various software tools, such as `BeamPROP` by `RSoft` (Synopsys 2018) and `OptiBPM` by `Optiwave` (OptiBPM 2020).

# Chapter 3

# Simulation and optimisation of the photonic dicer

In this chapter, I simulate the photonic dicer (PD) (Harris et al. 2015), by optimising its throughput and geometrical design using `Soapy` and `BeamProp` simulation software. The PD was tested on-sky by Harris et al. (2015) and is an astrophotonic spatial reformatter that re-arranges the sampled PSF in the focal plane of a telescope into a close-to-diffraction-limited pseudo-slit output (see Section 2.4.3). It has the potential to further increase the precision of high-resolution spectroscopic measurements of astronomical sources, where precise spatial information is not required.

The PD finds application in the seeing limited observing conditions where it relaxes the dependence of the spectrograph size on the telescope diameter feeding it as shown by equation 2.11 for high spectral resolving power measurements. The device does not preserve imaging information, however for the purposes of high resolution spectroscopy this is not a problem.

In Section 3.1 the configuration parameters taken into account for the simulated version of the PD are presented, followed by the results, the procedure that was followed and the techniques used for the optimisation in Section 3.2. The results are discussed in Section 3.3 and concluded in Section 3.4.

The chapter is largely drawn from Anagnos et al. (2018a).

## 3.1 Methods

In order to calibrate future designs and test their potential, realistic simulation conditions are required. For this work two tools were combined to simulate the PD's on-sky performance.
`Soapy` (Reeves 2016), a Monte Carlo AO simulation program, is used to model the atmosphere and yielding the amplitude and phase of the star at the focal point of a telescope. Having this crucial information is of paramount importance to the performance of the PD. The other tool, a commercial finite-difference beam propagation solver known as `BeamPROP` by `RSoft` Synopsys (2018), is used to model the PD itself and how the beam propagates through it.

Two different approaches were used to perform the simulations: at first, `Soapy` was used to determine an AO-corrected output beam with amplitude and phase information at the focal point of the telescope, which could then be used as an input for the `BeamPROP` software, and secondly using the on-sky data (Intensity information of the beam only) from Harris et al. (2015) as the input (real). In order to identify areas of improvement, these two methods are compared.

### 3.1.1 `Soapy` Configuration

`Soapy` is a module specifically written in Python's object oriented programming environment making use of Monte Carlo techniques for AO simulations. It can be simply be operated just by using a configuration file where input parameters are stored. Figure 3.1 illustrates the graphical user interface (GUI) that can be used instead of a purely Python script.

`Soapy` was configured to approximate the CANARY (Myers et al. 2008) parameters used on-sky for the PD tests (see Table 3.1). The simulation was run in the same three AO modes as used on-sky, namely closed-loop, tip-tilt and open-loop. To match the on-sky AO performance the seeing parameter (Fried parameter - $r_0$) was set to a range of 0.09 to 0.11 m, which is representative of the conditions encountered during the on-sky experiments described in Harris et al. (2015).

In the first step, `Soapy` is used to produce 12,000 NIR data frames, each with an exposure time of 6 ms (150Hz) as they were on-sky. The science camera parameters of the `Soapy` output frames were 128x128 pixels with a sky angular dimension of 3.0 arcseconds, just under ten times the angular size of the PD on-sky. Unlike the on-sky camera data, these frames contain both phase and amplitude

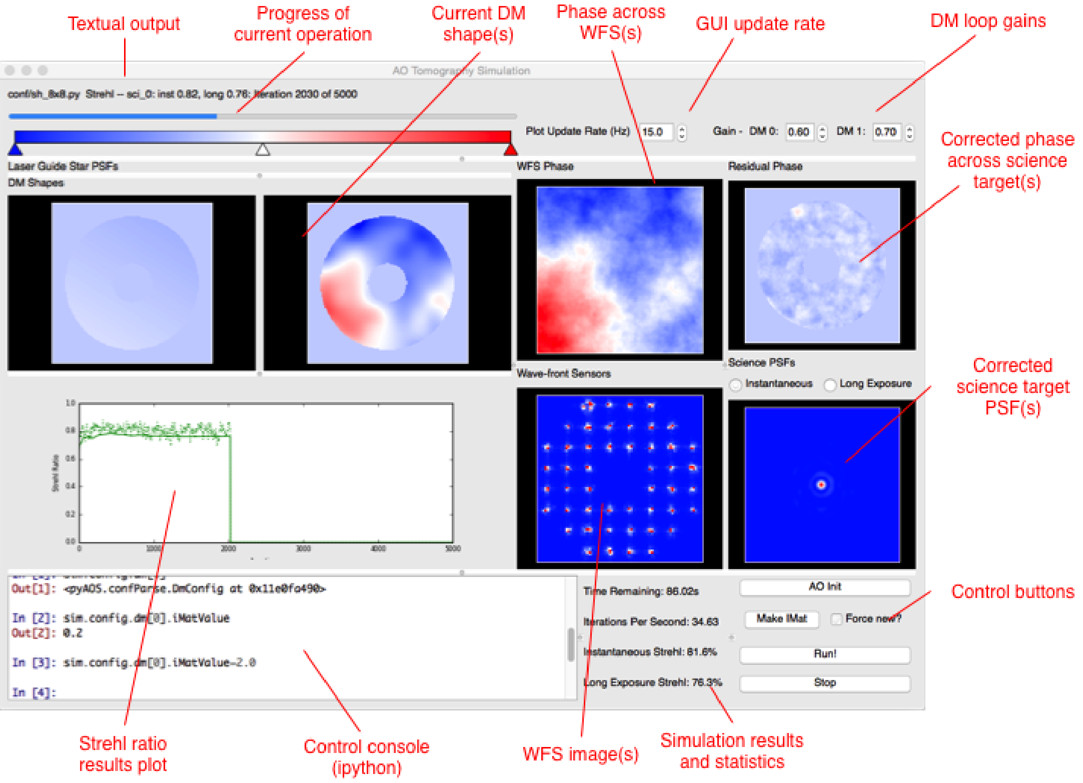
Textual output
Progress of current operation
Current DM shape(s)
Phase across WFS(s)
GUI update rate
DM loop gains
Corrected phase across science target(s)
Corrected science target PSF(s)
Control buttons
Strehl ratio results plot
Control console (ipython)
WFS image(s)
Simulation results and statistics
AO Tomography Simulation
Laser Guide Star PSFs
DM Shapes
WFS Phase
Residual Phase
Wave-front Sensors
Science PSFs
○ Instantaneous
○ Long Exposure
AO Init
Make IMat
☐ Force new?
Run!
Stop

conf/sh_8x8.py Strehl -- sci_0: inst 0.82, long 0.76: Iteration 2030 of 5000

Plot Update Rate (Hz) 15.0

Gain - DM 0: 0.60 DM 1: 0.70

```
Out[1]: <pyAOS.confParse.DmConfig at 0x11e0fo490>

In [2]: sim.config.dm[0].iMatValue
Out[2]: 0.2

In [3]: sim.config.dm[0].iMatValue=2.0

In [4]:
```

Time Remaining: 86.02s

Iterations Per Second: 34.63

Instantaneous Strehl: 81.6%

Long Exposure Strehl: 76.3%

Figure 3.1: Illustration of the `Soapy` GUI including description of its individual display panels. Image courtesy: Reeves (2016).

information, which was found to be essential to the simulation accuracy and is detailed in Section 3.2.1. These `Soapy` frames were used as an input to `BeamPROP`.

## 3.1.2 `BeamPROP` Configuration

Following the procedure, each frame from `Soapy` was then used as an input for `BeamPROP`; the angular size of the PD in `BeamPROP's` simulation domain was set to 321 mas. For these simulations the PD architecture was as described in MacLachlan et al. (2014) and is presented in Figures 3.4 & 3.2 as designed in `RSoft's` CAD environment. As thoroughly explained in Section 2.4.4, `BeamPROP` requires the information of refractive indices for both the core and cladding of the optical device under simulation. The cladding substrate is a borosilicate glass (Corning, EAGLE2000), which has a refractive index $n_{\mathrm{cl}}$ of ∼1.49 at 1550 nm. As no refractive index measurements were made of the waveguides in the PD, this value is adopted from Thomson et al. (2011). Consequently, the refractive index difference value $\Delta = \frac{n_{\mathrm{core}} - n_{\mathrm{clad}}}{n_{\mathrm{core}}} \approx 1.76 \times 10^{-3}$, is expected to be close to the waveguides in the PD, but due to differences in the inscription parameters, small variations are possible (see Table 3.2).

| | Modes of AO operation | | |
|---|---|---|---|
| | closed-loop | open-loop | tip-tilt |
| Parameters | | | |
| Seeing (arcsec) | 1.03 | 0.94 | 1.15 |
| Instantaneous Strehl ratio (mean) | 0.26 | 0.08 | 0.07 |
| Long exposure Strehl ratio (mean) | 0.12 | 0.01 | 0.01 |
| Fried parameter $r_0$ (m) (@1550 nm) | 0.1 | 0.11 | 0.09 |
| Atmosphere layers | 5 | 5 | 5 |
| DM integrator loop gain tip-tilt | 0.3 | 0.001 | 0.3 |
| DM integrator loop gain Piezo | 0.3 | 0.001 | 0.001 |

Table 3.1: Simulation `Soapy` input parameters

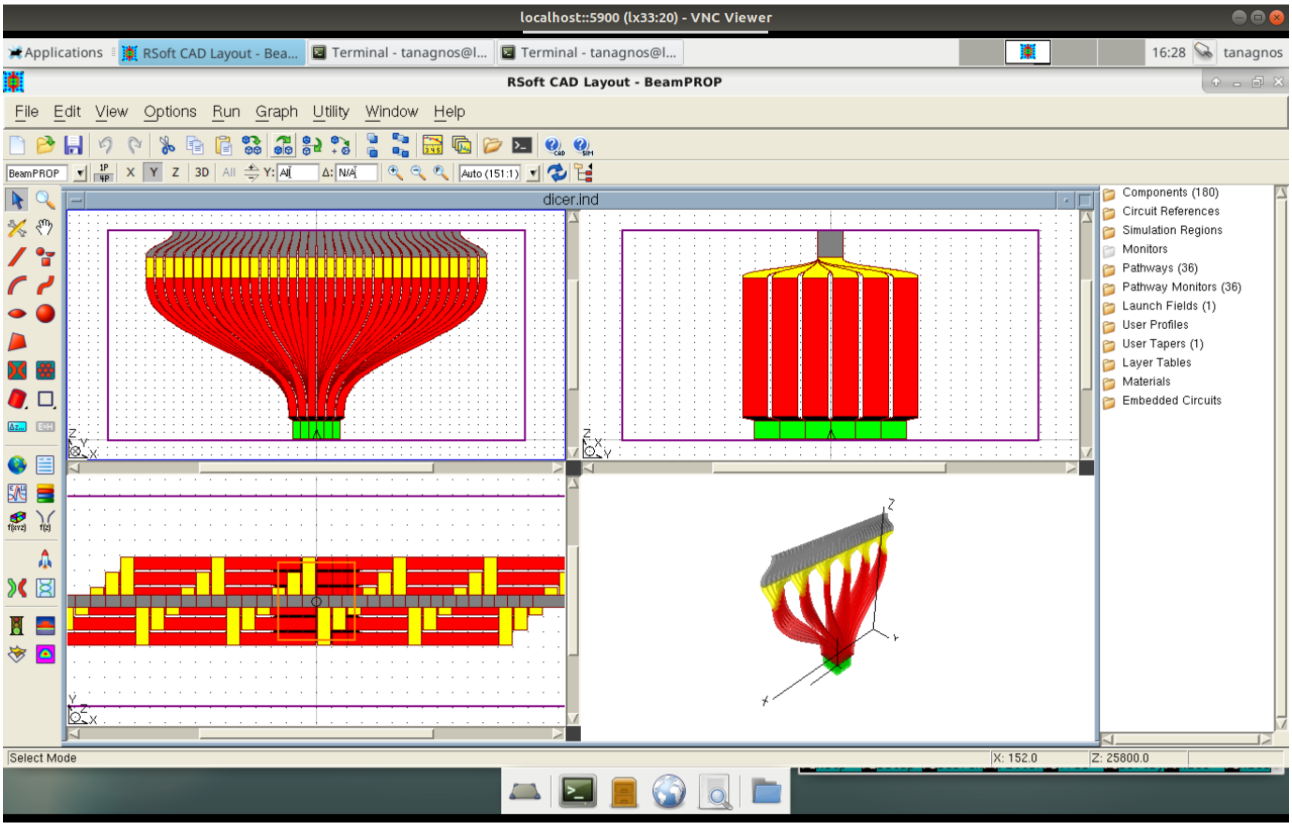
localhost::5900 (lx33:20) - VNC Viewer
Applications
RSoft CAD Layout - Bea...
Terminal - tanagnos@l...
Terminal - tanagnos@l...
16:28
tanagnos
RSoft CAD Layout - BeamPROP
File
Edit
View
Options
Run
Graph
Utility
Window
Help
BeamPROP
X
Y
Z
3D
All
Y: All
Δ: N/A
Auto (151:1)
dicer.ind
Components (180)
Circuit References
Simulation Regions
Monitors
Pathways (36)
Pathway Monitors (36)
Launch Fields (1)
User Profiles
User Tapers (1)
Layer Tables
Materials
Embedded Circuits
Select Mode
X: 152.0
Z: 25800.0

Figure 3.2: Illustration of the photonic dicer structure as it appears in `RSoft` CAD.

| Parameters | Thomson et al. | Harris et al. |
|---|---|---|
| $n_{\mathrm{cl}}$ (@1550 nm) | $\sim 1.49$ | $\sim 1.49$ |
| Pulse Energy (nJ) | 165 | 251 |
| Pulse repetition rate (kHz) | 500 | 500 |
| Pulse duration (fs) | 350 (1047 nm) | 460 (1064 nm) |

Table 3.2: Comparison of ULI inscription parameters used in Thomson et al. and Harris et al.

By default, `BeamPROP` does not take into account the material propagation loss. For the simulations, I ran tests using losses of 0.1 dB/cm that are in agreement with the behaviour of the substrate's reported characteristics in the literature (Nasu et al. 2005), though this was shown to be small in comparison to the losses due to geometrical changes (<2 % over the PD length). However, this will need to be taken into account in future modelling with more efficient devices.

To increase the accuracy of the simulations, introducing noise to the step refractive index profile of the waveguides was considered, similar to that measured by Thomson et al. (see Figure 3.3 for a graphical representation). This greatly increased simulation time and the differences in efficiency between noisy and noiseless waveguides were found to be minor - less than 0.001%. Thus simulations were performed without taking into account noise in the refractive index profile of the waveguides to minimise the computation time. The complete input starting parameters of `BeamPROP` simulation are presented in Table 3.3.

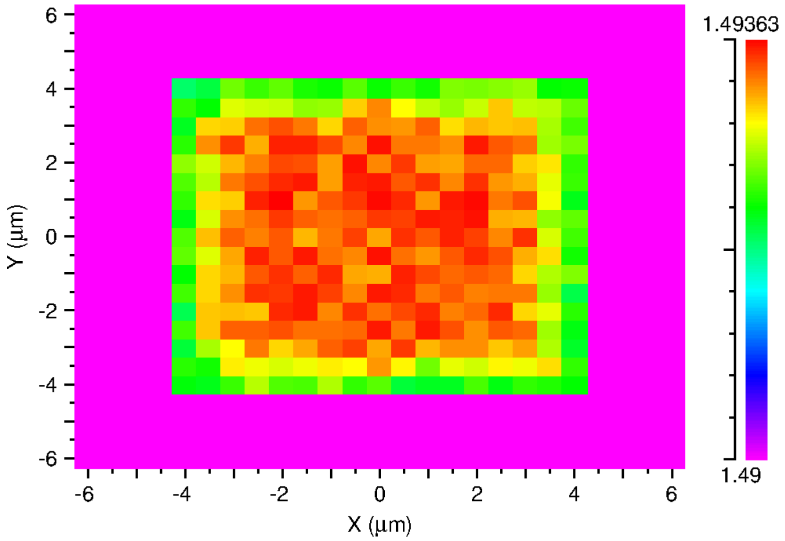

Figure 3.3: Colour map showing the refractive index profile of a noisy waveguide of the photonic dicer.

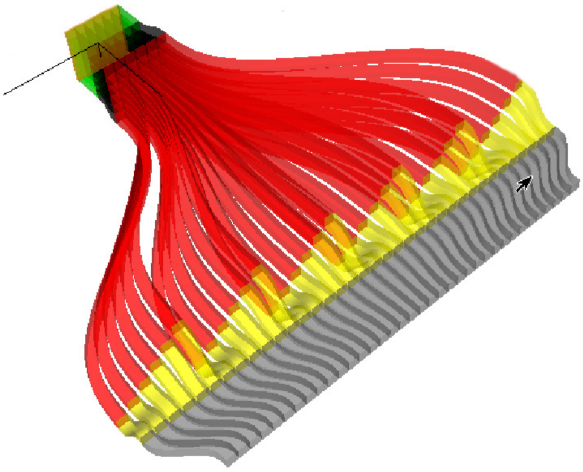

Figure 3.4: The photonic dicer 3D design in the `RSoft` CAD environment. The colours indicate the 5 different transition planes used to reform the square input (green colour) to a linear slit output (grey colour).

| Parameter | Value | Comment |
|---|---|---|
| Wavelength | 1550 nm | Wavelength of operation |
| Background index | 1.49 | Refractive index of the glass Eagle 2000 |
| $\Delta_\mathrm{n}$ | 0.002627024 | Refractive index difference between the core and the substrate |
| Domain Min/Max | ±219 μm | Spatial domain of the simulation field |
| Grid size | 0.5 μm | Convergence study optimum result for accurate simulations |

Table 3.3: Simulation domain initial parameters of `RSoft` for the PD.

### 3.1.3 Throughput calculation

In order to calculate the total throughput ($T_\mathrm{tot}$) of the PD, the ratio of the flux in the slit output ($F_\mathrm{slit}$) to that of the input field ($F_{\mathrm{ref}\star}$) was taken for each of the science frames. As `BeamPROP` does not take into account any size differences in images, a constant $k$ is used to normalise the input and output spatial sizes of the fields as they were different; this results in

$$T_\mathrm{tot} = \frac{F_\mathrm{slit}(i)}{F_{\mathrm{ref}\star}(i) \times k}, \quad i = \#frames. \tag{3.1}$$

### 3.1.4 Photonic dicer plane optimisation

The PD was designed in 2013 (MacLachlan et al. 2014), without the ability to do the full system modelling using a similar to this software suite. This means that there are potential optimisation possibilities that were not taken into account. To investigate this, I use a Monte Carlo simulation routine built into `BeamPROP` to calculate the relative losses for different propagation planes (see Figure 3.4), changing the size of the PD (in the simulation domain) to the optimal one.

In order for the transitions to have low losses, they should be gradual (Birks et al. 2015). However, as using ULI results in relatively high material and bend losses, these transition losses need to be balanced against length. Simulation results for the optimal device (see Figure 3.10) show that the optimal PD length is shorter than the constructed one by several mm, leading to greater throughput and a more compact design.

## 3.2 Results

### 3.2.1 Throughput performance results

In this section, the throughput results are presented from the simulation configurations as described in Section 3.1. As stated above, the `Soapy` AO modes were configured to approximate the on-sky corresponding performance. Consequently, the tip-tilt AO mode was adjusted to perform worse than the open-loop case, in terms of correction similarly to what was experienced on-sky due to seeing effect, by regulating the seeing/Fried parameter in our simulations (see Table 3.1). Hence, simulations were performed using the produced `Soapy` data (phase and amplitude information provided) and real on-sky images acquired in the focal plane at the input of the PD provided by CANARY (Myers et al. 2008). As Canary uses an InGaAs camera only intensity is recorded, therefore for the simulations a flat phase front (all phase = 0) and the square root of the intensity (amplitude) is used.

As presented in Figure 3.5, depending on the operating AO mode, there is a difference in the distribution of the light output at the exit slit of PD. A schematic representation of how the light propagates through different view-angles of the PD is illustrated in Figure 3.6.

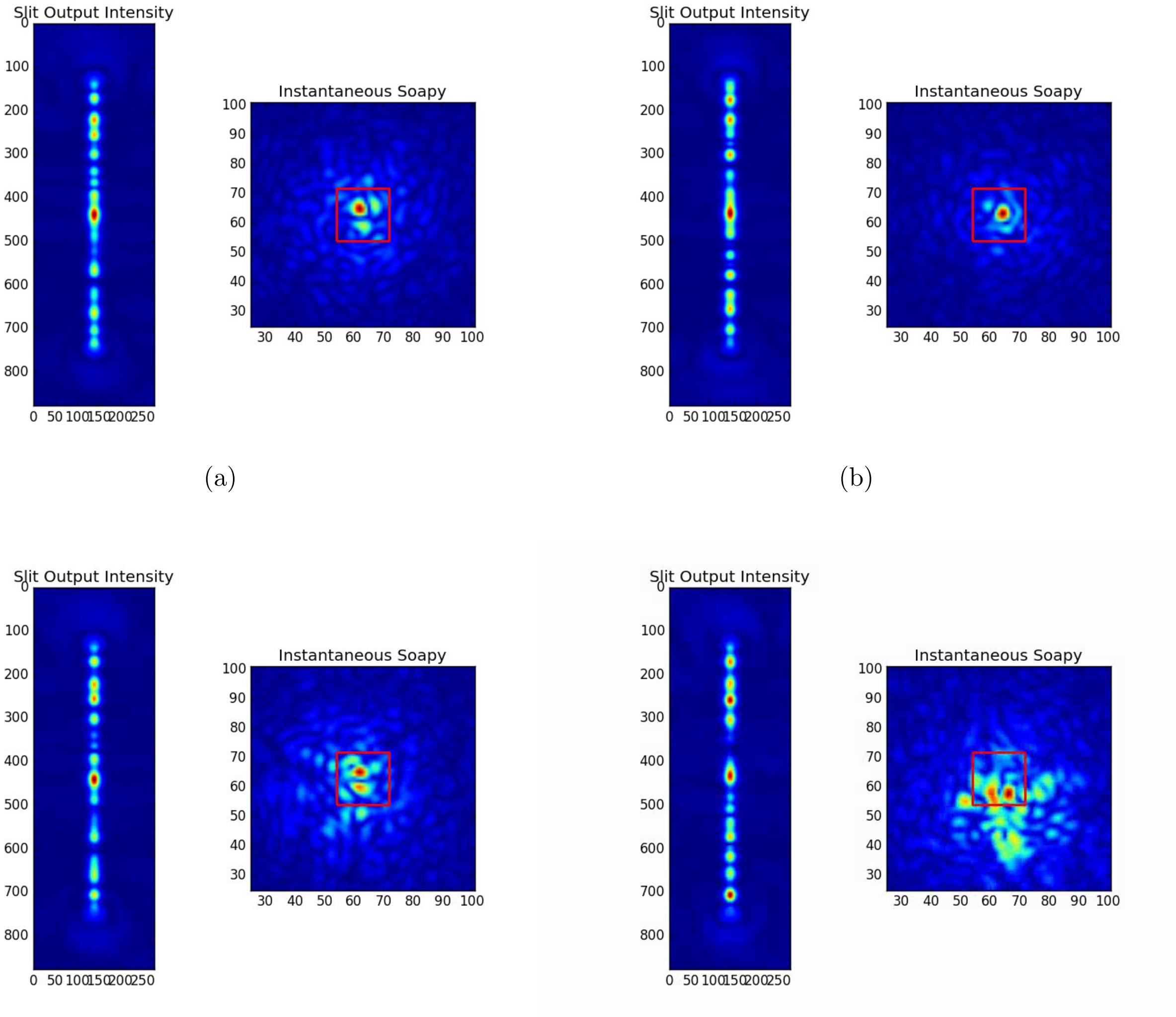

(a)

(b)

(c)

(d)

Figure 3.5: Graphical illustration of Soapy output beam to the square entrance of the photonic dicer (red square) at the right side of the sub-frames, with its corresponding slit output of photonic dicer on the left of the sub-frames, (a-b) with close-loop AO correction at two different times, (c-d) same as before but for the case of open-loop correction AO mode. Colours indicate the relative normalised intensity of the light.

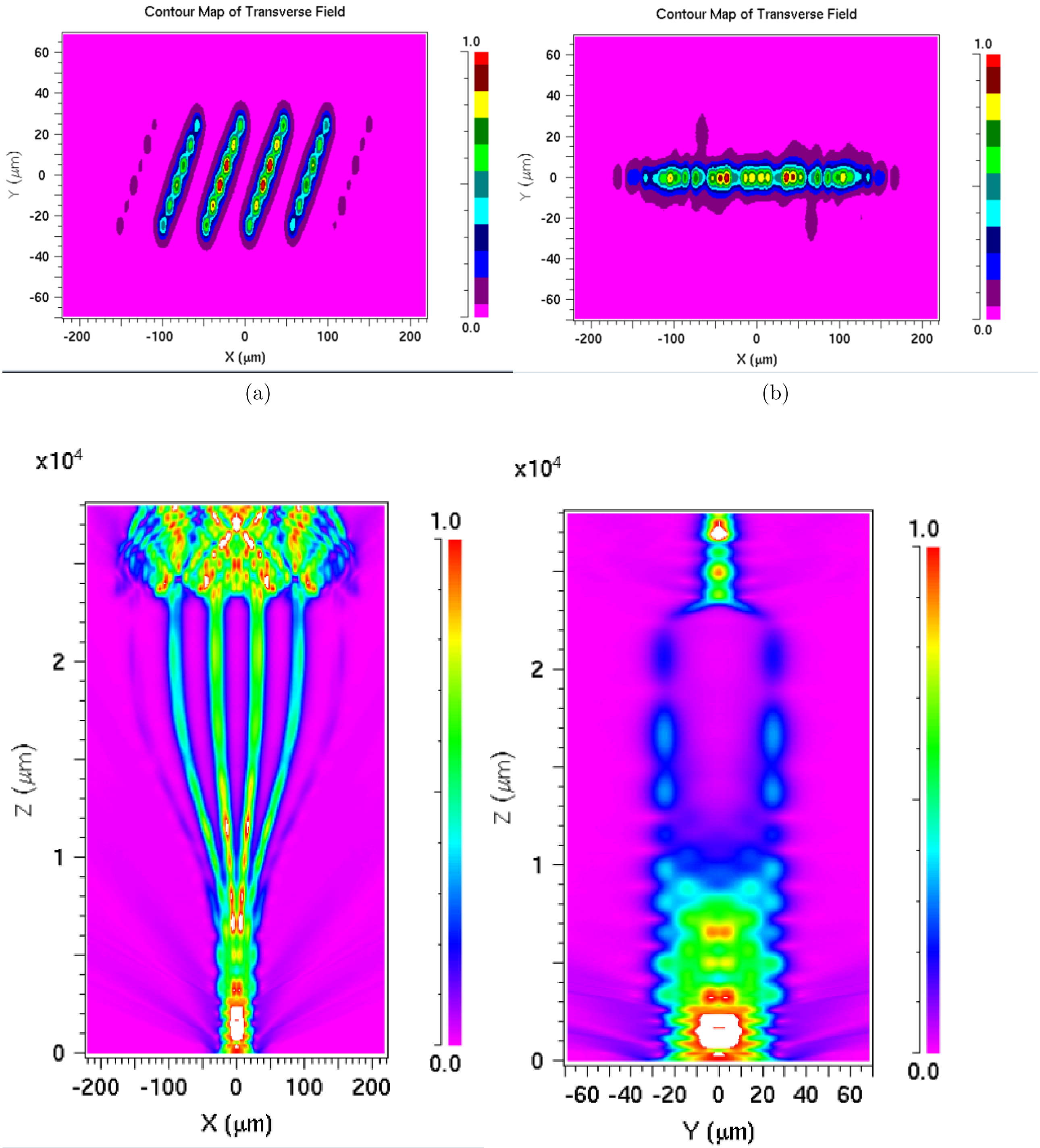

(a) (b)

(c) (d)

Figure 3.6: Graphical illustration of light propagation through the photonic dicer as displayed by `RSoft`'s simulation CAD environment. (a-b) cross-section of photonic dicer plane where the waveguides reform towards a linear array output (see Figure 3.4), (c-d) Top and side view of the same simulation as the light propagates on the z-axis. Colours indicate the relative normalised intensity here.

The results of simulating 12,000 frames are shown in Figure 3.7. For closed-loop operation mode where there was operating full AO correction, the transmission of the PD was measured to be 20 ±2 (%). In open-loop operation mode the transmission was measured to be 8 ±2 (%); and for tip-tilt correction results shown to be 9 ±2 (%).

The camera data taken from the on-sky run (real) were also simulated by `BeamPROP` and the results are shown in Table 3.4. This shows an overestimation of the throughput by a factor of ∼2. The reason of this overestimated result is the absence of phase information in the on-sky data fields and as a consequence `BeamPROP` considers zero-phase everywhere.

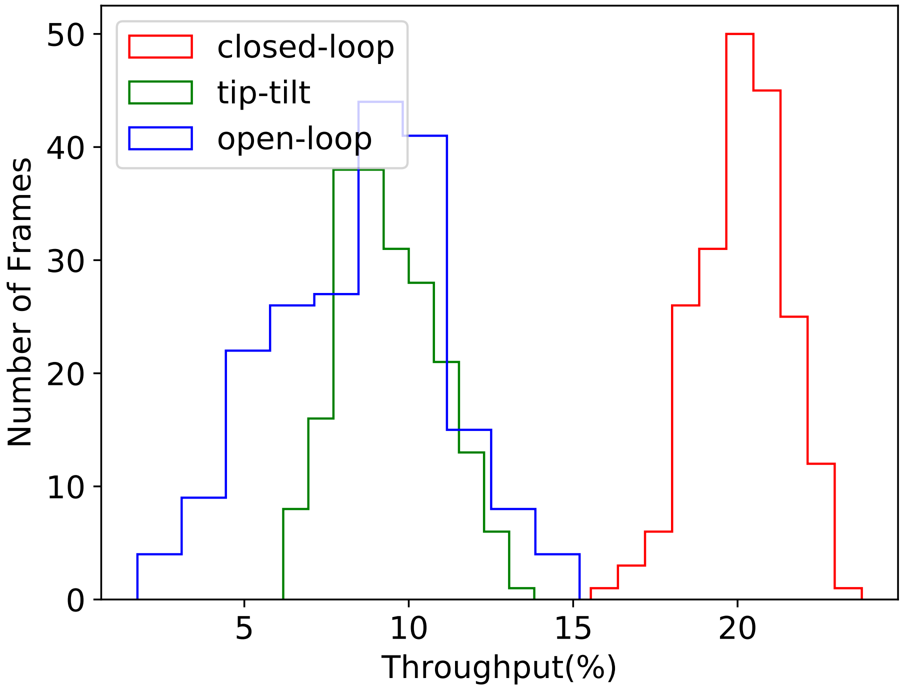

Figure 3.7: Histogram plot of throughput measurements in the three different AO modes, with each mode containing 12,000 simulation results binned by a factor of 60. In order of correction, red shows closed-loop, green tip-tilt correction and blue shows open-loop.

As with Harris et al. (2015) I also investigated the ratio of output power in the slit to input power coupled to the PD, in order to calculate a value of light transmitted through the PD. To do this the ensquared energy (EE) at the input of the PD was calculated and plotted against the corresponding throughput. Figure 3.8 shows the result of this; as in Harris et al. (2015) I observed a positive linear correlation of EE with the calculated slit output power. The black line shows where the input EE and output throughput are equal. Some values are close to equal; this is due to evanescent field coupling which is further explained in section 3.3.3.

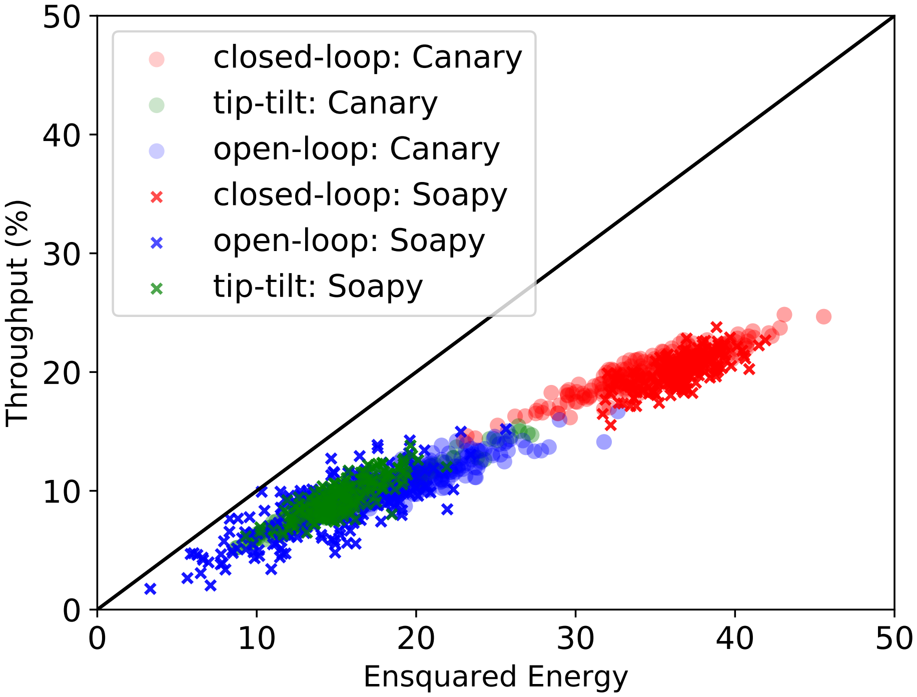

Figure 3.8: Throughput measurements of the simulated photonic dicer slit end versus the amount of light coupled at 321 mas (the square entrance of the device as configured in `BeamPROP`). This is shown for the simulated data of `Soapy` (bold colour) and on-sky results (transparent) in all three AO operating modes. Note that the number of points are binned by a factor of 60 into 200 points from the 12,000, for each AO mode.

For a better understanding of the coupling efficiency EE, the ratio between closed-loop and tip-tilt correction was calculated and plotted versus the device MM entrance input size for averaged `Soapy` and real data images (Figure 3.9). This figure illustrates that the EE under closed-loop mode is higher than that of tip-tilt by a factor of $\sim 2.8$ for real and $\sim 2.4$ for `Soapy` data. This factor varies inversely with the spatial size of the sampling as a function of overall throughput.

| | Data and results | | |
|---|---|---|---|
| AO mode | On-sky | `Soapy` +`BeamPROP` | On-sky +`BeamPROP` |
| closed-loop (%) | 20 ± 2 | 20 ± 2 | 45 ± 2 |
| tip-tilt (%) | 9 ± 2 | 9 ± 2 | 20 ± 2 |
| open-loop (%) | 11 ± 2 | 8 ± 2 | 24 ± 2 |

Table 3.4: Fractional throughput results comparing theoretical simulations and on-sky conditions. The incorrect results for real measured input data + `BeamPROP` show a factor of two overestimation because `BeamPROP` assumes zero phase if phase information is not provided; this highlights the importance of having phase information of the input beam in the simulations.

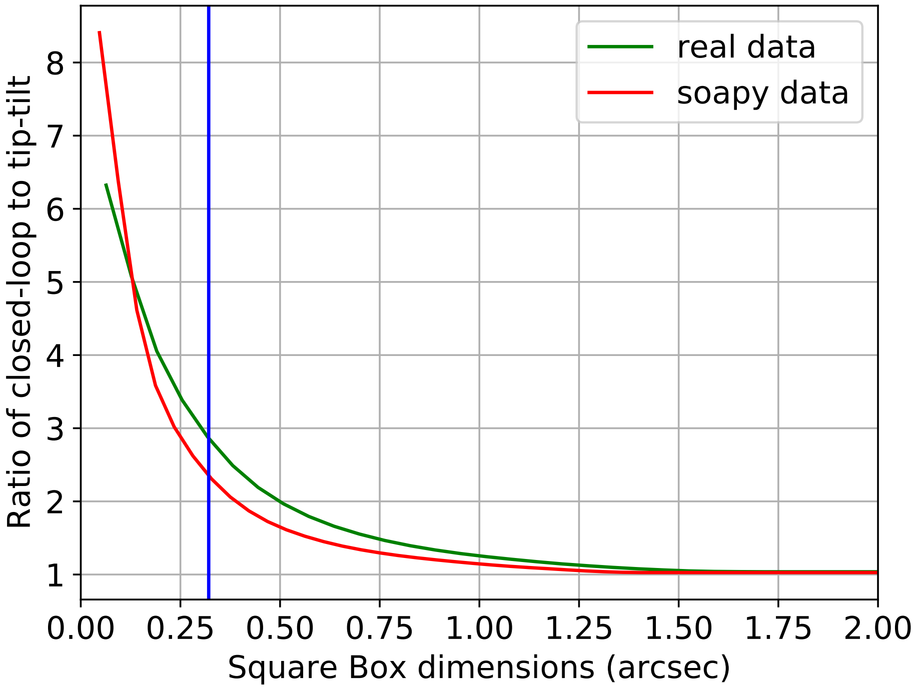

Figure 3.9: The relation of closed-loop and tip-tilt AO mode ratios of ensquared energy as a function of spatial scale (square box centred), plotted for both simulated (`Soapy`) and on-sky averaged data (real). The photonic dicer square entrance size is represented by the blue vertical line.

### 3.2.2 Optimisation results

In order to optimise the PD, the average of the real and imaginary parts of the electric field of the frames from a closed-loop dataset by `Soapy` was chosen. Using this as an input, a Monte Carlo simulation was performed on the PD, optimising each of its transition planes for throughput by scanning for different lengths among the 5 transition planes of the device. The results of this are shown in Figure 3.10. In this figure, throughput results from simulations with the optimised and unoptimised versions of the PD using all of the three AO modes as an input are plotted against the propagation length of the device. The solid and dashed lines represent the unoptimised and optimised PD, respectively. In this illustration it can be observed the shorter more efficient version of the PD, as well as the high coupling losses at the entrance input of the device, where the PL section is located. That means the transition can be further improved to be more adiabatic and thus lower in loss.

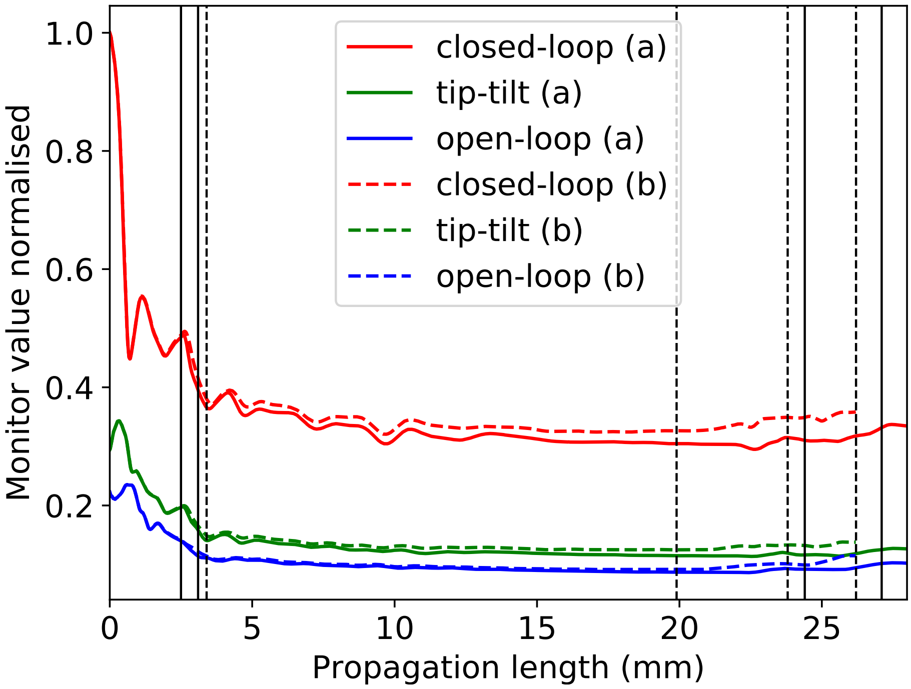

Figure 3.10: Co-added computed power enclosed inside the 36 waveguides as a function of the propagating length. Vertical solid black lines indicate the 5 transition planes of the device as it was originally built, and vertical dashed black lines represent the optimised locations of the planes. This is shown for the three AO operating modes in three different colours (constant lines for default photonic dicer (a) and dashed lines (b) for the optimised version correspondingly). Computed powers are normalised according to the maximum of each AO modes. Averaged frames of all three AO modes were used as an input. Power fluctuations are discussed in section 3.3.3.

### 3.2.3 Modal noise results

To investigate whether the theoretical PD was subject to modal noise, I performed two analyses. The first is similar to a classical modal noise experiment, where the measured barycentre of the slit moves (Rawson et al. 1980; Chen et al. 2006). To do this I chose a single wavelength and examined the stability of the near field image of the slit using `Soapy` produced images as an input. The second is a more recently discovered phenomenon, namely periodic variations of throughput as a function of wavelength, due to modal mismatch in the reformatting devices (Spaleniak et al. 2016; Cvetojevic et al. 2017).

To check the stability of the slit, the intensities of output frames from the simulations were averaged. The variation of the MFD and its barycentric position were calculated to look for disturbances of the coupled field that are translated to a different speckle pattern at the slit output. Figure 3.11 presents the analysis results of the PD. In the top panel the averaged slit image (intensity) from `BeamPROP` is illustrated. The middle panel shows the MFD of the slit profile calculated from the Gaussian fit, and the bottom panel depicts the barycentre position of the MFD calculated across the slit.

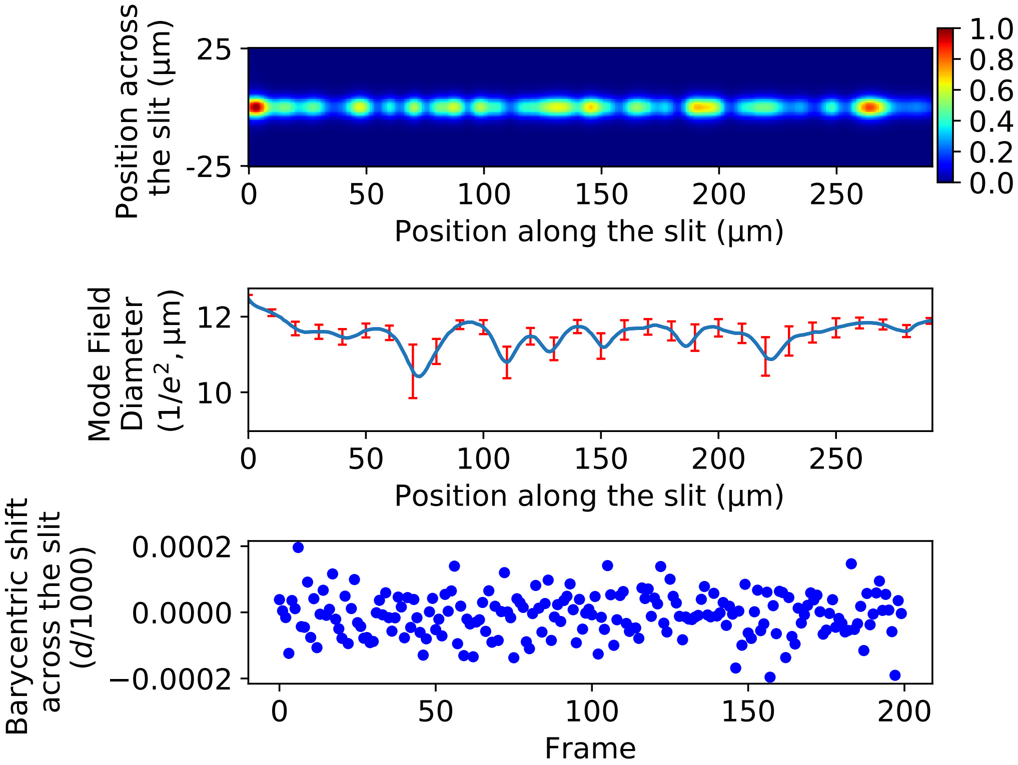

Figure 3.11: Top panel: Near field averaged image (intensity) of the slit from `BeamPROP` simulations (@1550 nm). Middle panel: MFD of the slit profile including 1$\sigma$ errors from individual frames. Bottom panel: Near field barycentre shifts across the slit.

Measurements of the barycentre movement are presented as a portion of one-thousandth of the core diameter ($d/1000$). Results show a mean variation of 1.2 µm (10% of the averaged MFD) in the MFD dimension, while the semi amplitude barycentre variation was found to be of the order of $2 \times 10^{-4}$ ($d/1000$). It should be noted that the simulations did not include any manufacturing errors in the straightness of the slit. These variations degrade the spectral resolving power and introduce noise and uncertainties in the produced spectra. Measurements of the throughput were performed in two wavelength regimes; the first covering the 1545-1555 nm wavelength range with 0.1 nm steps to approximate a typical low resolution spectrum (R ∼ 15,500), and the second covering the 1554.5-1555.5 nm wavelength range with 0.01 nm steps corresponding to a typical high resolution spectrum (R ∼155,000). It should be noted that the launch mode profile remained the same in those simulations for all wavelengths, namely a 50 µm (MFD @ $1/e^2$) representative of a diffraction-limited input injected into the entrance of the PD. Normalised throughput results are presented in Figure 3.12, where it can be seen that there is no significant variation of throughput with wavelength, both for high and low resolution simulations.

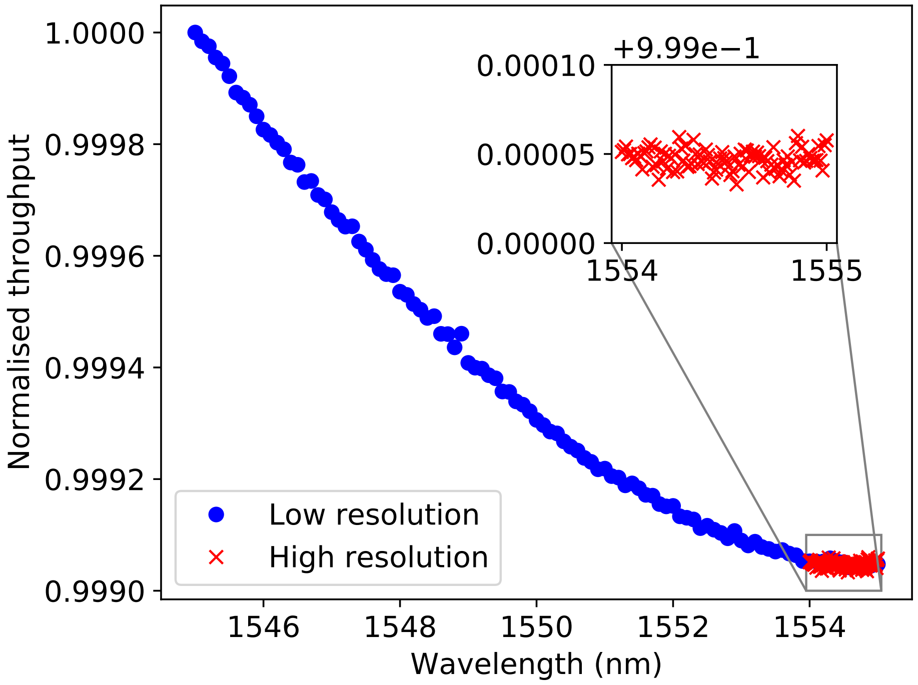

Figure 3.12: Throughput performance of the photonic dicer as a function of wavelength for low spectral resolution scanning with steps of 0.1 nm (R ∼ 15,500), and high spectral resolution scanning with steps of 0.01 nm (R ∼ 155,000). **Inset:** High spectral resolution magnified.

## 3.3 Discussion

### 3.3.1 Adaptive Optics performance

In order to match the performance for each AO operation mode, the datasets from `Soapy` were compared to the corresponding on-sky data. By comparing the EE within a growing box starting from the centre of averaged data frames as a function of square box spatial dimensions, I matched the simulated datasets to on-sky ones. I found most results converged for the same AO parameters as on-sky, though the mean seeing value of all AO modes used in `Soapy` was 1.04 arcseconds instead of the 0.7 arcseconds as seen on-sky (see Table 3.1 & Harris et al. (2015)). This might be caused by various factors, including the unstable atmospheric conditions on-sky, vibrations due to electronics in the telescope and the impact of the wind on the telescope dome and around its components. This raises the question of how best to optimise future simulations and what data to take for future on-sky tests. Future work will involve adding more noise to the simulations to try to better compare the results with on-sky data. It should be noted also that the effect of changing atmospheric conditions was considered in order to represent better the on-sky conditions (see Figure 3.10 and Table 3.1 by adjusting the seeing parameter in each AO mode).

### 3.3.2 F-ratio calibration

Harris et al. (2015) state that the relative scaling between the calibration and main arms of their experiment configuration had a magnification mismatch. This was caused by errors in focal length calculation due to the extremely short focal length $\sim 4.5$ mm lenses that imaged the PSF generated by CANARY onto the PD entrance. Our initial tests were performed with their platescale of 7.96 arcseconds/mm (a PD entrance aperture of 405 mas), which led to an underestimation of the on-sky throughput performance. Following further investigation I concluded that a platescale of 6.37 arcseconds/mm (PD entrance aperture of 321 mas) produced a much better fit of the resulting throughput compared to the on-sky results. With the appropriate corrections to magnification, I found that their results fit mine. As their lenses had short focal lengths it is likely that their scaling has large errors, which leads to the mismatch. In future on-sky experiments it would be extremely useful to have accurately characterised optical designs.

### 3.3.3 Evanescent field coupling

In Figure 3.8 I see that the measurements with lower EE (and hence less light into the PD) show a throughput closer to the input EE (a higher device transmission); while when the EE is increased, the fraction of light passing through the PD appears to drop.

To investigate this effect, a test was conducted with three data frames from Soapy, one in closed-loop mode, one in open-loop and one in tip-tilt (full field). As with my other simulations, this was propagated through the PD and the throughput measured. The field outside the PD was then set to zero and the simulation was re-run (cut field). A third simulation was then performed with the field inside the PD set to zero (cut-inside field) (see Figure 3.13 (full, cut, cut-inside field)).

To calculate the relative throughput for each simulation per AO mode, I use the following equation

$$\begin{aligned} T_{\mathrm{tot}} &= EE_{\mathrm{b}} \times T_{\mathrm{b}} + EE_{\mathrm{c}} \times T_{\mathrm{c}} \\ 20.53\% &= 42.05\% \times 46.28\% + 57.94\% \times 1.86\% \\ 9\% &= 16.06\% \times 49.07\% + 83.94\% \times 1.34\% \\ 11.95\% &= 20.4\% \times 50.12\% + 79.6\% \times 2.17\%, \end{aligned} \tag{3.2}$$

where $EE_{\mathrm{a,b,c}}$ the percentage of the light in the partial simulation ($EE_{\mathrm{a}} = EE_{\mathrm{b}} + EE_{\mathrm{c}} = 100\%$), and $T_{\mathrm{b,c}}$ the throughput in the partial simulation.

The results from this are shown in Table 3.5. This result shows that the light coupled into the PD was not coupled entirely at the entrance to the PD. This can be explained as being due to the small refractive index difference between core and cladding ($\Delta \approx 1.76 \times 10^{-3}$). This gives the PD a large evanescent field, which couples light into the waveguides.

| AO mode | Full field (Throughput) | Cut field ($EE_{\mathrm{b}} \times T_{\mathrm{b}}$) | Cut-inside field ($EE_{\mathrm{c}} \times T_{\mathrm{c}}$) |
|---|---|---|---|
| closed-loop (%) | 20.53 | 42.05 × 46.28 | 57.94 × 1.86 |
| tip-tilt (%) | 9 | 16.06 × 49.07 | 83.94 × 1.34 |
| open-loop (%) | 11.95 | 20.4 × 50.12 | 79.6× 2.17 |

Table 3.5: Evanescent field contribution results (See section 3.3.3)

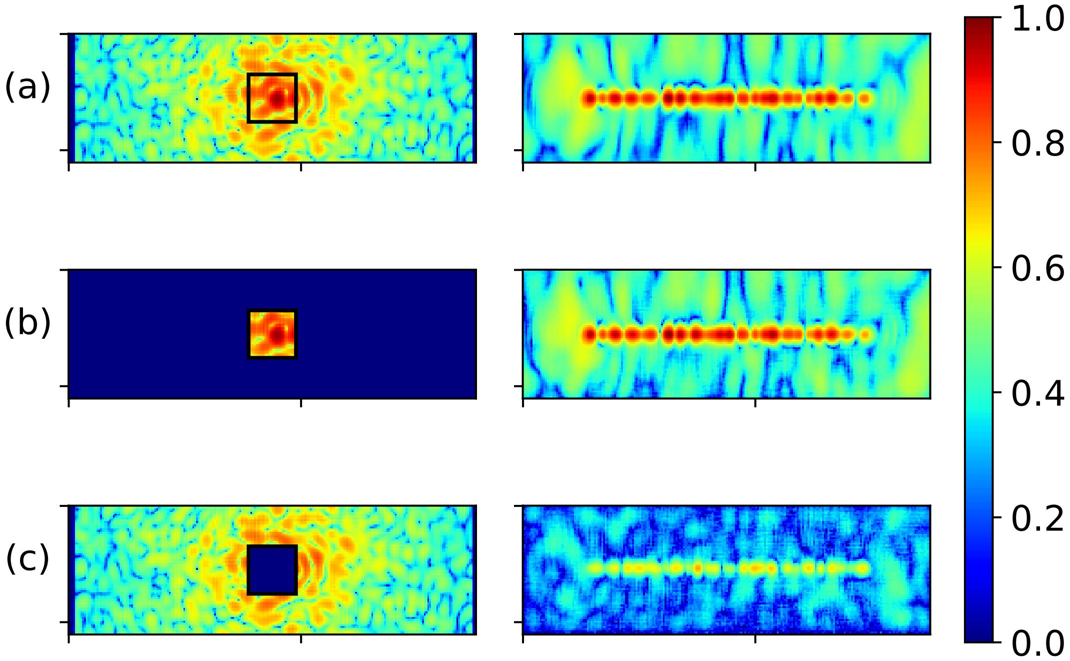

Figure 3.13: (a-c) Colour map images (logarithm of intensities) of the `Soapy` closed AO mode input data at the left together with the corresponding reformatted output of the photonic dicer at the right, for 3 different ensquared energy coupled to device spatial simulation domain, ((a) - full field) and ((b) - cut field) 42.05 % of the full frame, ((c) - cut-inside field) 57.94 % of the full frame. The simulated spatial domain for each of the 6 frames is 438×138 µm.

For looking into this further, the partial power monitors of `RSoft` were examined as the light propagated along the waveguides. Figure 3.10 shows the normalised power within the waveguides. As expected, this drops as the light propagates through the PD. However, in the second to last section the power is increasing slightly. This is due to the power monitors in `RSoft` not taking the evanescent field of the waveguides into account.

As the waveguides in the second to last section are brought together, the evanescent field from each one is coupled into the adjacent waveguide, which means the evanescent fields overlap, increasing the measured power in the PD.

To summarise, my findings indicate that up to 2% of the light within the slit output originates from evanescent field coupling. Thus, a slit mask should be used in front of the PD entrance if the evanescent field is undesired depending on the scientific goals.

### 3.3.4 Modal noise

As it can be observed from the bottom panel in Figure 3.11 the modal pattern in the slit is not straight and has some limited residual movement even though the slit was configured to be straight. This, as with modal noise, will limit the spectral resolving power of the spectrograph, though not to the same extent as with the modal noise in conventional fibres (Chen et al. 2006). In order to prove that statement two experiments were performed to justify my hypothesis. Firstly, following the procedure as described in section 3.2.3 the variation of the MFD and its barycentric position were calculated for a device identical to the PD, though at the output level of the slit the waveguides were separated and not touching each other. Secondly, the same method was applied to a common circular MMF 50 µm in diameter with a NA = 0.22 and refractive index of the core equal to 1.45. Results suggest that for the separated version of the PD, barycentric movement is 50% more stable than the original version of the PD (semi amplitude variation $10^{-4}$ ($d/1000$), see Figure 3.14), while for the MMF case the barycentre movement of the average of the speckles that were calculated, is three orders or magnitude larger than the PD (semi amplitude variation $2 \times 10^{-1}$ ($d/1000$), see Figure 3.15) and qualitatively similar to results in the literature (e.g. Feger et al. 2012).

It should be cautioned that, as noted in Spaleniak et al. (2016) any imperfections in the manufacture of the slit will result in modal noise due to movement of the barycentre of the MFD. Following the results above, it is suggested (as already pointed out in the aforementioned paper) the waveguides of the output slit to be well separated between them, to allow reduction of this modal noise.

I also did not observe variation in throughput with wavelength for the PD, as seen with similar devices and wavelength regimes (e.g. Spaleniak et al. 2016; Cvetojevic et al. 2017). This suggests the PD device is free of noise caused by modal mismatch between components (e.g. the mismatch between a MMF and PL in Cvetojevic et al. (2017)).

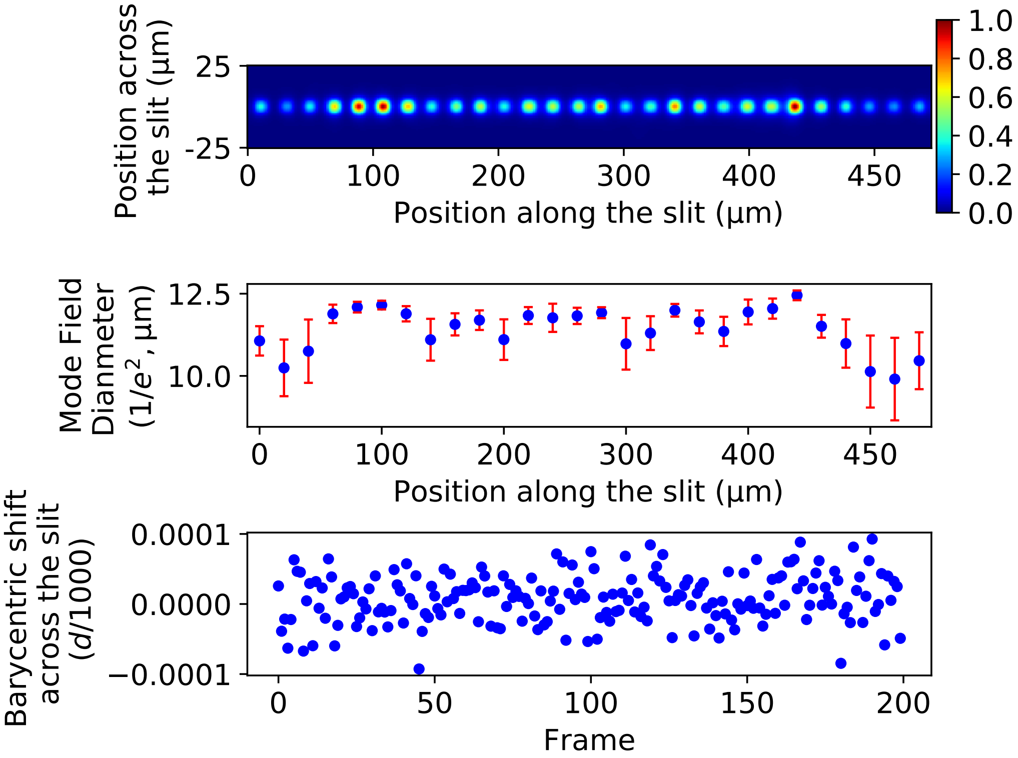

Figure 3.14: Top panel: Near field averaged image (intensity) of the separated slit from `BeamPROP` simulations. Middle panel: MFD of the slit profile including 1σ errors from individual frames. Bottom panel: Measurements of barycentre movement across the slit from individual frames.

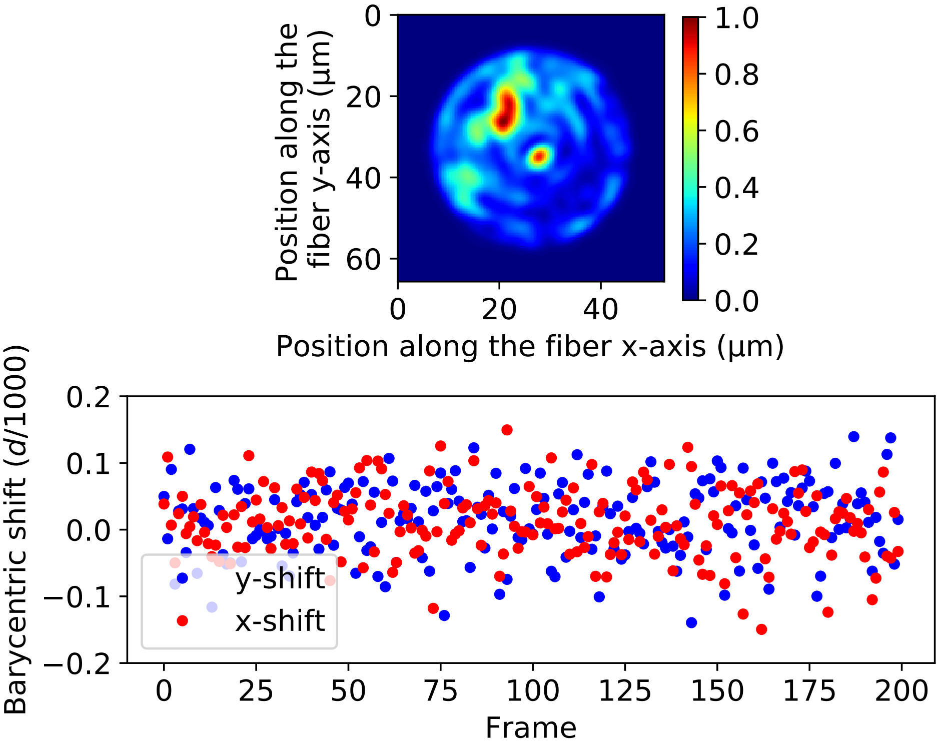

Figure 3.15: Top panel: Typical near field image of the 50 μm MMF output from `BeamPROP` simulations. Bottom panel: Measurements of barycentre movement along the fibre y-axis (blue) and x-axis (red) from individual frames.

## 3.4 Conclusions

In this chapter, a theoretical study was conducted concerning the performance of an existing astrophotonic component, the PD. Two tools were used for that: `Soapy`, a Monte Carlo AO simulation program to model the atmosphere and its impact on the performance of the device, and `BeamPROP` by `RSoft`, a finite-difference beam propagation solver to simulate the device itself. The simulated AO corrected PSFs were used as an input to the replicated PD in `RSoft`.

Results matched the on-sky results well, showing a simulated throughput of 20 ± 2% in closed-loop (compared to the same value on-sky), 9 ± 2% in tip-tilt (compared to the same value on-sky) and 8 ± 2% in open-loop (compared to 11 ± 2% for on-sky). The slight variation is likely due to changing atmospheric seeing during the course of the observations, which were only partially reproduced in the simulation.

I also investigated the effect of modal noise on the PD, results show that although it is not completely modal noise free it should show a reduction of three orders of magnitude as compared to a standard

MMF. This can also be improved by separating the output slit, as suggested in Spaleniak et al. (2016).

Further simulations were used to optimise the device and resulted in an absolute throughput improvement of 6.4%. This highlights the importance of fully simulating such devices, in particular with atmospheric effects.

Simulations also revealed an error in magnification at the input of the PD reported in Harris et al. (2015). A value of 7.96 arcseconds/mm was reported for the plate scale, while my investigation resulted in a plate scale of 6.37 arcseconds/mm. Optimising this will be important in future work for both the devices and also the AO performance.

Results suggest that detailed simulations are a valuable tool for the design of new components for astronomy with the aim of enabling more precise measurements, easier calibration of the acquired data, and more compact instruments for future telescopes. Simulations like these can be used to estimate the on-sky performance in non ideal observing conditions.

Aims for future work include further optimisation for better coupling to the telescope PSF by repositioning of the PD entrance wave-guide positions and improvement of the transmission of the device through a better manufacturing process.

Future plans for physical devices call for the development of more efficient devices through manufacturing optimisation and then integration in a complete instrument.

# Chapter 4

# Hybrid reformatter simulations and optimisation

In this chapter motivated by the method developed in the previous chapter, I present the simulated results of a more advanced astrophotonic reformatter than the PD, namely the hybrid reformatter (HR) (MacLachlan et al. 2017) and compare it with its on-sky performance. This is an astrophotonic spatial reformatter that geometrically manipulates the MM input PSF into a SM (diffraction-limited) pseudo-slit output, aiming to increase the resolving power of the spectrograph into which the light is coupled and enable more precise measurements of astronomical targets with the elimination of modal noise. The HR is composed of a 92-core MCF (91 plus an extra core to define orientation and aid alignment) tapered down to form a PL (Leon-Saval et al. 2005, 2013; Birks et al. 2015) having a MM entrance at one end face, while towards the other end the cores are uncoupled in the original hexagonal arrangement of the MCF. Following that, the cores are connected to a ULI reformatter that re-arranges the hexagonal geometry of the MCF cores into a slit profile output to feed a spectrograph.

This chapter is organised as follows: starting with Section 4.1 the configuration parameters for the simulation of the HR are reported. In Section 4.2 results are presented as well as the selected method and the optimisation techniques. Following that, a discussion of the results is included in Section 4.3, and finally the conclusion in Section 4.4.

The chapter is largely drawn from Anagnos et al. (2018b).

## 4.1 Methods

Performing precise simulations is of paramount importance for calibration of future designs as well as to estimate their performance in realistic conditions. Motivated by this, a combination of two simulation tools was used to simulate the HR. `Soapy` (Reeves 2016), a Monte Carlo AO simulation tool, was used to replicate the atmospheric conditions encountered on-sky and the influence on the device's performance. I combined this with `BeamPROP` by `RSoft` (Synopsys 2018), for simulating the propagating field through the medium using a finite-difference beam propagation solver.

The configuration of the simulation was the following: first, `Soapy` was used to generate the image of an AO-corrected star, and then the frames were used as an input for the `BeamPROP` simulations. In the next stage, a Monte Carlo simulation routine was built into `BeamPROP` for improving the performance of the device by calculating the relative losses at its separate propagation planes.

### 4.1.1 `Soapy` set-up

The HR was tested on-sky with CANARY AO system (Myers et al. 2008) at the William Herschel Telescope. Therefore, `Soapy` was configured to approximate the sky conditions during the observation run (see Table 4.1). `Soapy` was used to simulate three different AO operation modes as they were performed on-sky with CANARY, namely closed-loop, open-loop and tip-tilt correction only. In closed-loop mode of AO operation CANARY provided correction at an update rate of 150 Hz, both for tip-tilt and higher order aberrations, while for the tip-tilt AO mode of operation the integrator loop gain on the high-order modes was reduced to a small value on the order of 0.001, thus correcting only for the PSF position in real-time, but not for the PSF shape which required higher-order AO correction. As for the case of open-loop mode of correction, the gain on the tip-tilt correction was further reduced in order to have the PSF positioned in the reference location providing optimum coupling, but without having high frequency correction. A value of 0.15 m for the seeing parameter (Fried parameter-$r_0$) was selected, representative of the on-sky conditions (MacLachlan et al. 2017).

`Soapy` was configured to produce 200 NIR data frames, each with a 6 ms exposure duration, to be later used as an input to `BeamPROP`. Each `Soapy` frame covers a 3.0 arcseconds squared field on-sky, slightly more than three times the angular size of the HR entrance aperture. In contrast to the data

| | Modes of AO operation | | |
|---|---|---|---|
| | closed-loop | open-loop | tip-tilt |
| Parameters | | | |
| Seeing (arcsec) | 0.69 | 0.69 | 0.69 |
| Instantaneous Strehl ratio (mean) | 0.53 | 0.21 | 0.11 |
| Long exposure Strehl ratio (mean) | 0.38 | 0.04 | 0.06 |
| Fried parameter $r_0$ (m) (@1550 nm) | 0.15 | 0.15 | 0.15 |
| Atmosphere layers | 5 | 5 | 5 |
| DM integrator loop gain tip-tilt | 0.3 | 0.001 | 0.3 |
| DM integrator loop gain Piezo | 0.3 | 0.001 | 0.001 |

Table 4.1: `Soapy` input parameters for simulation

acquired on-sky, the `Soapy` frames provided both phase and amplitude information, which proved to be crucial for the simulation results (see Section 4.2.1).

### 4.1.2 `BeamPROP` set-up

In the next stage, the frames from `Soapy` simulation were used as an input to `BeamPROP` simulations; the HR's angular size was set to 1.1 mas in the simulation domain. The design structure of the device was as described in MacLachlan et al. (2017). The HR is composed of a PL section followed by a ULI reformatter section, ending in a slit profile output. To perform the simulations in `BeamPROP`, the refractive index information is a crucial parameter, both for the core and the cladding materials. For the HR the initial PL section of MCF was made of fused silica with step-index Ge-doped cores fabricated as in Birks et al. (2012); Birks et al. (2015), and for the following reformatter section a substrate of borosilicate glass (SCHOTT AF45) was used (Meany et al. 2014) for the inscription of the waveguides with a $n_{\mathrm{cl}}$ ~1.4974 at 1550 nm. As the are no refractive index measurements of the waveguide profiles for the device, the value from (Thomson et al. 2011) was used ($\mathit{\Delta} = \frac{n_{\mathrm{core}} - n_{\mathrm{clad}}}{n_{\mathrm{core}}} \approx 1.76 \times 10^{-3}$) as it is considered to be close to the device, despite the small expected differences resulting from the inscription parameters (see Table 4.2) and the difference in glass. The 3D structure of the ULI section of the HR as shown in `RSoft`'s CAD, is illustrated in Figure 4.1.

In general, in the `BeamPROP` simulation tool the material propagation loss is a freely chosen parameter depending on the material and its properties. Therefore, in order to add greater precision in my simulations I ran tests using a propagation loss of 0.1 dB/cm (Nasu et al. 2005). This value is an

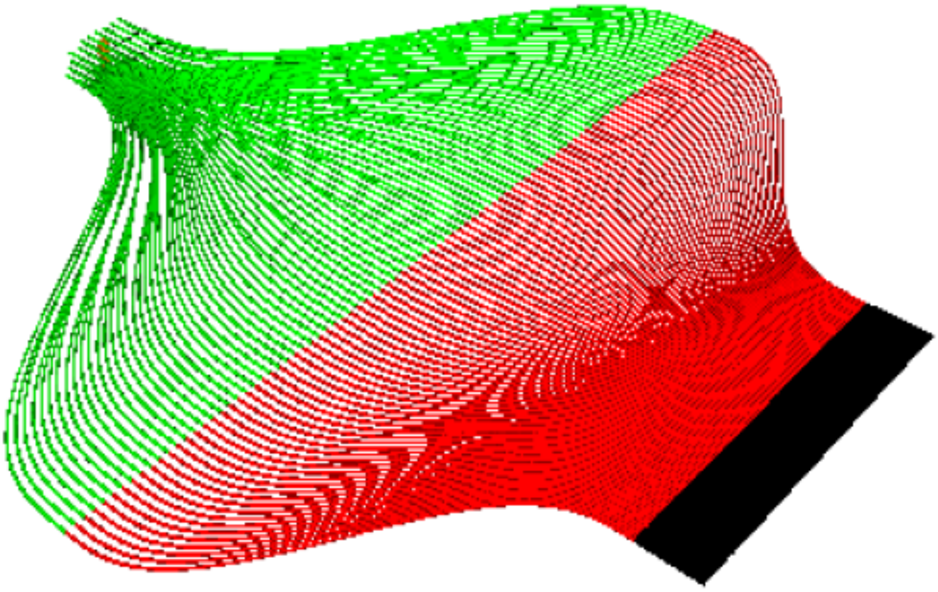

Figure 4.1: The Hybrid Reformatter's 3D structure, without the initial photonic lantern section included in the plot as visualised in the `RSoft`'s CAD environment. The colours show the 3 different transition planes used.

optimistic estimate representing relatively low losses when compared to the losses due to the geometric design ($< 2$ % over the HR length). Further tests will be performed in future modelling with optimised devices.

| Parameters | Thomson et al. | hybrid reformatter |
|---|---|---|
| $n_{\mathrm{cl}}$ (@1550 nm) | $\sim 1.49$ | $\sim 1.4974$ |
| Pulse Energy (nJ) | 165 | 174 |
| Pulse repetition rate (kHz) | 500 | 500 |
| Pulse duration (fs) | 350 (1047 nm) | 430 (1030 nm) |

Table 4.2: Comparison of ULI inscription parameters used in Thomson et al. (2011) and MacLachlan et al. (2017).

### 4.1.3 Throughput measurement

In order to calculate the total throughput ($T_{\mathrm{tot}}$) that includes the coupling losses and transmission properties of the device from simulations, the ratio of the total intensity in the output slit to the injected beam intensity was considered as follows

$$T_{\mathrm{tot}} = \frac{F_{\mathrm{out}}(i)}{F_{\mathrm{in}}(i)}, \quad i = \#frames, \tag{4.1}$$

where $F_{\mathrm{out}}$ is the output of the slit and $F_{\mathrm{in}}$ is the coupled flux of the input field.

## 4.2 Simulation results

### 4.2.1 Output power performance results

In this section are the simulation results from the above explained procedure. `BeamPROP` simulations were performed using `Soapy` output data that provided both amplitude and phase information. As the on-sky frames obtained with CANARY were obtained by an InGaAs detector that records the intensity information of the sampled light, these were not used with `BeamPROP`. This is due to the lack of phase information, which yields incorrect results (see Anagnos et al. 2018a).

In Figure 4.2 the simulation results of 200 frames with `Soapy` are presented. The throughput of the HR for closed-loop AO operation was measured to be 56±4(%). In tip-tilt operation mode the output was measured to be 55±5(%); and for open-loop correction results were 51±7(%). To further investigate the HR's coupling performance, the ensquared energy (EE) ratio between the closed-loop and tip-tilt AO modes of correction was calculated and plotted as a function of the device's MM entrance input size for the `Soapy` averaged data. The results are presented in Figure 4.3 where they show that the spatial size of the MM entrance of the device is larger than the spatial size of the input. Hence, all the light is coupled into the HR for both AO correction modes because of its large collecting area.

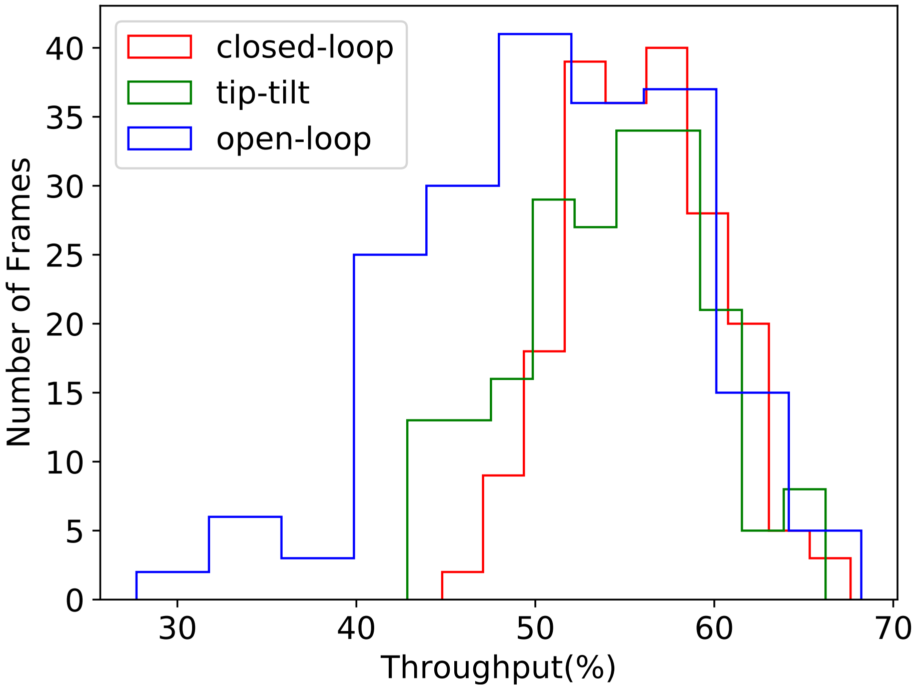

Figure 4.2: Histogram distribution of throughput measurements from simulations shown for three different AO modes. Red colour represents the closed-loop AO mode of correction, green shows the tip-tilt correction and blue shows open-loop correction.

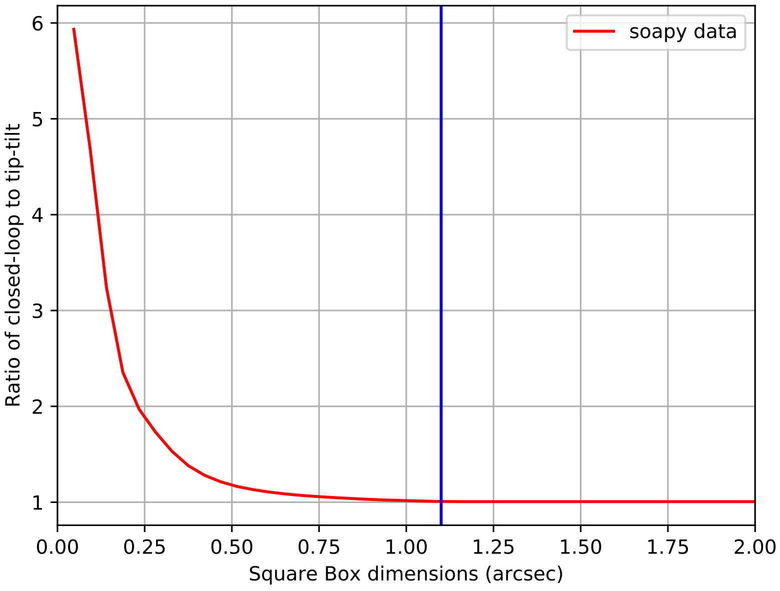

Figure 4.3: The distribution of closed-loop and tip-tilt AO mode ensquared energy ratios as a function of the entrance's spatial scale (circular radius centred), plotted for simulated (`Soapy`) averaged (Intensity) data. The vertical blue line represents the circular entrance size of the PL section of the HR.

### 4.2.2 Optimisation results

When the HR was designed and manufactured in 2014 there was no attempt to fully model it. Therefore, there are many areas for further optimisation of the device's performance. To assess this, a Monte Carlo simulation run was performed to investigate the optimal length of each transition stage separately of the ULI section of the device (see Figure 4.1).

A gradual-adiabatic transition of the ULI waveguides position in between the three different planes is a crucial factor to ensure low loss of propagated light (Birks et al. 2015). Accounting for that, there is a trade off between material and bend losses against the device's length, when making use of the ULI technique to inscribe waveguides in materials, considering that the waveguides profiles are uniform and similar to each other.

In order to optimise further the throughput performance of the HR, a Gaussian input (close to the diffraction limit) with a 25 µm mode field diameter (MFD) generated by `RSoft` was chosen. Injecting this input, I performed a short Monte Carlo simulation on the HR, in order to optimise each of its reformatter section transition planes for transmission by scanning for a variety of different lengths between the 3 transition planes of the reformatter section. Preliminary results show an improvement in theoretical transmission by 2% (a relative $\sim$ 6% improvement in performance), leading to a shorter, more compact device. However, transition planes can be further improved to be lower in loss (more adiabatic).

### 4.2.3 Modal noise results

To investigate the modal noise properties of the modelled HR device, I followed a similar procedure to that described by Anagnos et al. (2018a). The wavelength of operation throughout all the simulations was 1550 nm. To assess the modal noise levels of the optical device, the barycentric movement of the slit output was measured (Rawson et al. 1980; Chen et al. 2006) examining its stability in the near field regime.

The dimension of the MFD and its barycentric movements were measured, from the simulation results. In addition to that, I examined disturbances of the injected field to the device, which lead to different speckle distribution at the reformatter's slit output. Results of this analysis are presented in

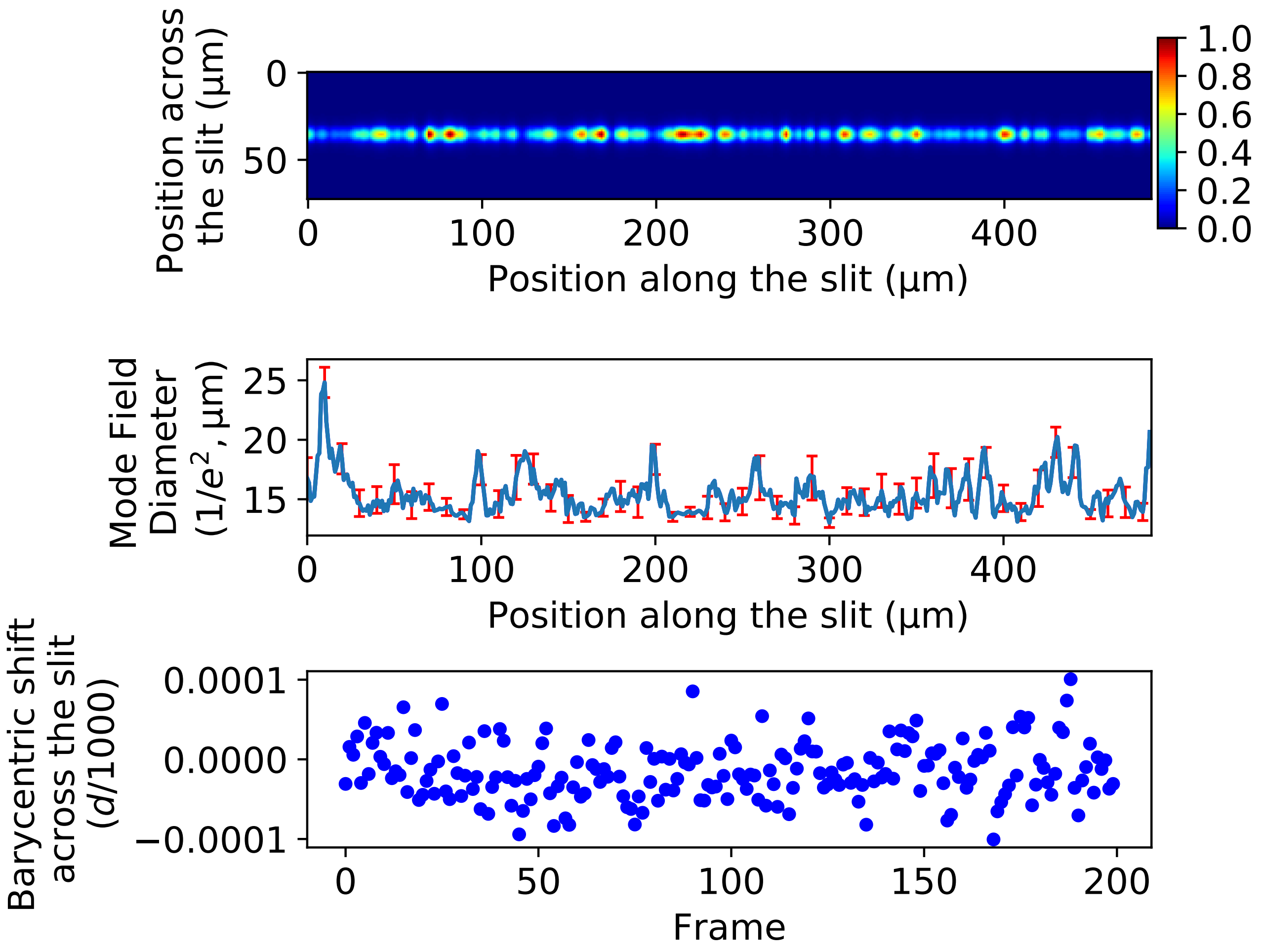

Figure 4.4: Top: Averaged (intensity) near-field images of the slit output from `BeamPROP` simulations (@1550 nm). Middle: MFD profile size measurements of the slit with $1\sigma$ errors from the individual images. Bottom: Barycentric variations across the slit of the device calculated from the dataset.

Figure 4.4, where the averaged slit images are illustrated on the top panel, the middle panel figures the calculated MFD size from the Gaussian distributions fitting along the slit, and finally the barycentric movement of the MFD across the slit is plotted in the bottom panel of the figure. The results of the barycentric movement of the slit are expressed in units of one-thousandth of the waveguide's core diameter size ($d/1000$). It is immediately apparent from the figure that the average semi-amplitude variation of the barycenter is on the order of $10^{-4}$ ($d/1000$), which is small enough and meets the expectations for the modal noise properties of this device compared to other devices (Anagnos et al. 2018a), as is discussed further in section 4.3.3. It must be noted that the above mentioned simulation results neglect the effect of manufacturing errors in the straightness of the slit. As expected, the presence of such variations limits the spectral resolving power of a spectrograph by causing noise and uncertainties in the measured spectra.

## 4.3 Discussion

### 4.3.1 Throughput performance

Following the procedure as described in section 4.1 for the simulations, I obtained a difference in throughput between the simulations and the on-sky output performance of the order of 3 to 8 percent (see Table 4.3). These small differences in throughput are mostly caused by the following factors: firstly the on-sky AO raw data during the night of observation were not available at this point, therefore the AO performance per mode of correction could not be matched with sufficient precision; secondly the changing on-sky atmosphere conditions during the observation run were not considered for the `Soapy` simulations, and lastly it was assumed that the waveguide's structure and geometry in simulations was free of manufacturing errors.

| Data and results | | |
|---|---|---|
| AO mode | On-sky | `Soapy` + `BeamPROP` |
| closed-loop (%) | 53 ± 4 | 56 ± 4 |
| tip-tilt (%) | 47 ± 5 | 55 ± 5 |
| open-loop (%) | 48 ± 5 | 51 ± 7 |

Table 4.3: Percentage results of throughput from simulations in comparison with the on-sky conditions.

### 4.3.2 Coupling of evanescent field

The evanescent field coupling into the optical device is an undesirable result for various reasons, such as the appearance of modal noise due to the interaction of cladding modes with the propagated ones, or the loss of the sampled spatial information (Anagnos et al. 2018a). The HR optical device was a combination of two optical devices; a PL section made out of a tapered MCF was feeding the photonic reformatter created using the ULI technique resulting in a linear output array of waveguides. As a consequence of the higher refractive index difference of the fiber-made PL that is able to guide light confined into its cores compared to the lower refractive index contrast of the ULI device, the evanescent field coupling issue was absent.

### 4.3.3 Modal noise

As mentioned above, the presence of modal noise in spectroscopic measurements diminishes further the theoretical resolving power of the instrument producing additional noise in the measurements. It is apparent from the bottom part of Figure 4.4 that there is a minor barycentric movement of the slit output even though the slit is designed to be completely straight. To address the magnitude of this barycentric movement the following experiment was performed; the same method to the one described in section 4.2.3 was applied to a typical state-of-the-art MMF with an octagonal cross-section profile of 50 µm in diameter and another typical SMF of 8.2 µm in diameter, similar to the Corning SMF-28 fiber. As the results illustrate, the HR modal noise properties are similar to the SMF, while their corresponding barycentric movements are three orders of magnitude less than the MMF with the octagonal cross-section (see Figure 4.5). The results are quantitatively complimentary to the related results in the literature (i.e. Feger et al. 2012).

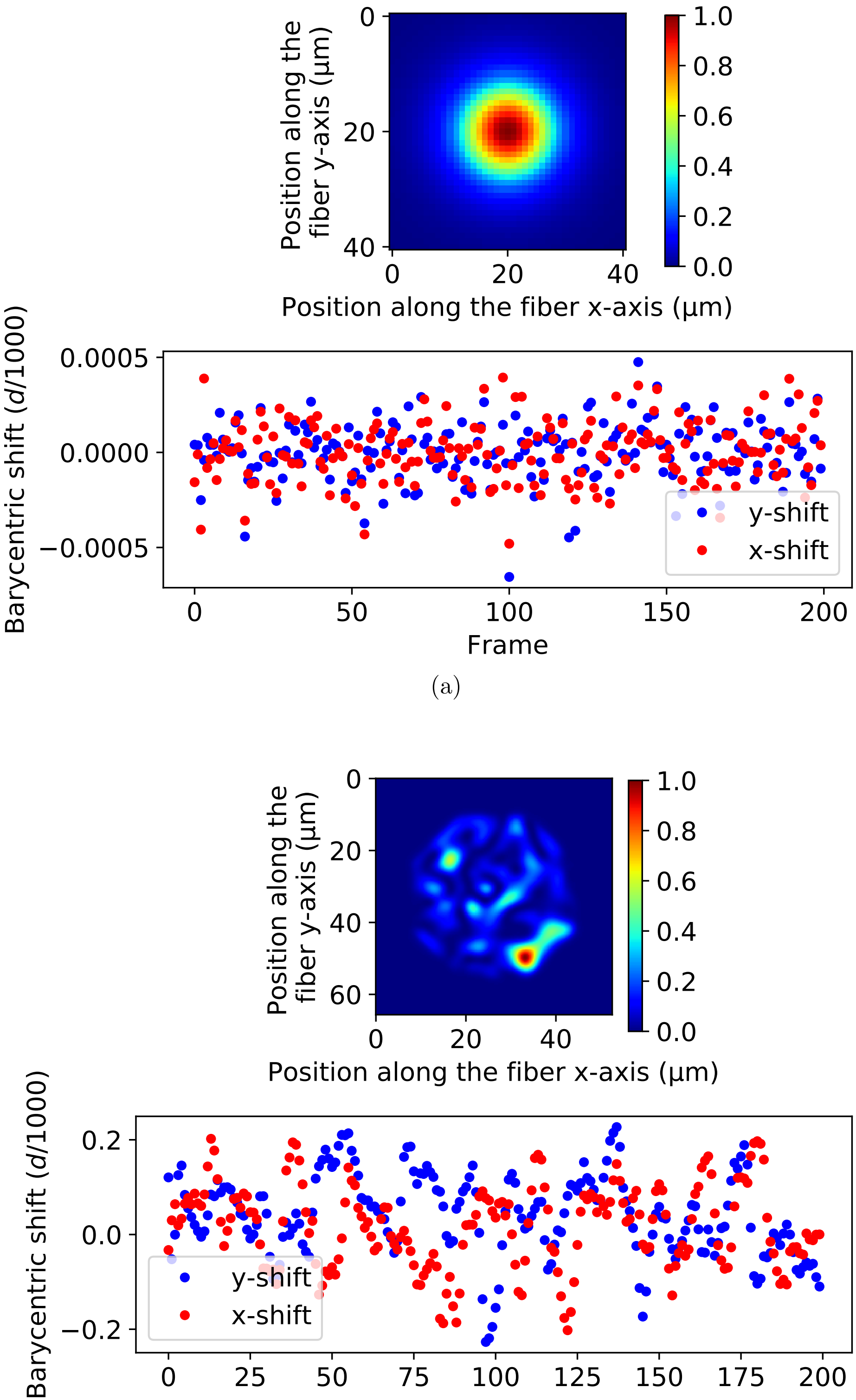

(a)

(b)

Figure 4.5: **(a)**: Top panel: Typical near-field image (intensity) of the 8.2 µm single-mode fiber output from `BeamPROP` simulations. Bottom panel: Barycentric movement measurements along the fiber x-axis (red) and y-axis (blue) derived from individual images. **(b)**: Top panel: Common near-field image (intensity) of the 50 µm octagonal fiber output from `BeamPROP` simulations. Bottom panel: Barycentric movement measurements along the fiber x-axis (red) and y-axis (blue) derived from individual images.

## 4.4 Conclusions

This chapter discussed a simulation experiment regarding the performance of an existing astrophotonic spatial reformatter, the hybrid reformatter. To this end, I used two tools in conjunction: `Soapy` (Reeves 2016) which is a simulation program to replicate the on-sky conditions and its influence on the device's performance, and `BeamPROP` by `RSoft` (Synopsys 2018) which is a commercial finite-difference beam propagation solver to model the light propagation throughout the device using data produced by `Soapy`.

The simulation results were similar to the on-sky reported values, yielding a device performance of $56 \pm 4\%$ in closed-loop (compared to $53 \pm 4\%$ for on-sky), $55 \pm 5\%$ in tip-tilt (compared to $47 \pm 5\%$ for on-sky) and $51 \pm 7\%$ in open-loop (compared to $48 \pm 5\%$ for on-sky). The variable atmospheric seeing conditions encountered on-sky during the night of observations, which were not taken into account in this simulation, explain these differences in throughput.

Furthermore, the modal noise properties of the hybrid reformatter were investigated. Results show that although the modal noise is not entirely absent, it is improved by three orders of magnitude compared to a typical multi-mode fiber with an octagonal cross-section.

Additional simulations were performed to optimise the device's transmission performance, resulting in an absolute 2% improvement in theoretical transmission (a corresponding relative $\sim 6\%$ improvement in performance) over the model of the original device. Simulating the performance of components including atmospheric effects proves to be crucial for improving their characteristics.

The method used as well as its outcome, shows that performing similar simulations to enhance the designs of future astronomical components is essential, increasing their measurement precision while allowing for a better calibration and minimising their size footprint.

# Chapter 5

# Broadband characterisation of astrophotonic spatial reformatters in the visible spectral band

In this chapter motivated by the simulations on the previous chapters and aiming to connect them with actual laboratory measurements I present a study on the throughput performance characterisation of multiple astrophotonic reformatters in the visible band. The reformatters are inscribed using the ULI technique in two identical optical substrates using two values for the laser pulse energy, and a variety of internal geometry architectures. These were originally designed, fabricated and polished by Dr. Alexander Arriola during his research work at Prof. Michael Withford's group supported by an ARC Discovery Project funding at Macquarie University in Sydney, Australia. This study aims to explore whether the chips are an efficient way of transporting starlight at visible wavelengths from a telescope to a remotely located spectrograph. This is the first time the performance of such astrophotonic components is assessed in the visible bands, as previous attempts were accomplished only at NIR wavelengths (1550 nm) were the throughput performance is significantly better and the inscription parameters were previously explored (e.g. Davis et al. 1996; Glezer et al. 1996; Thomson et al. 2009).

## 5.1 Methods

To efficiently inject light into an astrophotonic reformatter manufactured with the ULI technique the following elements were combined: the optical substrate for the inscription of the structures, a stable ULI system to write the optical components and the fiber. For these test, the fiber was re-imaged onto the surface of the chip, however eventually it will be butt-coupled to the integrated chip at a later stage to transfer the light from the telescope's focal point to the instrument for measurements. In this section these elements will be discussed in detail.

### 5.1.1 Setup architecture

To transfer the starlight from the telescope to a diffraction-limited spectrograph, a low light-loss fiber and an integrated astrophotonic reformatter are combined. To efficiently couple the devices, their spatial modes are chosen to match closely across the operating bandwidth 600-800 nm (Birks et al. 2012). An SMF-28 by Corning was used as a fiber to transfer the light from the telescope to the astrophotonic reformatter, acting as few-mode fiber in the operation wavelength regime delivering 9 and 6 spatial field modes at 600 and 800 nm respectively (neglecting polarisation). This was confirmed by simulations using the `FemSIM` mode solving module of `RSoft` (Synopsys 2018) software. Whilst in these tests the SMF-28 was re-imaged, once determined the best setup it will be connected with the best performing reformatter, while the output slit of the reformatter will feed light into a spectrograph (see Figure 5.1).

### 5.1.2 Inscribed devices architecture

To investigate the parameters for the best performing astrophotonic reformatter, two glass substrates of the same material were inscribed using the ULI technique (Thomson et al. 2009). In these substrates, 24 different geometric combinations were inscribed in order to select the best performing one.

On the first substrate, chip#1, an inscription power of 35 nJ was used, while for chip#2 the power was 40 nJ. Inside both chips, there are three transition planes where the waveguides are routed (see Figures 5.2 and 5.11); on the first transition plane is the MM section, composed of 6 individual SM waveguides placed in a pentagon formation close together as it is the most efficient geometry to optimise the light

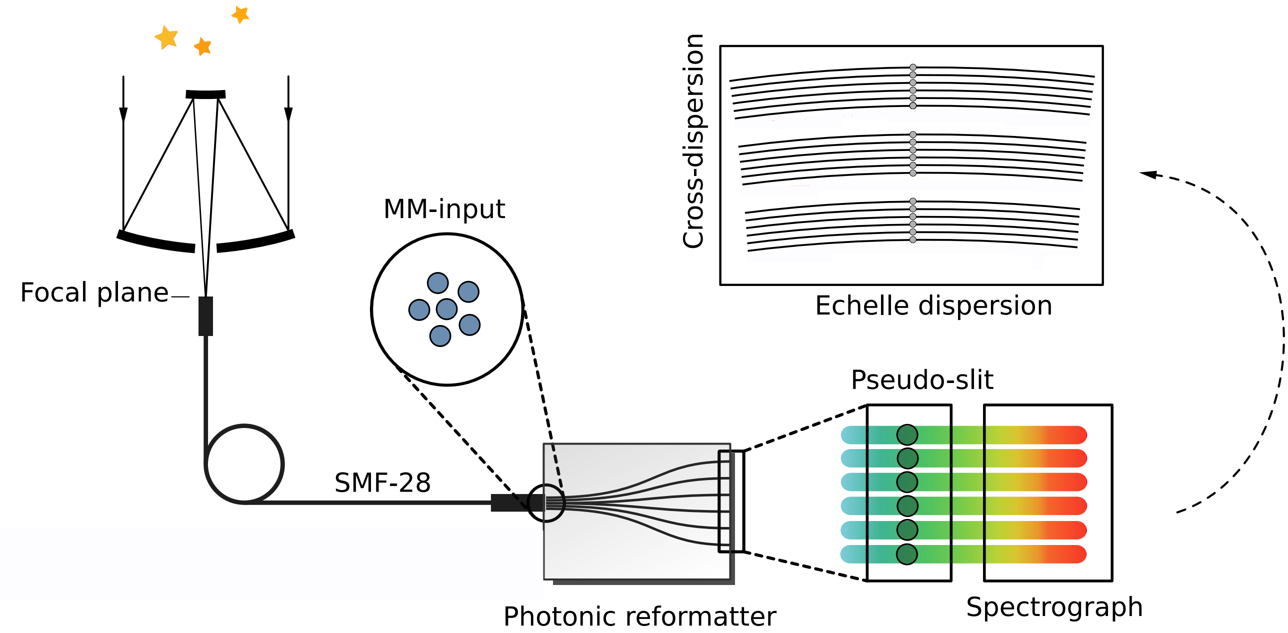

Figure 5.1: Instrument schematic concept composed of an SMF-28, the astrophotonic reformatter and the spectrograph. Image adapted from Tobias Feger.

coupling (Fontaine et al. 2012) in a straight line of a length of 3 mm along the propagation axis. On the second transition plane the individual waveguides separate from each other towards a 20 µm pitch for the chip#1 and 30 µm for the chip#2 maintaining their pentagon configuration for another 8 mm. On the third transition plane the waveguides reshape to a linear pseudo-slit array over a length of 13 mm and finally on the fourth transition plane the maintain the same configuration for another 3 mm. The total length of both of the chips is 27 mm.

The integral configuration for these 24 astrophotonic devices for the substrates includes a variation of input to output waveguide-to-waveguide pitch, a variation of the length of the last transition plane and a variable on-axis side step of the output plane to eliminate the coupling of evanescent fields. In more detail, (see Table 5.1) the first photonic device is a straight MM device composed of 6 individual SM waveguides with a 5 µm pitch separation to each other. Following that, there is a combination of 4 astrophotonic reformatters with varying pitches at the entrance waveguides and at the exit pseudo-slit (4-6, 4-7, 5-6 and 5-7 µm for the entrance-exit pitch), and right after another 4 with a varying transition length ($\Delta$y = 1-4 mm) of the last plane (the plane where the waveguides are all close to each other and in linear formation) where the third transition plane is changing as well making a combination of both planes lengths of 15+1, 14+2, 13+3 and 12+4 mm respectively. After that, there are 3 more devices with an off-axis lateral step ($\Delta$x) of 2, 3 and 4 mm respectively.

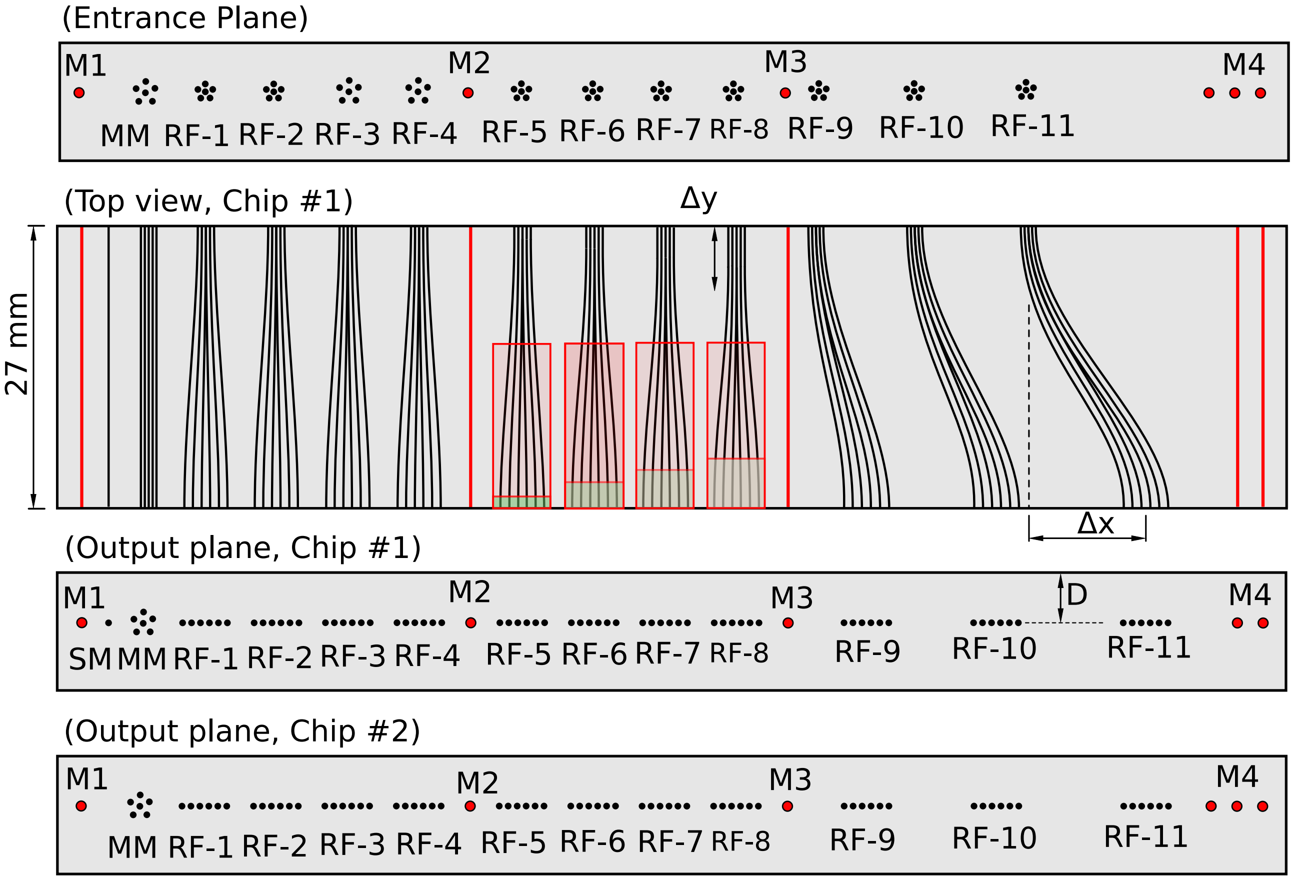
(Entrance Plane)
M1
M2
M3
M4
MM
RF-1
RF-2
RF-3
RF-4
RF-5
RF-6
RF-7
RF-8
RF-9
RF-10
RF-11
(Top view, Chip #1)
Δy
27 mm
Δx
(Output plane, Chip #1)
M1
M2
M3
M4
D
SM
MM
RF-1
RF-2
RF-3
RF-4
RF-5
RF-6
RF-7
RF-8
RF-9
RF-10
RF-11
(Output plane, Chip #2)
M1
M2
M3
M4
MM
RF-1
RF-2
RF-3
RF-4
RF-5
RF-6
RF-7
RF-8
RF-9
RF-10
RF-11

Figure 5.2: Laser inscribed astrophotonic components layout inside the two optical chip substrates. M1-4 represent the position reference marks, MM is the linear compilation of the SM waveguides in a pentagon formation, RF1-4 are the photonic reformatters with a combination of different pitch in input and output plane of their individual waveguides, RF5-8 stand for the photonic reformatters with a different length in transition final plane (Δy) towards the slit output and RF9-11 stand for the devices with a lateral displacement step from their on-axis entrance plane (Δx). All the components are inscribed at a depth of D = 200 μm (internal configuration parameters of the devices are listed in Table 5.1.)

| **Component** | **Entrance MM pitch (μm)** | **Exit slit pitch (μm)** | **Δx (mm)** | **Δy (mm)** |
|---|---|---|---|---|
| **MM** | 5 | 5 | - | - |
| **RF-1** | 4 | 6 | - | - |
| **RF-2** | 4 | 7 | - | - |
| **RF-3** | 5 | 6 | - | - |
| **RF-4** | 5 | 7 | - | - |
| **RF-5** | 4 | 6 | - | 1 |
| **RF-6** | 4 | 6 | - | 2 |
| **RF-7** | 4 | 6 | - | 3 |
| **RF-8** | 4 | 6 | - | 4 |
| **RF-9** | 4 | 6 | 2 | - |
| **RF-10** | 4 | 6 | 3 | - |
| **RF-11** | 4 | 6 | 4 | - |

Table 5.1: Internal configuration parameters for both of the optical chips. See figure 5.2 for a visual representation.

### 5.1.3 Fabrication process

For a stable and reliable inscription technique of the integrated astrophotonic devices the rather novel direct laser inscription method was selected that modify locally the refractive index of the substrate material in the 3D space.

The structures of the photonic reformatters were inscribed using the multiscan technique (Nasu et al. 2005) into a 27 mm long boro-aluminosilicate glass substrate (Corning Eagle2000). The inscription was performed using an ultrafast Ti:sapphire oscillator (FEMTOSOURCE XL 500, Femtolasers GmbH) emitting $< 50$ fs pulses at a central wavelength of 800 nm with a 5.1 MHz repetition rate. An 100x oil immersion objective lens Zeiss N-Achroplan of NA $= 1.25$ and 450 µm of working distance was used to focus the laser beam into the sample, while an Aerotech 3-axis air-bearing translation stage was used to position the sample under inscription for a smooth translation speed and waveguides inscribed with consistency.

The two glass substrates were inscribed with identical written structures using two pulse energies, 35 nJ (chip#1) and 40 nJ (chip#2) at a translation speed of 500 mm/minute based on previous studies results (Jovanovic et al. 2012; Spaleniak et al. 2013), creating waveguides which are SM at the desired operational wavelength regime. Both substrates were thermally annealed (Arriola et al. 2013) to improve the bend loss of the waveguides and marked with traces (M1-M4) for future reference. In the next stage the inscribed samples were ground and polished in order to improve the coupling at the entrance/exit waveguide's planes. Due to the high repetition rates to inscribe the structures, all waveguides were manufactured in the cumulative heating regime (Eaton et al. 2005). A microscope image of the inscribed optical chip#2 is shown in Figure 5.3 where the first five devices are visible at their input and output plane.

### 5.1.4 Throughput measurement setup

To quantify the throughput performance of each of the inscribed devices, a test experiment was constructed. The experiment apparatus involves two broadband light sources across the operation wavelength regime and a variate combination of optical lenses sets to alternate the NA of the injected beam in order to find the optimum one. The graphical layout of the setup is presented in Figure 5.4. As light sources for exploration of the devices behaviour in a broad wavelength coverage two LEDs

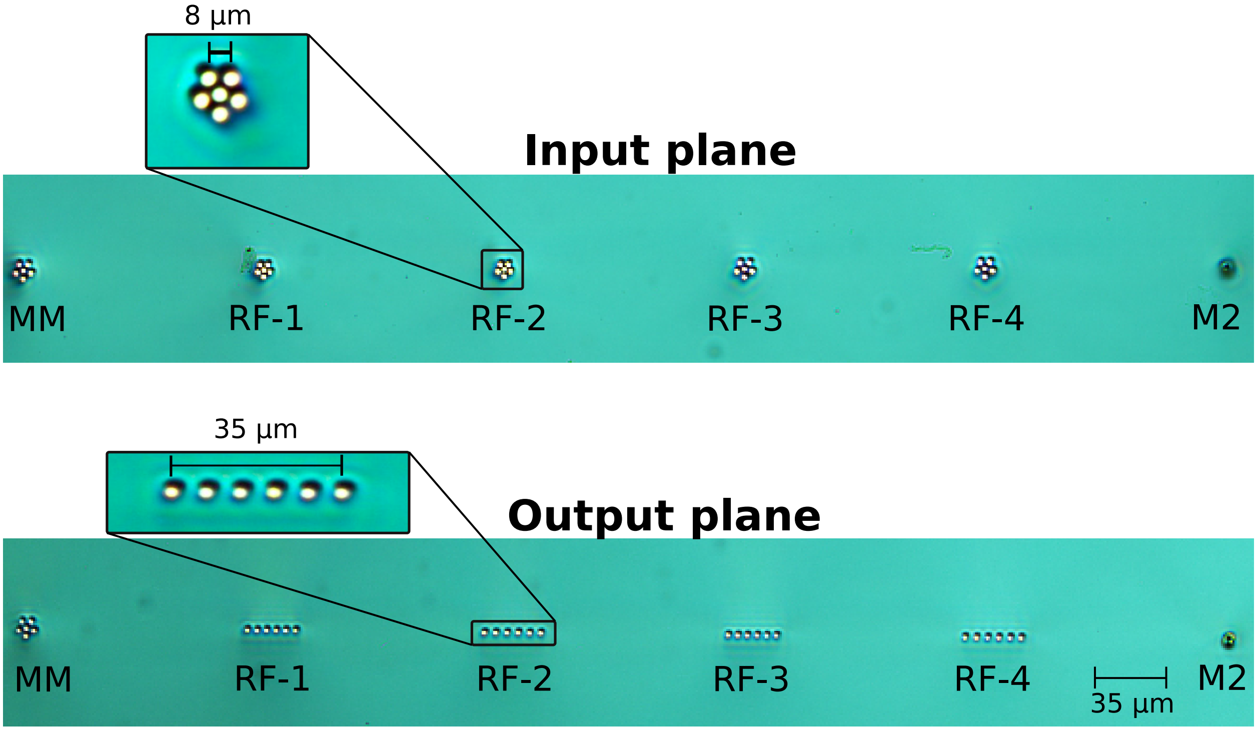

Figure 5.3: Microscope image of the input-output plane of the inscribed substrates (Eagle2000 glass) featuring five inscribed devices fabricated and characterised. In this chip#2 the individual SM waveguides were written with 40 nJ pulse energy with a translation speed of 500 mm/minute.

were used; a 600 nm (Thorlabs, LED600L) and a 800 nm (Thorlabs, LED800L) central wavelength LED with spectral FWHM bandwidths of 12 and 30 nm respectively. The light is coupled to the SMF-28 and its output is collimated using an off-axis parabola of 15 mm focal length (Thorlabs-RC04APC-P01) followed by a set of optical lenses to focus down the collimated beam (see Figure 5.5) and alter its NA (for a detailed list of them see Table 5.2). By using different combinations of focal length lenses, the spatial frequencies of the injected light are kept constant while the injected NA changes, avoiding the appearance of the Gibbs phenomenon (Gottlieb & Shu 1997). Following this, the optical chip under characterisation is placed on a 5-axis stage (Thorlabs, MBT402D-MMBT501) to position the injected beam focus at the entrance of each optical component. Following this, 19 and 50 mm achromat optical lenses were used to re-image the output of each of the chips onto the CMOS detector (ASI-290MM mono) with a sufficient beam magnification to achieve a 2.7 pixels per FWHM sampling. The last re-imaging setup with the detector was mounted on a 3-axis stage for translation.

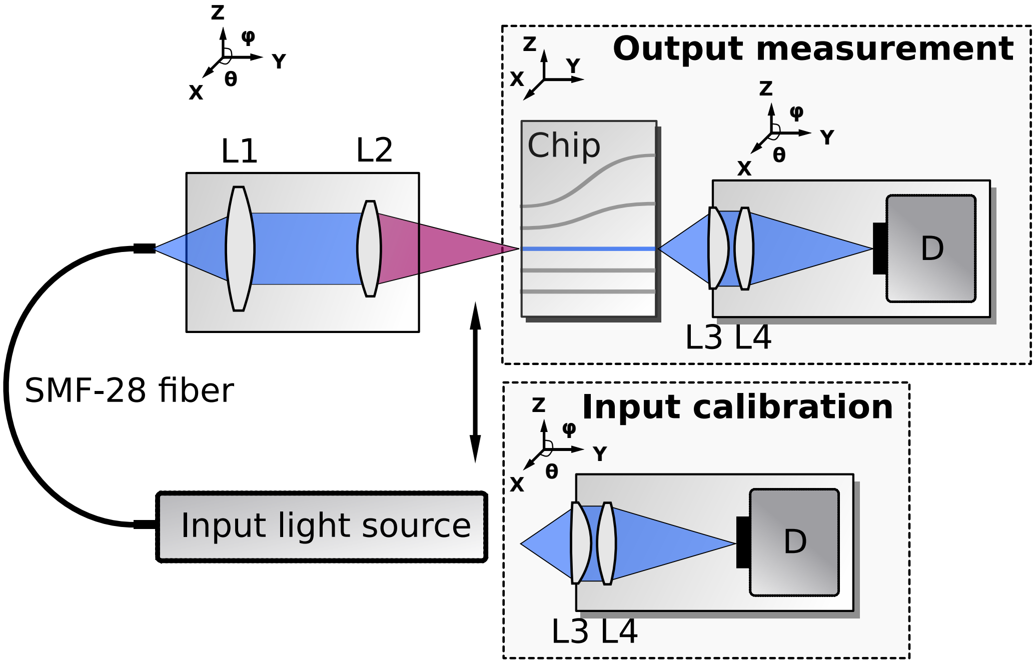

Figure 5.4: Schematic illustration of the throughput test apparatus for the optical chip substrates. An SMF-28 fiber was used to transfer light from the light source to the optical chip. A combination of a variety of focal length lenses (L2) were used with the collimation lens (L1) to modify the injected focal ratio into the sample entrance. A system of L3-L4 lenses were used to focus the output beam into the detector chip (D). This was used to calibrate the output of the chips with the injected beam. The detailed optical components that were used are listed in Table 5.2. The optical chips were mounted on a 5-axis stage and the lens system with the detector on a separate 3-axis stage.

| **Component** | **Thorlabs Part No** | **Focal length (mm)** |
|---|---|---|
| **Input light source** | LED600L<br>LED800L | -<br>- |
| **L1** | RC04APC-P01 | 15 |
| **L2** | AC254-019-B-ML<br>AC254-025-B-ML<br>AC254-030-B-ML<br>AC254-035-B-ML<br>AC254-050-B-ML | 19<br>25<br>30<br>35<br>50 |
| **L3**<br>**L4** | AC127-019-B-ML<br>AC254-050-B-ML | 19<br>50 |

Table 5.2: Table of the optical components used on the lab characterisation. All listed parts are from the Thorlabs online catalogue.

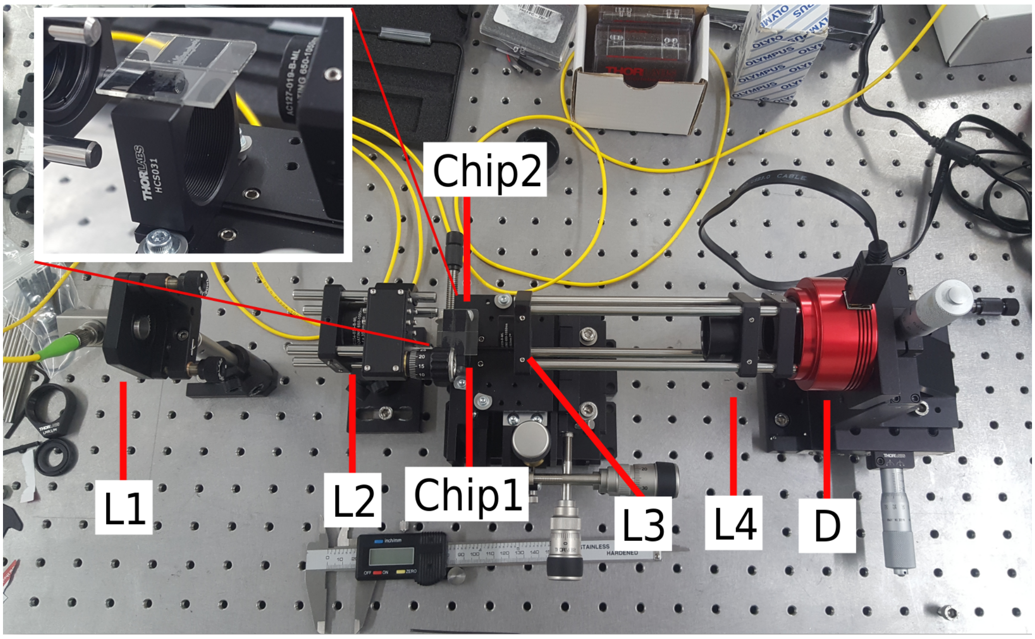

Figure 5.5: Throughput test apparatus in the laboratory for measuring the performance of the optical chip substrates. The SMF-28 (yellow) transfers the light from the LED to the collimation optical element (L1) where it is focused into the chip with the optical lens (L2). Both chips are attached side by side on the 5-axis translation stage. A combination or re-imaging optics (L3, L4) are used to focus the output of the chips into the detector (D). The detailed optical components that were used are listed in Table 5.2.

## 5.2 Results

In this section the throughput performance results for a range of astrophotonic reformatters inscribed into two substrate chips using different inscription laser pulse energies are presented. Initially, I present an overview of the results, and in the following subsections they are grouped into three divisions according to their inscribed geometry architecture as described in Section 5.1.2.

### 5.2.1 Data acquisition and reduction

All data images were acquired with ASI-290MM mono CMOS detector, with a range of 20 milli-seconds up to 2 seconds of exposure time. For the throughput analysis three types of data images were collected:

1. **Output images**. These were taken at the near-field of each photonic device output after the injected beam was centred on the device's entrance and the throughput was maximised in the detector.

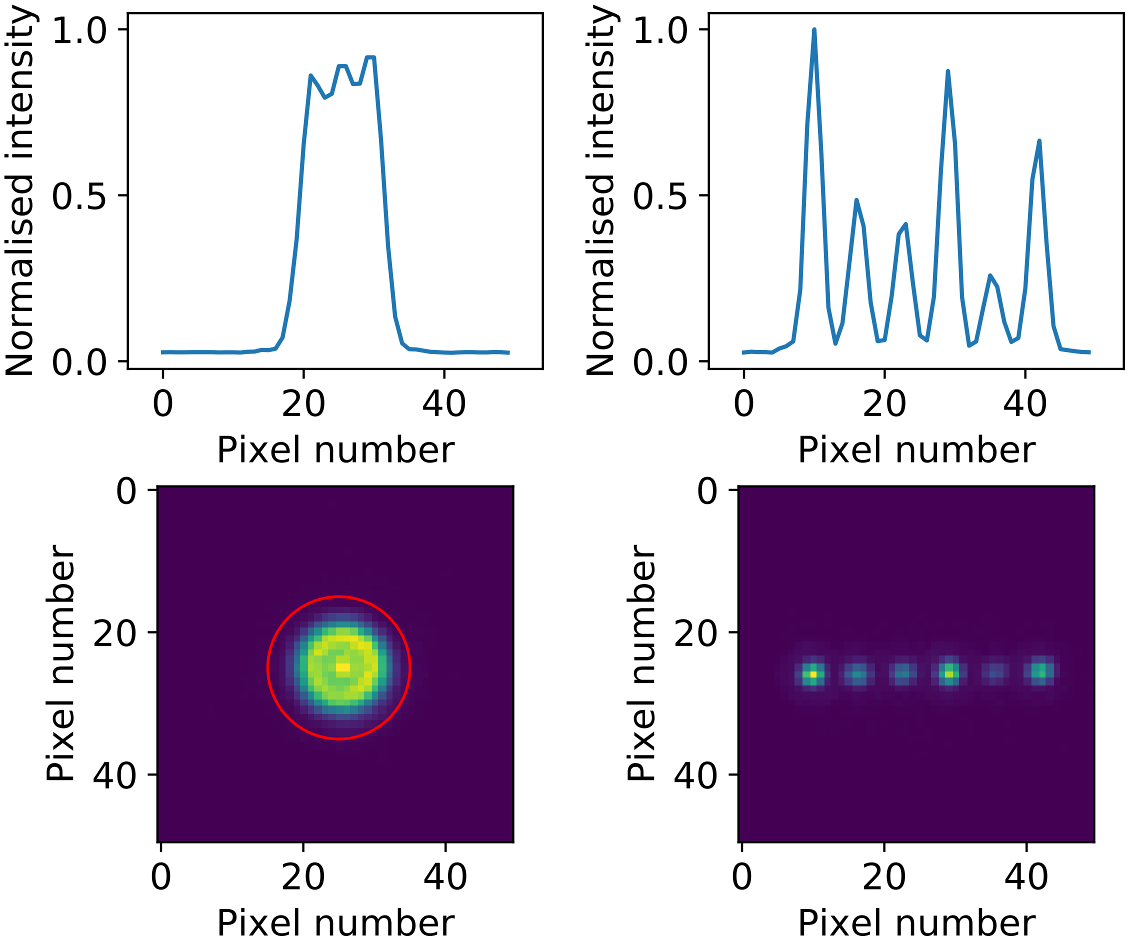

Figure 5.6: Examples of input and output images produced by the photonic reformatters. Here the RF-4 reformatter in chip#1 is shown with the corresponding injected beam of f#9.3 @600 nm. **Left panel**: The injected beam with a red circle showing the collecting area of the RF-4 input and its cross section profile on the top sub-figure. **Right panel**: The resulted output slit intensity of RF-4 astrophotonic reformatter with its intensity profile along the slit plotted on the top sub-figure.

2. **Input images**. These were acquired for the calibration of the output flux in the throughput calculation. This was done by shifting the astrophotonic chips laterally and focusing the beam into the detector by translating the mounts (see Figures 5.4 and 5.5).
3. **Dark frames**. These frames were used for the background subtraction of the the input and output images.

Figure 5.6 shows an example of input and output data images with their cross-section profile intensity normalised. Following the acquisition of data-images, the averaged dark frames were subtracted from the input and output images to filter the detector noise background and abnormal (hot, dead) pixels. In the next step, a Gaussian smoothing algorithm was applied on the data for object recognition in the images in combination with a flood fill algorithm that compliments the recognition using joined pixels. In that way, by adjusting the background level of identified objects in each frame, small features not belonging to the astrophotonic device under investigation were removed. After that, the flux within the identified region was calculated and saved. The throughput of each of the astrophotonic devices was calculated from the ratio of the flux in the averaged output frames over the averaged input frames taking into account of the exposure time of each set. This is shown in equation 5.1 where $T_{\text{tot}}$ is the total throughput (not accounting for coupling losses), $F_{\text{out}}$ is the flux in the output of each device (slit), $F_{\text{in}}$ is the flux injected into each device, $t_{\text{out}}$ and $t_{\text{in}}$ are the exposure times respectively. This was done for all the devices.

$$T_{\text{tot}} = \frac{F_{\text{out}} t_{\text{in}}}{F_{\text{in}} t_{\text{out}}}. \tag{5.1}$$

### 5.2.2 Laboratory throughput results

Here I present the throughput performance results as described in section 5.1.4. After the data reduction, the throughput performance of the each of the device was calculated using the equation 5.1. The laboratory throughput results for all of the astrophotonic reformatters at 600 and 800 nm are presented in Table 5.3 for chip#1 and Table 5.4 for chip#2. The maximum calculated value amongst them was 14.4%±0.2% corresponding to the RF-4 device for an $f\#13$ beam at 800 nm, while its total performance was among the best. The errors are the standard deviations calculated for all of the devices ranging from 0.2 to 0.9 %. All the devices showed their throughput maximum for an $f\#9$ injected beam at 600 nm and for an $f\#14$ injected beam at 800 nm.

The best performing astrophotonic reformatter RF-4 was found to be similarly efficient as well in the other wavelength band and on chip#2. Its throughput performance is presented in Figure 5.7. By visual inspection it is apparent that the throughput of RF-4 across the different wavelengths and inscribed chips is uniform and presents a similar trend. In particular, the maximum throughput at the wavelength of 600 nm is observed for an $f\#10$ injected beam for chip#1, presenting a dropoff for smaller and bigger values of $f\#$, while for the longer wavelength of 800 nm the best throughput is observed for an $f\#13$ injected beam.

| | **Chip#1 Throughput (%)** | | | | | | | | | |
|---|---|---|---|---|---|---|---|---|---|---|
| **Wavelength** | **600 nm** | | | | | **800 nm** | | | | |
| **Injected $f\#$** / **Component** | 7.09 | 9.33 | 11.2 | 13.07 | 18.67 | 7.09 | 9.33 | 11.2 | 13.07 | 18.67 |
| **MM** | 3.98 | 4.50 | 4.28 | 3.43 | 3.25 | 9.45 | 10.90 | 12.30 | 12.48 | 11.98 |
| **RF-1** | 9.39 | 9.88 | 9.78 | 6.57 | 6.38 | 7.44 | 8.97 | 9.05 | 9.06 | 8.30 |
| **RF-2** | 2.45 | 2.72 | 2.64 | 2.35 | 2.04 | 5.64 | 7.89 | 8.09 | 8.22 | 7.76 |
| **RF-3** | 8.69 | 10.38 | 9.37 | 8.23 | 6.05 | 9.40 | 11.62 | 12.05 | 12.63 | 12.37 |
| **RF-4** | 10.67 | 13.96 | 13.75 | 9.11 | 7.30 | 9.64 | 13.16 | 13.69 | 14.39 | 13.90 |
| **RF-5** | 4.29 | 4.85 | 4.49 | 3.88 | 3.50 | 6.84 | 8.20 | 8.24 | 8.52 | 7.95 |
| **RF-6** | 7.40 | 8.30 | 7.49 | 6.45 | 5.56 | 3.35 | 9.34 | 9.47 | 9.90 | 9.71 |
| **RF-7** | 3.95 | 5.04 | 5.32 | 5.15 | 4.90 | 8.62 | 10.71 | 10.72 | 11.6 | 11.4 |
| **RF-8** | 8.58 | 10.70 | 10.33 | 10.02 | 10.13 | 10.15 | 12.46 | 12.88 | 14.05 | 14.0 |
| **RF-9** | 2.09 | 2.37 | 2.27 | 2.00 | 1.81 | - | - | - | - | - |
| **RF-10** | 1.52 | 1.87 | 2.01 | 1.98 | 1.97 | - | - | - | - | - |
| **RF-11** | 0.62 | 0.73 | 0.77 | 0.73 | 0.77 | - | - | - | - | - |

Table 5.3: Throughput performance of the chip#1 at the wavelengths of 600 and 800 nm.

| | **Chip#2 Throughput (%)** | | | | | | | | | |
|---|---|---|---|---|---|---|---|---|---|---|
| **Wavelength** | **600 nm** | | | | | **800 nm** | | | | |
| **Injected $f\#$** / **Component** | 7.09 | 9.33 | 11.2 | 13.07 | 18.67 | 7.09 | 9.33 | 11.2 | 13.07 | 18.67 |
| **MM** | 12.61 | 12.65 | 10.62 | 9.48 | 6.62 | 14.24 | 16.18 | 16.10 | 16.48 | 13.66 |
| **RF-1** | 5.94 | 6.47 | 6.15 | 6.05 | 5.20 | 7.66 | 7.97 | 7.98 | 8.01 | 7.9 |
| **RF-2** | 7.97 | 8.61 | 7.76 | 7.39 | 6.53 | 8.07 | 8.35 | 8.57 | 8.95 | 8.57 |
| **RF-3** | 11.96 | 12.3 | 12.26 | 10.25 | 8.71 | 6.39 | 7.19 | 7.41 | 7.51 | 6.58 |
| **RF-4** | 12.44 | 12.34 | 11.35 | 9.44 | 7.36 | 8.33 | 9.01 | 9.20 | 9.44 | 8.28 |
| **RF-5** | 5.87 | 6.45 | 4.62 | 5.78 | 5.74 | 6.67 | 7.39 | 7.40 | 7.89 | 7.62 |
| **RF-6** | 10.03 | 10.34 | 9.67 | 7.84 | 7.53 | 7.26 | 7.75 | 7.87 | 8.03 | 6.93 |
| **RF-7** | 9.83 | 10.13 | 9.76 | 8.74 | 7.72 | 6.70 | 7.69 | 7.87 | 7.73 | 7.62 |
| **RF-8** | 10.23 | 10.43 | 10.18 | 9.98 | 9.88 | 4.29 | 5.03 | 5.23 | 5.27 | 4.70 |
| **RF-9** | - | - | - | - | - | - | - | - | - | - |
| **RF-10** | - | - | - | - | - | - | - | - | - | - |
| **RF-11** | - | - | - | - | - | - | - | - | - | - |

Table 5.4: Throughput performance of the chip#2 at the wavelengths of 600 and 800 nm.

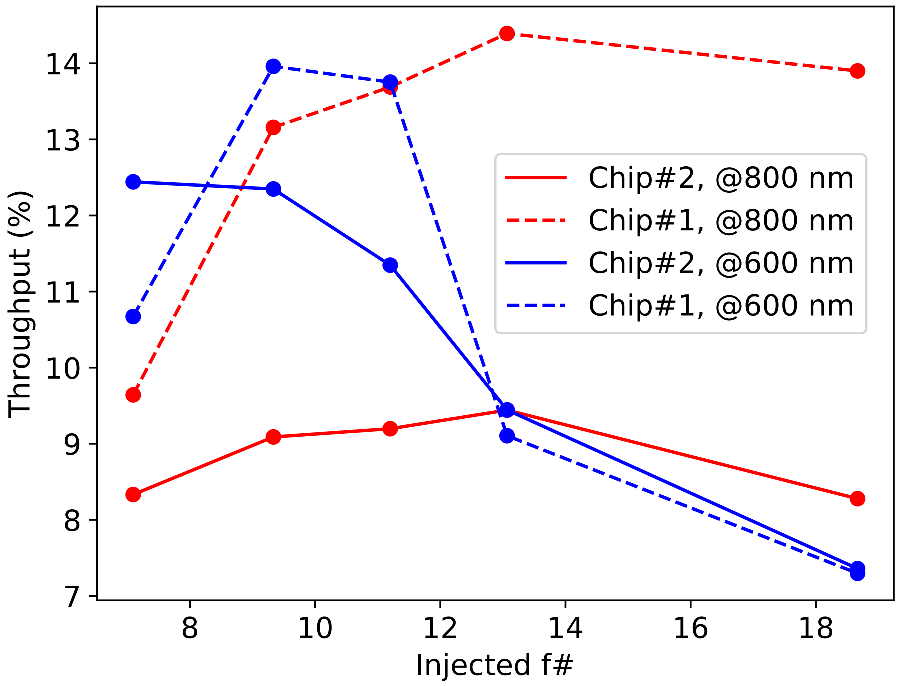

Figure 5.7: Throughput laboratory measurements of the RF-4 astrophotonic reformatter in the optical chip#1 and chip#2 versus the injected beam's $f\#$. This is shown for the wavelengths of 600 and 800 nm.

As equation 2.20 dictates, the number of propagated modes ($N_{\mathrm{MM}}$) into a step-index MM waveguide approximately is given by

$$N_{\mathrm{MM}} \approx \frac{V^2}{4} = \left(\frac{2\pi a NA}{\lambda}\right)^2. \tag{5.2}$$

Consequently, there is a certain value of $NA$ or $f\#$ for a given wavelength that the waveguides support the maximum estimated number of spatial modes. This effect is obvious in the multi-wavelength throughput results.

### 5.2.3 Astrophotonic reformatters – Optimising the pitch

As explained thoroughly in section 5.1.2 a set of four different astrophotonic reformatters with a different pitches for their waveguides at the entrance and exit slit, were inscribed into the two substrates. This was done to identify the pitch combination that produces the best throughput result. The measured throughput of this parameter scan as a function of injected $f\#$ are presented in Figure 5.8.

As is immediately apparent from the figure, the best performing reformatter is the RF-4 across all wavelengths at both of the optical substrates. The RF-4 device, with a combination of pitch values between entrance and exit of 5-7 µm, achieved a throughput of more than 12% for both of the chips at the wavelength of 600 nm for an $f\#9$ beam and at 800 nm for an $f\#13$ beam.

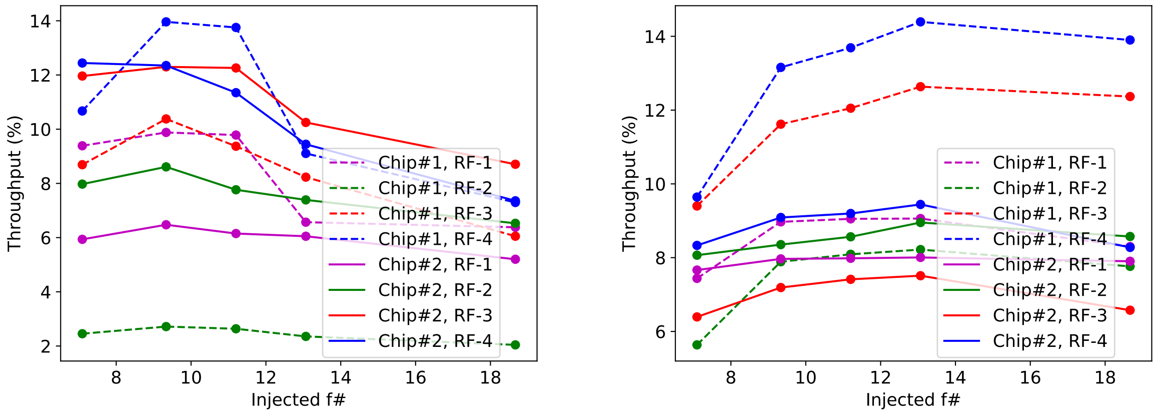

(a) (b)

Figure 5.8: Throughput lab results of the output slit ends for the devices RF-1-4 from both of the optical chips versus the injected $f\#$. This is shown for the wavelengths of (a) 600 and (b) 800 nm.

### 5.2.4 Optimising the transition reformatting plane length

After determining the optimal pitch-set for the input and output, the next step is to assess the optimal last transition length, evaluating the inscription parameters of the reformatters RF-5-8. On this particular transition plane, the waveguides reform to a linear output slit. The transition length geometry affects the loss of light and the coupling of the evanescent field into the waveguides further on at the output end slit.

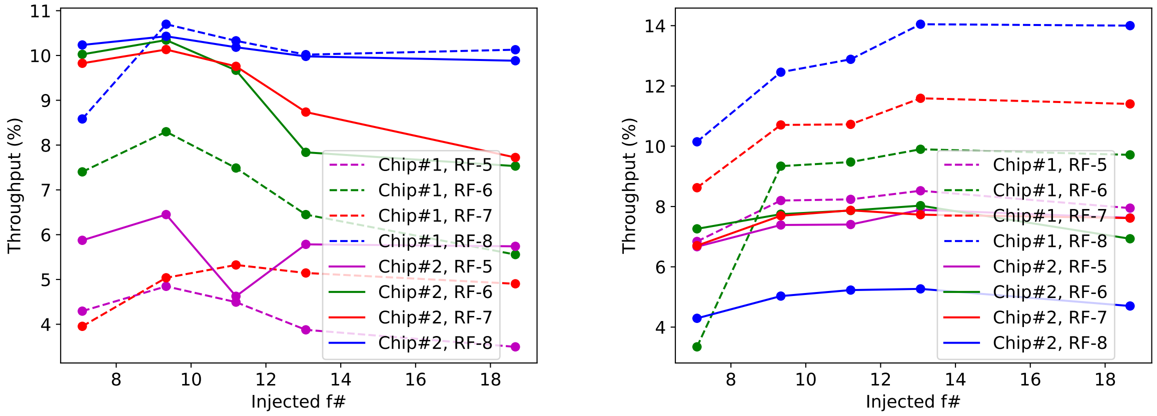

(a) (b)

Figure 5.9: Throughput lab results of the output slit ends for the devices RF-5-8 from both of the optical chips versus the injected $f\#$. This is shown for (a) 600 and (b) 800 nm.

The outcome of this parameter scan is presented in Figure 5.9 where is apparent that the best performing device is the RF-8 on the chip#1 showing a throughput of almost 11% at 600 nm and slightly more than 14% at 800 nm.

### 5.2.5 Optimising the off-axis lateral step devices

After the ideal pitch ratio and transition length of the waveguides were investigated, I further examined astrophotonic reformatters' behaviour with respect to the side step lateral shift of output slit compared to the input on-axis centre of the pentagon wave-channel arrangement. This is rather useful for measurements where the evanescent field does not couple into the waveguides of the device influencing the data measurements.

The results of this study are summarised in Figure 5.10. It is apparent from the figure that the light losses due to the lateral shift are rather high, manifesting a maximum throughput of slightly more than 2.3% for the reformatter with a side step of 2 mm. This result is expected as the lateral shift (2 mm) is more than 180 times larger than the radius of the MM input (5 µm) of each of the reformatters. Across the longer wavelength of 800 nm these reformatters demonstrated negligible throughput close to 0% similar to the devices at the chip#2 for both of the wavelengths. The maximum throughput for each of the reformatters was found to be similar to previous results for a $f\#9$ beam for the wavelength of 600 nm.

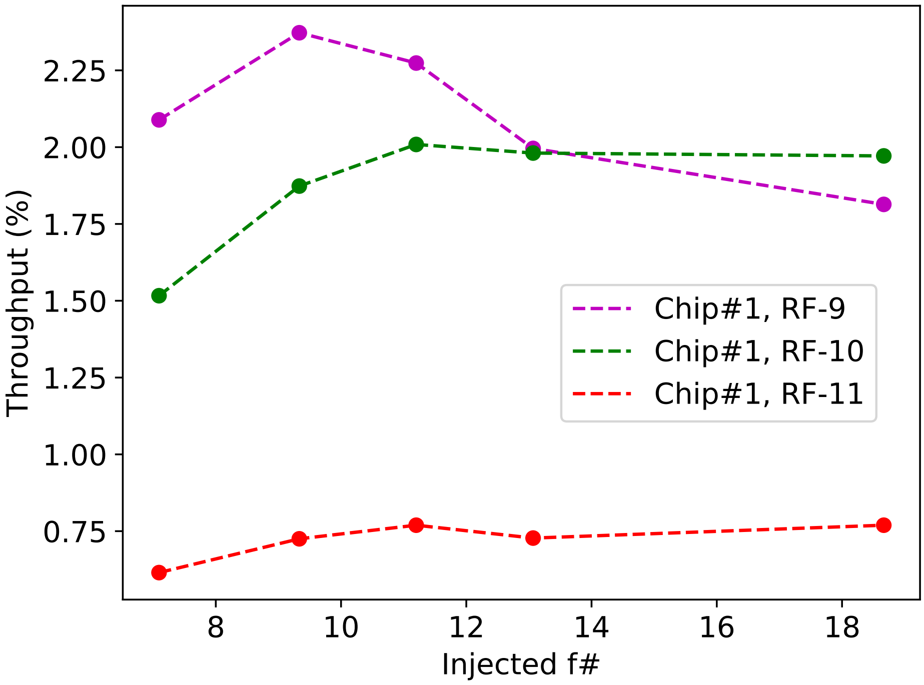

Figure 5.10: Throughput lab results of the output slit ends for the devices RF-9-11 from both of the optical chips versus the injected $f\#$. This is shown for the wavelength of 600 nm.

### 5.2.6 Simulated `BeamPROP` comparison

To investigate areas of improvement on the device's throughput performance, the `BeamPROP` module from `RSoft` was used to simulate the RF-4 astrophotonic reformatter (see Figure 5.11). The refractive indices values are taken from the literature for the substrate material [1] as well as the approximate refractive index profile of the inscribed waveguides (Arriola et al. 2013). The simulation setup was composed of a simulated version of the SMF-28 in conjunction with the astrophotonic reformatter considered as close as possible to the laboratory measurement conditions.

The resulting maximum throughput of the simulation was 55.1% and 56.1% for 600 and 800 nm respectively (see Figure 5.12 for the `BeamPROP` CAD panel at 600 nm). The simulation results are almost five orders of magnitude larger than the experimental results, indicating that either the simulation didn't take into account the true parameters of the refractive index profile of the inscribed waveguides, or the behaviour of such devices in the optical regime is quite sensitive leading to non-ideal inscribed waveguides of low throughput.

---

[1] `https://refractiveindex.info/?shelf=glass&book=CORNING-display&page=EagleXG`

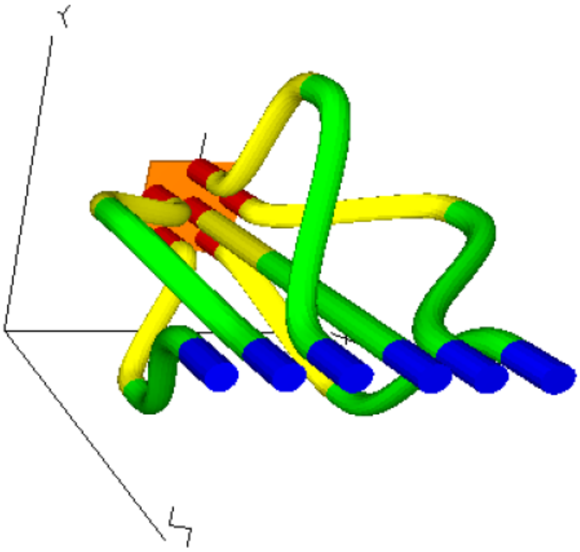

Figure 5.11: The RF-4 device of the chip#1 3D design as appears in the `RSoft` CAD environment. The colours indicate the four different transition planes used. Red colour represents the entrance and blue the exit pseudo-slit.

## 5.3 Discussion

### 5.3.1 Multi-mode waveguide performance

As described above in section 5.1.2, to better understand the throughput performance of the inscribed devices, a straight line MM device without any bend was inscribed into each of the substrates. This MM was composed of 6 individual waveguides in a pentagonal arrangement similar to the MM input of all the reformatters. The pitch of the waveguides of the straight-line MM device was 5 µm, similar to the entrance of RF-3 and RF-4 devices (see Table 5.1).

As the measured throughput suggests (see Table 5.3 and Table 5.4), the performance of the MM devices in chip#1 was inferior to the rest of the reformatters that had a non-straight-line arrangement along the substrate. However, in chip#2 the performance of the MM waveguide, is as expected, superior to the rest of the reformatters as there is only the material and coupling loss of light that is happening and not the loss due to the bend of the waveguide structure.

Following a similar procedure as in section 5.2.6 the straight MM devices were simulated. The results showed a throughput of 53.82% at 600 nm and 56.02% at 800 nm. These results are multiple orders of magnitude larger than the measured results, highlighting that either the structure of the inscribed

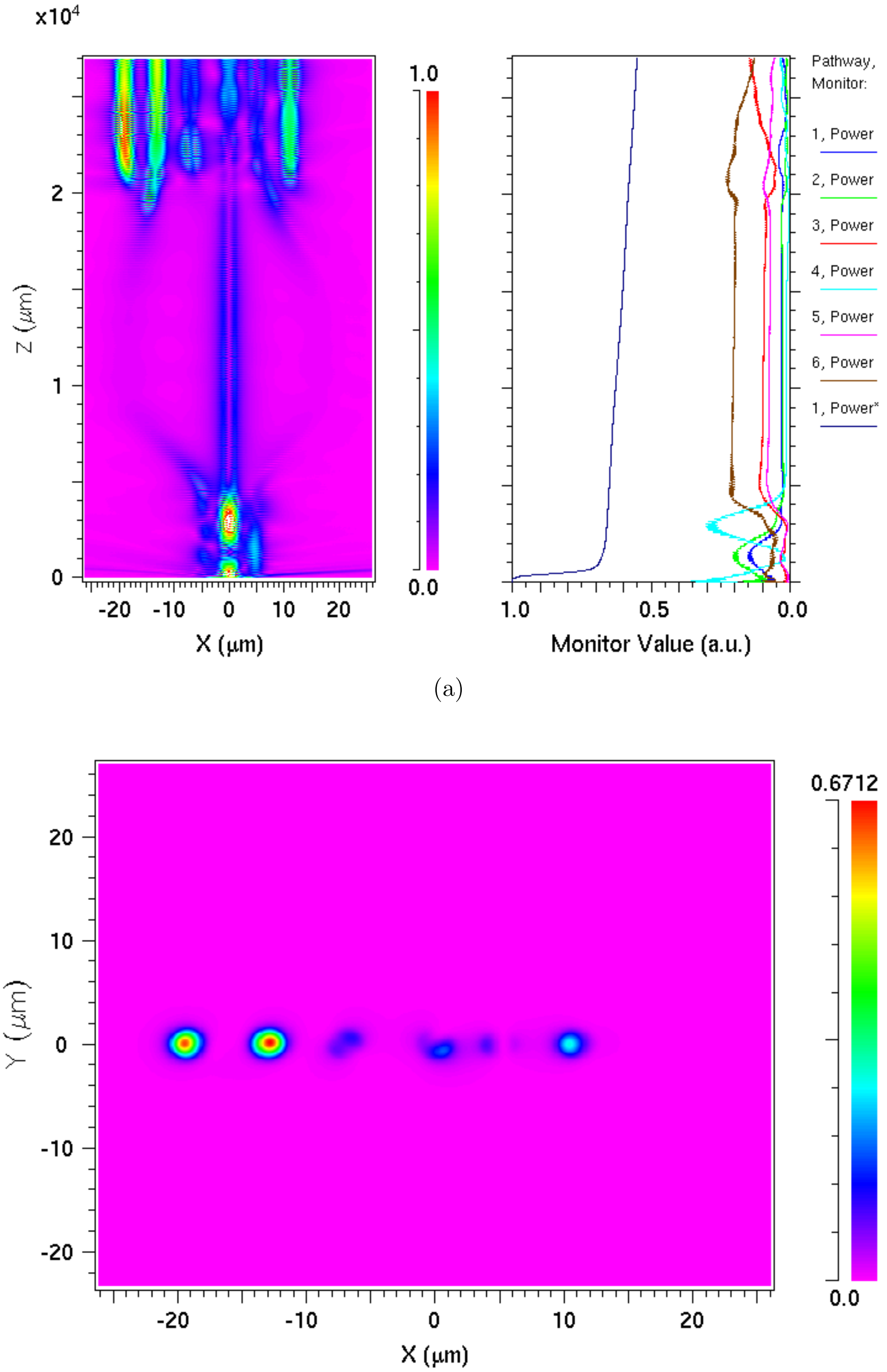

(a)

(b)

Figure 5.12: Throughput simulation results of the RF-4 astrophotonic reformatter. Top panel (a) shows the intensity of the propagated light through the device at a plane of the simulation domain where on the right the total throughput (black line) and the partial throughput of each of the individual waveguides are shown. Bottom panel (b) shows the output intensity of the slit end. This is shown for the wavelength of 600 nm.

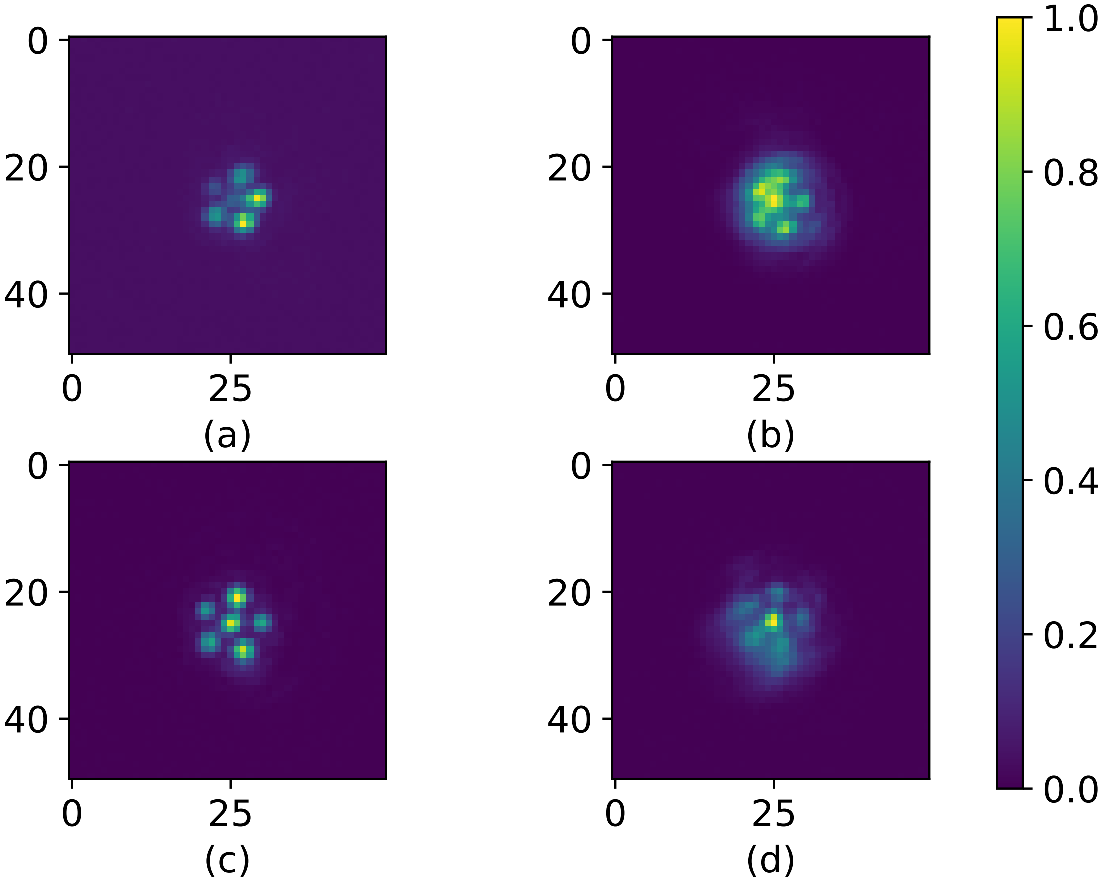

Figure 5.13: Near-field intensity distributions for the MM devices across both chips and wavelengths. (a)Chip#1 @600 nm, (b)Chip#1 @800 nm, (c)Chip#2 @600 nm, (d)Chip#2 @800 nm. All of the x-y axes of the images display the pixel numbers.

devices was quite different from the simulated one, or the laboratory measurements were not accurate (**quite impossible**). It should be mentioned as well that the MM devices during laboratory measurements had a different focal point than the rest of the reformatters which were the same.

Figure 5.13 illustrates the near-field intensity images of the MM structures at different wavelengths and for different chips. It is immediately apparent from the figures that not all of the individual waveguides are coupled with light and that there is a rather high evanescent field propagating outside of the waveguides. These facts and the intensity distribution around the waveguides (see Figure 5.13 (b), (d) sub-figures) indicate that the inscribed waveguide structure was not particularly efficient in light confinement, particularly at longer wavelengths.

## 5.3.2 Butt-coupled fiber into the astrophotonic reformatter

To connect the SMF-28 fiber and the best throughput-performing astrophotonic reformatter, I will follow the pigtailing process (e.g. Cvetojevic et al. 2017; MacLachlan et al. 2017). This enables to position the fiber end at the telescope's focal plane while the other end is positioned at the entrance of the instrument (i.e. a spectrograph).

The procedure will be as follows: between the fiber and the reformatter, a glass ferrule will be installed using an optical adhesive (Norland Optical Adhesive 61). The coupling from the fiber to the end of the reformatter will be optimised, then the glass ferrule will be inserted at the end of the stripped SMF-28. After that, the optical adhesive will be applied to all interfaces and the ultra-violet curing will be achieved while the coupling is continuously monitored. The whole connected structure will be supported on a microscope slide for rigidity. The resulting structure will be similar to the one illustrated in Figure 5.14.

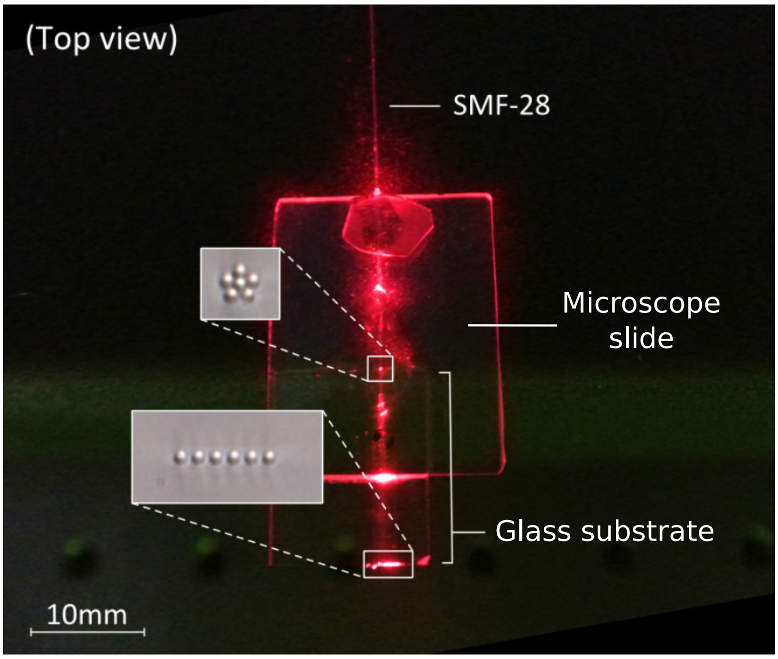

Figure 5.14: Illustration example of a pigtailed assembly composed of the SMF-28, the glass ferrule, the glass substrate and the supporting microscope slide underneath of them all. The device is illuminated using a HeNe laser coupled into the SMF-28 fiber entrance. Input and output planes of the chip are displayed in inset images. Image courtesy of Tobias Feger.

## 5.4 Conclusions

In this chapter I demonstrated a throughput characterisation of multiple composite astrophotonic reformatters fabricated by the ULI technique into two optical substrates. These were manufactured by the Optofab at Macquarie University. Each chip had a different inscription pulse energy, as well as uniquely-configured inscribed features. This was done intentionally to investigate the ideal geometry architecture of these devices in the optical wavelength regime.

The resulting measurements feature a maximum throughput performance of 14.4% at 800 nm, 41.7% lower than the simulated model comparison. The results suggest that inscribed astrophotonic reformatters using the optical substrate Corning Eagle2000 are rather low in light throughput efficiency. These show significant lower throughput performance compared with similar inscribed features operating at longer wavelengths, such as in the C-band (1550 nm) where they manifest a maximum throughput of 75-80% (Spaleniak et al. 2013).

The performance of the straight-line MM waveguide devices was found to be surprisingly low compared to simulations. An examination of the near-field images of their output showed the non-ideal effect of evanescent field as well as the unexpected modal coupling into the waveguides.

Aims for future work involve the investigation on selecting a better throughput performing material glass substrate to inscribe the devices, that had consistent inscription results in the optical wavelength regime. After addressing this, further tests on the inscribed devices will be performed to select the best of them. In the next step, a permanent connection of the SMF-28 fiber, acting as a few-mode fiber in the visible wavelengths, with the best performing astrophotonic reformatter will be accomplished. This will be used as an injection system of a high resolution compact diffraction-limited spectrograph coupled to a small diameter telescope. Spectroscopic measurements will be used to assess its performance in respect to spectroscopic efficiency and quality of measurements.

# Chapter 6

# First on-sky demonstration of the 3D-printed Mono-Mode Multi-core fiber spectrograph (3D-M3)

An alternative and more versatile type of fiber that can act as an IFU is the multi-core fiber (MCF), which shows potential to mitigate the problems explained in chapter 2.2. This is a combination of at least two fiber cores, which form an individual fiber using the same cladding formed by tapering-fusing methods. The precise position of the cores of a MCF can sample light across the focus of the image plane, making it ideal for making an IFU. By 3D printing structures on top of its cores using novel nanoprinting techniques, we save significant effort in assembly of the IFU, dramatically improve the free-space coupling of light into the fiber and relax the requirement for precise alignment of the input (e.g., Gissibl et al. 2016; Dietrich et al. 2016, 2017, 2018; Hottinger et al. 2018).

In Section 6.1 I discuss the conceptual design and parameters, followed by a description of the experimental setup to characterise performance. In Section 6.2 I present the laboratory and on-sky results. Finally, I present summarise in sections 6.3 and 6.4.

## 6.1 Methods

To efficiently inject light from an 8-m class telescope into the cores of a MCF and a diffraction-limited spectrograph the following elements are required: a high performance AO system, an IFU to dissect the focal plane image and direct light to the individual cores, the MCF fiber itself, and the spectrograph to feed which must be able to handle a multi-core input In this section these elements will be discussed in detail.

### 6.1.1 Instrument architecture

To simulate the instrument the information of all of its components should be available, from the resulting beam output of the telescope down to the detector. To begin with, the 8-m Subaru telescope delivers the starlight through the complex set of AO188 AO and SCExAO systems where the resulted output beam's intensity distribution is close to a Gaussian profile.

To efficiently couple light into the SM cores of the MCF, a custom fiber injection unit is required. This system has to be carefully optimised to match the parameters of the MCF, which has a 5.3 µm MFD @980 nm ($1/e^2$) (an illustration of the fiber's cross-section is presented in Figure 6.1) with a SM cut-off at ∼800 nm so that the fiber's cores are SM at longer wavelengths. The core-to-core spacing (pitch) of the MCF is 40 µm. This is important to make sure the cross-coupling of light between the cores is negligible as they are physically quite far apart from each other with a ratio of pitch/MFD of 7.5:1. To maximise the amount of light coupled to the fiber's cores, micro-optics are 3D printed on top of the cores using a custom lithography system described below. To demonstrate the potential of such an injection unit system, a compact-size spectrograph was build with off-the-shelf optics detailed in the following sections.

To spatially resolve a star surface without compromising the throughput, the selected plate scale was 0.45"/mm. That means that each fiber core subtends 18 mas on-sky, which is 20% smaller than the diffraction limit of the Subaru Telescope @980 nm (25.6 mas). As a reference, the Subaru telescope with the SCExAO facility is able to spatially resolve the surface of stars with an angular dimension of ∼ 50 mas, which is an apparent size a handful of giant stars on night sky, like, for example, Betelgeuse (alpha Orionis), or Aldebaran (alpha Tauri). The required focal ratio to achieve the 0.45"/mm plate scale was calculated to be $f\#57.5$.

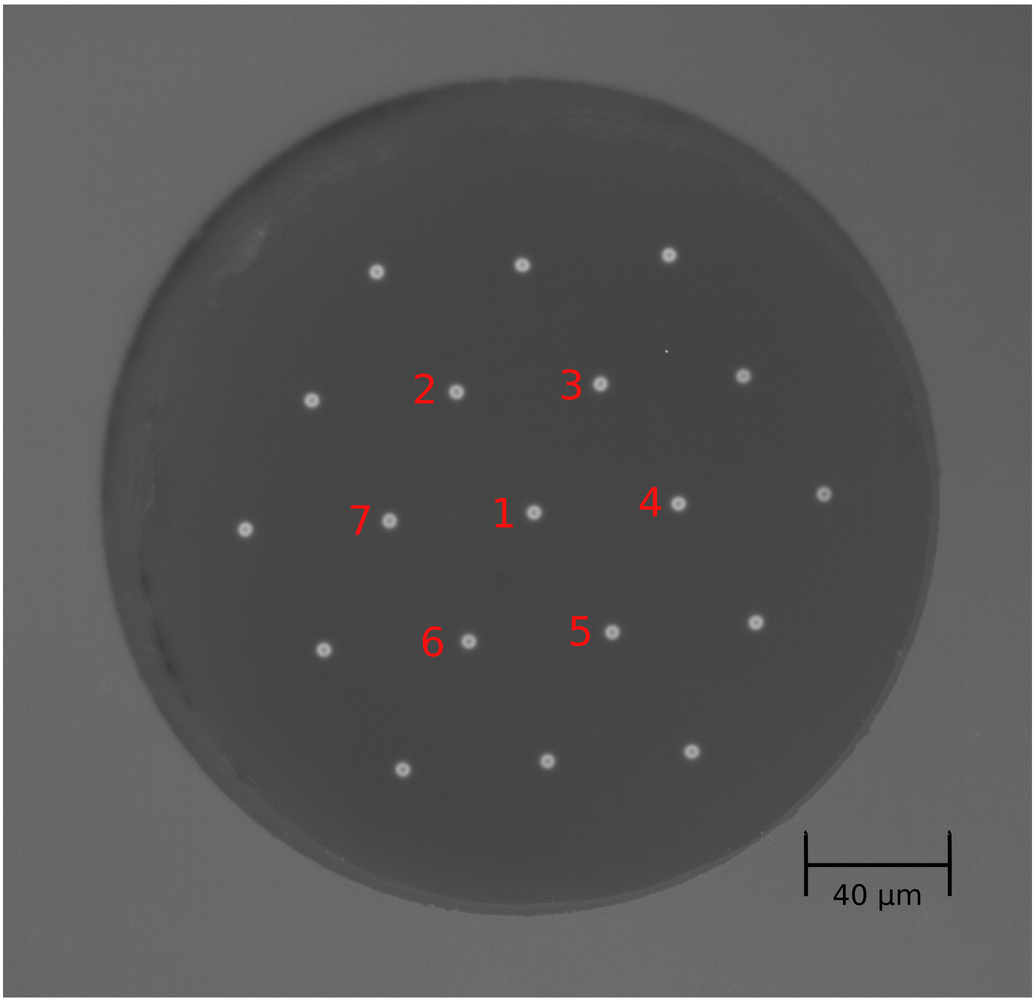

Figure 6.1: Microscope image of the polished multi-core fiber in its ferrule. The cores are visible in a hexagonal formation with a pitch of 40 µm. The fiber has a 5.3 µm mode field diameter @980 nm ($1/e^2$) and a cladding diameter of $\sim$ 220 µm. Here, the cores are back-illuminated with a white light source. Numbers in red are used for core referencing below.

### 6.1.2 The SCExAO infrastructure

SCExAO is installed at the NIR Nasmyth focus of the 8.2 m Subaru Telescope. Detailed information and schematic layouts of it are described in Jovanovic et al. (2015). Initially the starlight from the 8.2 m Subaru Telescope enters the AO188 facility, which offers 30-40% Strehl PSF correction in the H-band under moderate atmospheric seeing conditions (Hayano et al. 2008, 2010; Minowa et al. 2010). After a series of components in the optical train for manipulation of the beam, it is filtered using a dichroic when it enters SCExAO and diverges into two paths, the visible channel (<900 nm) and the NIR (>900 nm) channel. However, the wavelength response of the dichroic does not have a sharp cut-off profile and there is a slight overlap of wavelengths in both channels. After the starlight undergoes further wavefront corrections on the state-of-the-art pyramid wavefront sensor (PyWFS) to correct for higher-order spatial and temporal modes caused by the atmosphere, it is focused down using a gold-coated off-axis parabola (OAP) with $f$ = 519 mm onto the 3D-printed MCF facet. The 3D-printed end of the MCF was installed on the NIR bench of SCExAO (see Figure 6.2).

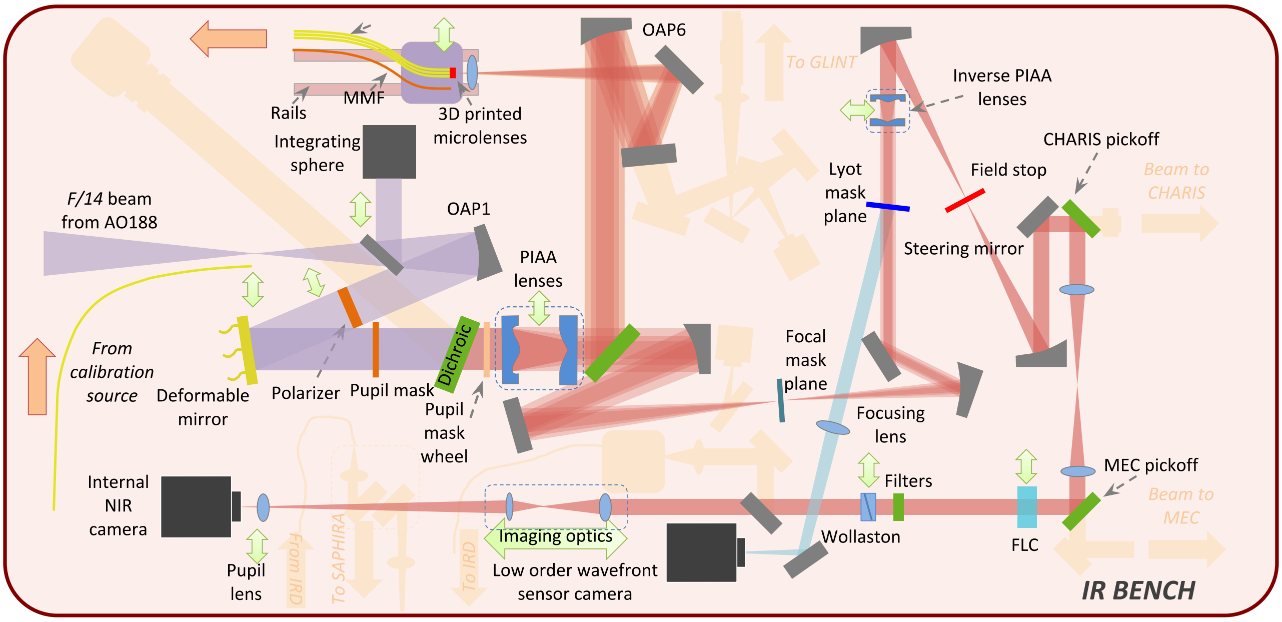
OAP6
To GLINT
Inverse PIAA lenses
CHARIS pickoff
Beam to CHARIS
Rails
MMF
3D printed microlenses
Integrating sphere
Lyot mask plane
Field stop
F/14 beam from AO188
OAP1
Steering mirror
PIAA lenses
From calibration source
Deformable mirror
Polarizer
Pupil mask
Dichroic
Pupil mask wheel
Focal mask plane
Focusing lens
Filters
MEC pickoff
Beam to MEC
Internal NIR camera
Pupil lens
From IRD
To SAPHIRA
To IRD
Imaging optics
Low order wavefront sensor camera
Wollaston
FLC
IR BENCH

Figure 6.2: Schematic illustration of the NIR bench of the SCExAO facility. The 3D-printed fiber is shown at top left of the layout diagram. The beam's optical path from the AO188 to the IFU is represented with purple and red colour.

### 6.1.3 Simulations

To simulate the output beam, the profile of the Subaru telescope and the SCExAO key parameters were used from the literature (e.g. Jovanovic et al. 2015, 2017).

The physical-optics propagation module of the commercial `Zemax` (Zemax 2016) ray tracing software was used to simulate the output beam profile of Subaru Telescope, including the effect of the Phase-Induced Amplitude Apodization (PIAA) optics (Lozi et al. 2009) installed into the NIR optical train of SCExAO where the fiber is positioned to sample starlight. This output was used as an input for optimising the performance of the micro-lens array (MLA) structure that forms the IFU.

To optimise the coupling efficiency of SCExAO's beam output at its image focal plane, the physical-optics propagation module was used again to model the surface shape of the MLA structure. Polynomials with coefficients up to the eighth order were used to model the MLAs' aspheric lens surfaces using a hexagonal aperture at the end of the lenses when the lenslets are merged together. Since the 3D printing method is able to achieve a printed structure surface root-mean-square (RMS) of 37 nm (Dietrich et al. 2018), the roughness of the structure is expected to be better than $\lambda/20$ at the wavelength of operation.

### 6.1.4 Micro-optics manufacturing process

The structure of the MLAs was directly printed in a single block using two-photon lithography. The material was a commercial negative-tone photoresist IP-Dip (Nanoscribe GmbH 2018). This MLA was printed on the cleaved MCF, which had previously been manually glued into an FC-PC connector and then polished to achieve a flat surface to enable straight-forward printing on the front face of the fiber. A lithography machine built in-house at our project partner, the KIT, was used to generate the lenses. The system is equipped with a 780 nm femtosecond laser (Menlo Systems GmbH 2020) and a 40x Zeiss objective lens with NA = 1.4. For high-precision alignment and writing with high shape fidelity, an in-house developed machine control software was used.

The fiber was back-illuminated with a red LED which was used together with machine vision to detect the 19 cores of the MCF and align the individual lenses to each core. To be able to compensate for any slight location and pitch variation of the individual cores of the MCF, the full 3D-model is generated only after core detection. Prior to printing, the individual models of the lenses are merged by a Boolean operation to avoid unnecessary double illumination. Automated detection of the fiber end-face tilt is employed and the structures are corrected accordingly. The writing distances between subsequent lines and layers, i.e., both hatching and slicing distance, were set to 100 nm. The fabricated structure is developed in propylene-glycol-methyl-ether-acetate (PGMEA), flushed with isopropanol, and subsequently blow dried. In the next stage, scanning electron microscopy (SEM) and vertically-scanned white-light interferometry (VSI) images of the structure were acquired to check the quality of the manufacture process (see Figure 6.3).

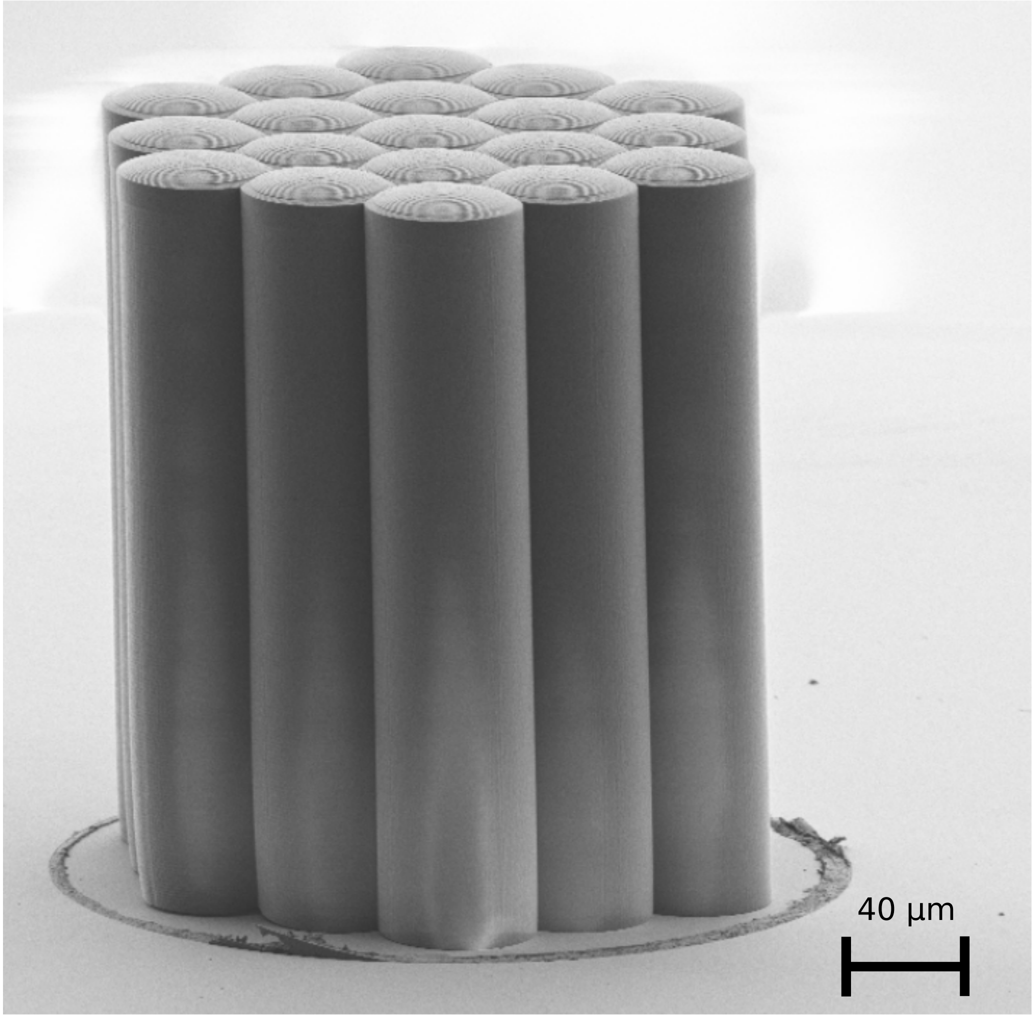

Figure 6.3: scanning electron microscopy image of the 3D printed micro-lens array structure on top of the multi-core fiber ferrule. All 19 cores were 3D printed, though only the inner 7 were used for the on-sky run.

### 6.1.5 Fibre injection unit

In order to achieve precise repeatable positioning of the injection fiber across the PSF of the target, a 5-axis remote controlled stage was used. The 5-axis stage (Newport, M-562-XYZ & 562F-TILT) was equipped with computer controlled stepper motors (Zaber, T-NA08A25) that allowed a minimum step translation of ∼50 nm and $< 1$ µm of unidirectional repeatability (see Figure 6.4). To align the fiber for tip-tilt, adjustments were performed manually when the L-bracket on which the fibers were mounted. The alignment of the fiber to the optical axis was achieved by adjusting the Gaussian illumination at the pupil to be centred while the fiber was back-illuminated with a HeNe laser. Immediately in front of the L-bracket, a -48 mm focal length plano-concave lens (Edmunds #67-995) was installed to re-adjust the injected $f\#$ to match that of the fiber. This was accomplished by using rails to translate the plano-concave lens and the 5-axis mount together and independently of each other. Using this arrangement a range of $\sim f\#$ from 28 to 60 could be achieved.

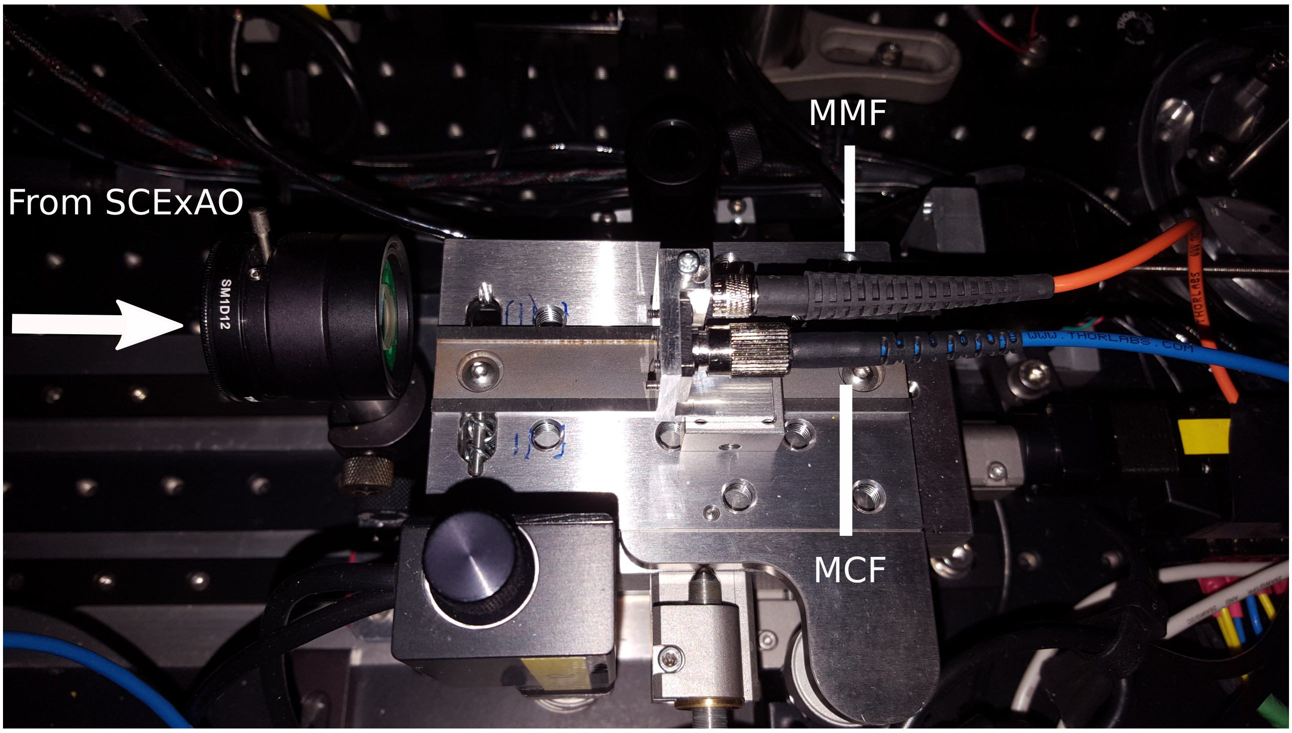

Figure 6.4: Illustration of the fibre-injection opto-mechanic setup on the SCExAO NIR bench. the 3D-printed multi-core fiber is using blue protection cable while the multi-mode fiber for calibration purposes, uses the orange one.

The L-bracket was designed to support 2 fibers, the MCF and another fiber with SMA connector. On the SMA slot, a MMF was installed (365 µm core, NA = 0.22, Thorlabs - FG365LEC) to calibrate the throughput measurements as the 5-axis stage moves laterally.

In order to achieve $f\#$ of 57.5 (see section 6.1.1), the spacing between the focusing OAP ($f = 519$ mm), the concave lens and the fiber was adjusted. The `Zemax` simulations served as a reference starting point. In a later stage, it was further adjusted using a detector to confirm the required $f\#$.

### 6.1.6 Throughput setup

To measure the total throughput performance of the custom injection 3D-printed MCF, a throughput test experiment was constructed. A graphical illustration of this setup is presented in Figure 6.5. The light from each of the fibers was collimated using a set of microscope lenses; L1 - Thorlabs RMS20X-PF for the MMF and L2 - Thorlabs RMS4X-PF for the MCF. Both beams were directed towards a 50:50 non-polarizing beamsplitter (BS) (Thorlabs CM1-BS014). After the BS, a 50 mm achromatic lens (L3 - Thorlabs AC254-050-B-ML) was used to re-focus the light on the detector (D - ASI-120MM-S mono). To measure the total throughput (including the coupling losses) of the MCF, the throughput of the MMF was used to calibrate the absolute flux. This was achieved by translating the 5-axis stage at the telescope beam's focus to couple it to each core of the MCF input, and then normalising each collected signal by the flux measured in the MMF.

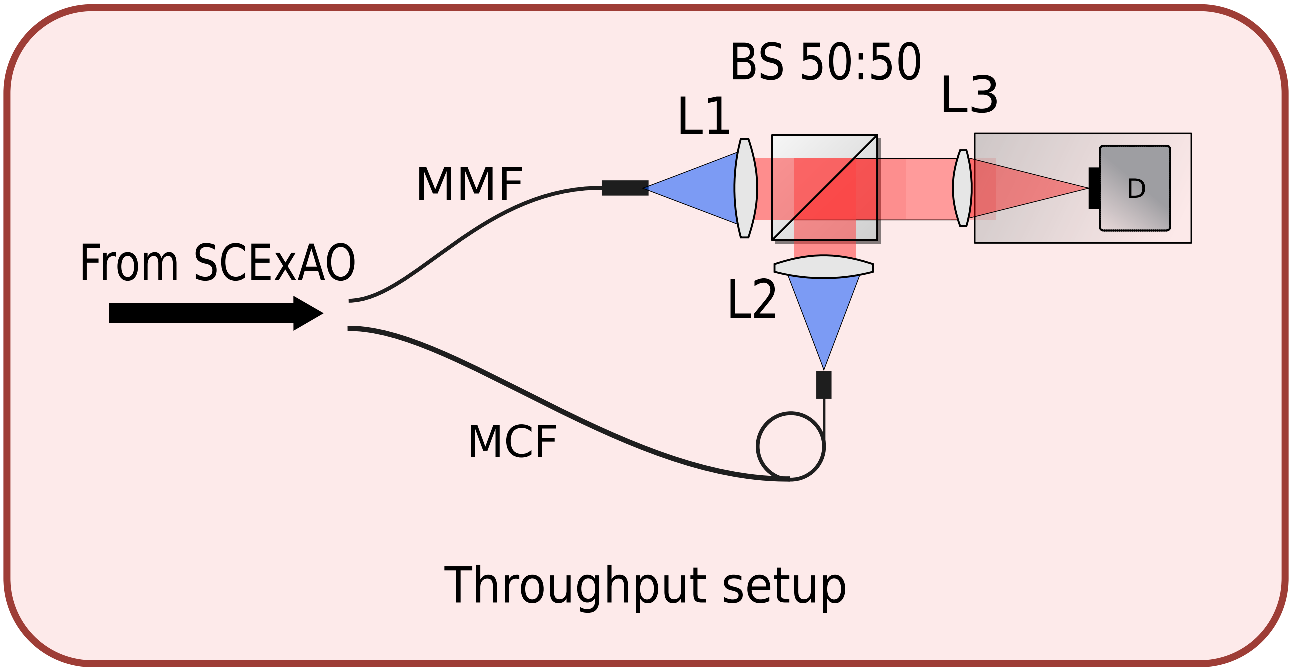

Figure 6.5: Throughput setup for measuring the efficiency of the 3D printed multi-core fiber. Calibration is achieved using a multi-mode fiber, lenses (L1-L2-L3) for collimation and focusing of the beam, beamsplitter (BS) and CMOS detector (D) for sampling the light output.

### 6.1.7 Spectroscopic setup

To show the potential of using 3D printed microlenses in conjunction with an MCF, a spectrograph similar to the Replicable High-resolution Exoplanet and Asteroseismology Spectrograph (RHEA)@Subaru design (Feger et al. 2014; Rains et al. 2016) was built. The benchtop instrument is a compact diffraction-limited échelle spectrograph using only off-the-shelf components, named 3D-M3.

As illustrated in Figure 6.6, the spectrograph was composed of the 3D printed fiber (P1), a combination of optic lenses to collimate the beam (P2) (EO#49-656-12mm, EO#47-655-INK-36mm, Thorlabs TTL200-A) an échelle R2 grating (P3) (Thorlabs GE2550-0363) for dispersion, then cross-dispersion using a transmission grating (P4) (2" 200 l/mm Baader Planetarium) and finally a lens (P5) (Thorlabs TTL200-B) to focus the beam onto the detector (P6) (ASI-183MM-pro mono).

3D-M3 makes use of only the 7 inner cores of the MCF out of 19 in total. A custom aperture to mask off the outer ring of 12 cores was positioned in between the MCF exit and the FC/PC connector mounted on the spectrograph side. Blocking the 12 outer cores was necessary to avoid overlapping of cores on the detector. The MCF was rotated until all the spectra from the individual cores were well separated and equidistant (see Figure 6.10 bottom panel), following the method described in Leon-Saval et al. (2012). The resolving power of the spectrograph was measured as 30,000 at 1 $\mu$m, while the footprint of the spectrograph is $300 \times 600$mm. It was installed on the Nasmyth NIR platform of the Subaru Telescope.

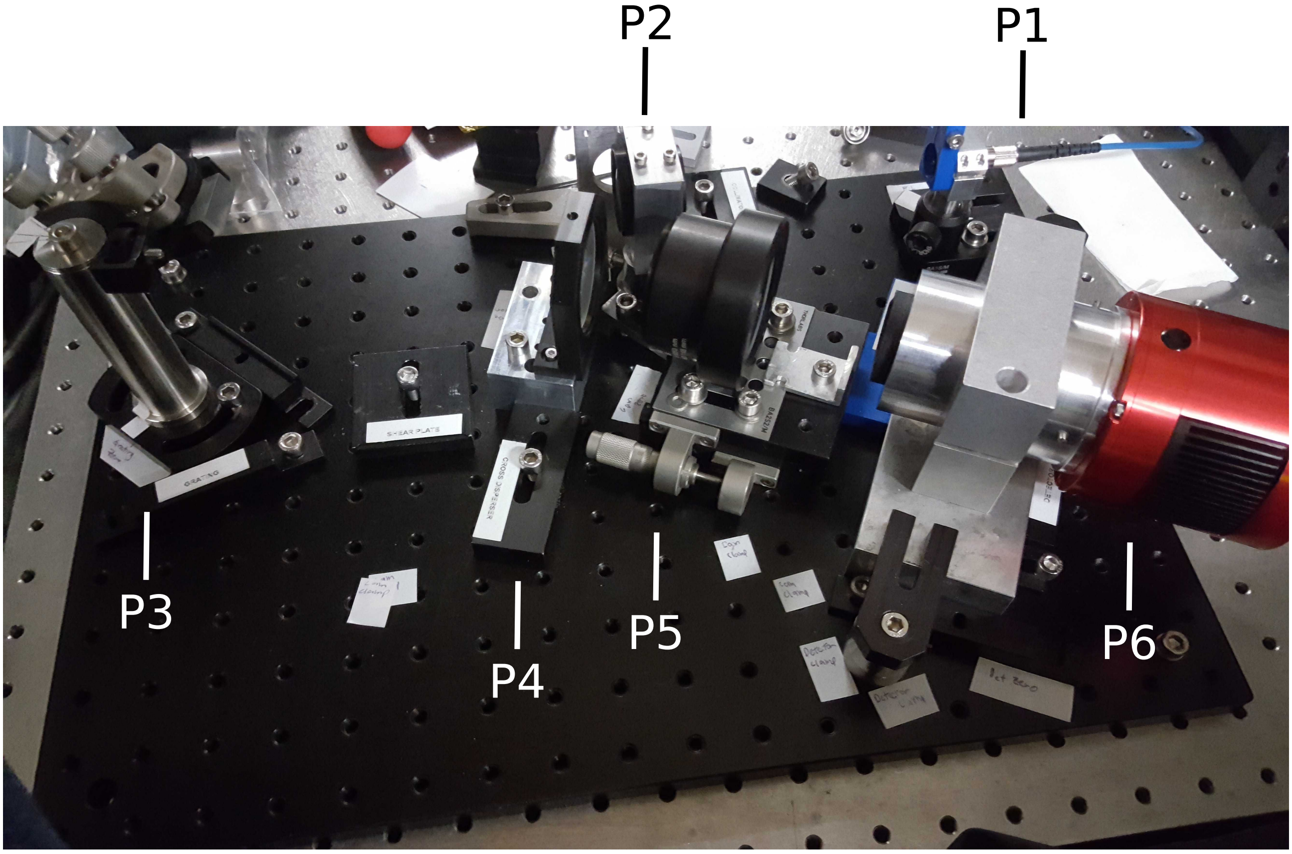

Figure 6.6: Spectroscopic setup of the 3D-printed Mono-Mode Multi-core fiber spectrograph using only off-the-shelf components. The footprint of the breadboard is 300 × 600 mm. The light injected from the 3D printed fiber (P1) was collimated by an optic (P2) before it was chromatically dispersed from an échelle grating (P3), cross-dispersed using a transmission grating (P4) and focused down using an optic (P5) on to the detector (P6).

## 6.2 Results

### 6.2.1 Laboratory throughput results

Here we present the throughput performance results for the injection system described in section 6.1.6. SCExAO is equipped with an internal calibration system using a Fianium supercontinuum source to inject light using an endlessly SMF delivering a broadband (from visible to K-band) diffraction-limited PSF into the facility following the same optical path as the light enters from the Subaru telescope and the AO188 facility. This source was used to inject light into SCExAO (see Figure 6.4) reaching the 3D printed MCF facet. Exposures of a fraction of a second were acquired from both fiber, the MCF and the large MMF used as a reference, using the experiment apparatus described in section 6.1.6. This setup was used to filter the light sampled by the detector from the adjacent cores of the fiber end. Dark frames were also recorded, which were averaged and subtracted from the data frames before further processing.

Two different experiments were performed to calculate the throughput performance of the IFU; on the first the maximum coupling of light into each core was calculated by measuring the optimal throughput after centring the incoming light on the fiber core, and on the second the sensitivity of coupling efficiency to misalignment of the injected beam was calculated by measuring the throughput of the central core of the MCF as the injected beam was laterally translated by steps of 5 µm in order to evaluate the performance of the fiber in a more realistic scenario where the target affected by the atmosphere perturbations will be moving.

To normalise the throughput of the MCF, the MMF throughput was also measured. Through simulation we determined that the MMF coupled all of the injected light. Therefore, we could use the power coupled into the MMF to normalise the flux from the MCF. To this end, we scanned the 5-axis stage to optimise the coupling into each core. We then normalised this measurement by that of the MMF to determine the throughput.

The results were derived using the PIAA optics of SCExAO. The results of the first experiment are shown in Figure 6.7 and it is apparent that the average throughput was 35.76 ± 0.3 (percent) and reach a maximum value that was 5 percent higher than the average equal to 40.7 ± 0.6 (percent). From the average calculation the low throughput of the fiber core #2 (12.3 ± 0.2) was excluded as it was not representative of the rest of the lenlets structure due to manufacture errors. The maximum achieved throughput corresponds to 83 percent of the theoretical expected value (48.8%) according to `Zemax` calculations. It should be mentioned that Fresnel reflection from the surfaces of the MLA, MCF and impurities of imperfectly polished fiber facets are not taken into account in the throughput calculation. The throughput across all the 7 lenslets when illuminated by a single, unresolved star was measured to be 70% ± 0.3 percent while the simulated is 83% (84.8% of the theoretical value).

The results of the second experiment are shown in Figure 6.8 where it can be observed that the misalignment tolerances of the injected beam are relaxed using the micro-lenses, performing decently well even for a lateral ∼18 µm off-axis injection where they manifest 20% of their throughput maximum.

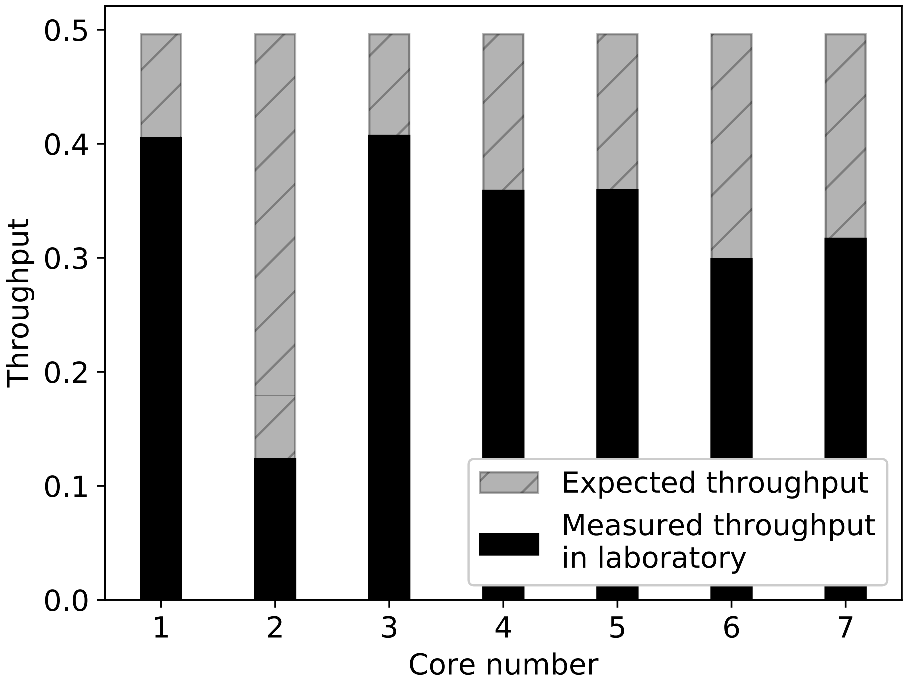

Figure 6.7: Throughput efficiency for each of the 7 cores of the fiber (see Figure 6.1 for the correspondence of core# to position on the fiber). Injected $f\#$ was fixed to $f\#57.5$ by positioning the carriage and the fiber to the desired location.

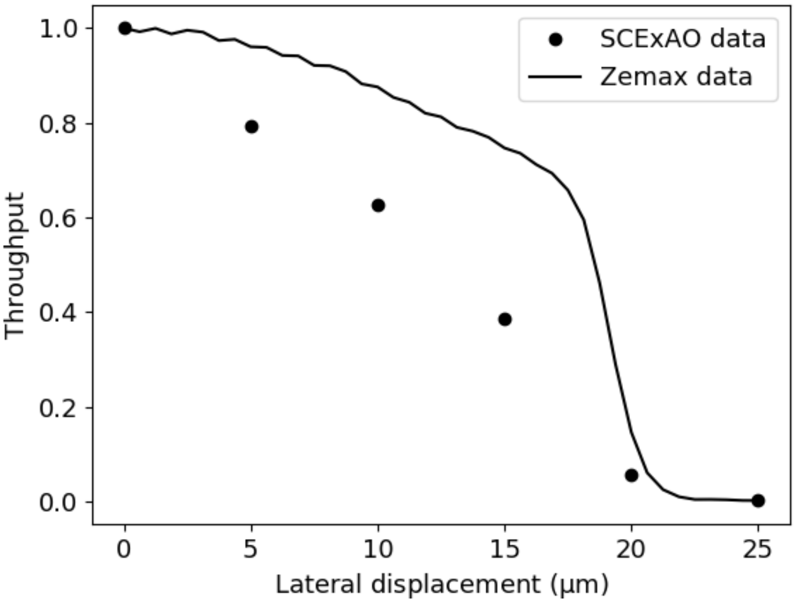

Figure 6.8: Throughput efficiency of the central core as a function of lateral displacement for SCExAO data compared to simulations from `Zemax`. Results are normalised to the maximum throughput and error-bars are smaller than the data points.

### 6.2.2 On-sky spectroscopic results

To evaluate the performance on-sky of the 3D-M3 instrument, it was tested on the night of 16th of October 2019 during a SCExAO engineering run. Thus, the true performance of the 3D printed IFU SM spectrograph was measured under real observing conditions. However, due to restrictions in available on-sky time, only one exposure of 8 min duration was captured at 6:00 (UTC-11) (see Figure 6.9). The conditions were less than ideal with below average atmospheric conditions (mean Seeing 0.62 high humidity >70%), telescope vibrations, and the wavefront sensor (WFS) being close to saturation on the bright test target. In addition to that, the rather high variable in direction wind-speed (16 km/h) was inducing vibrations to the telescope [1]. Thus the stabilisation and the shape of the beam coupled into the MLA facet were far from ideal (Lozi et al. 2018).

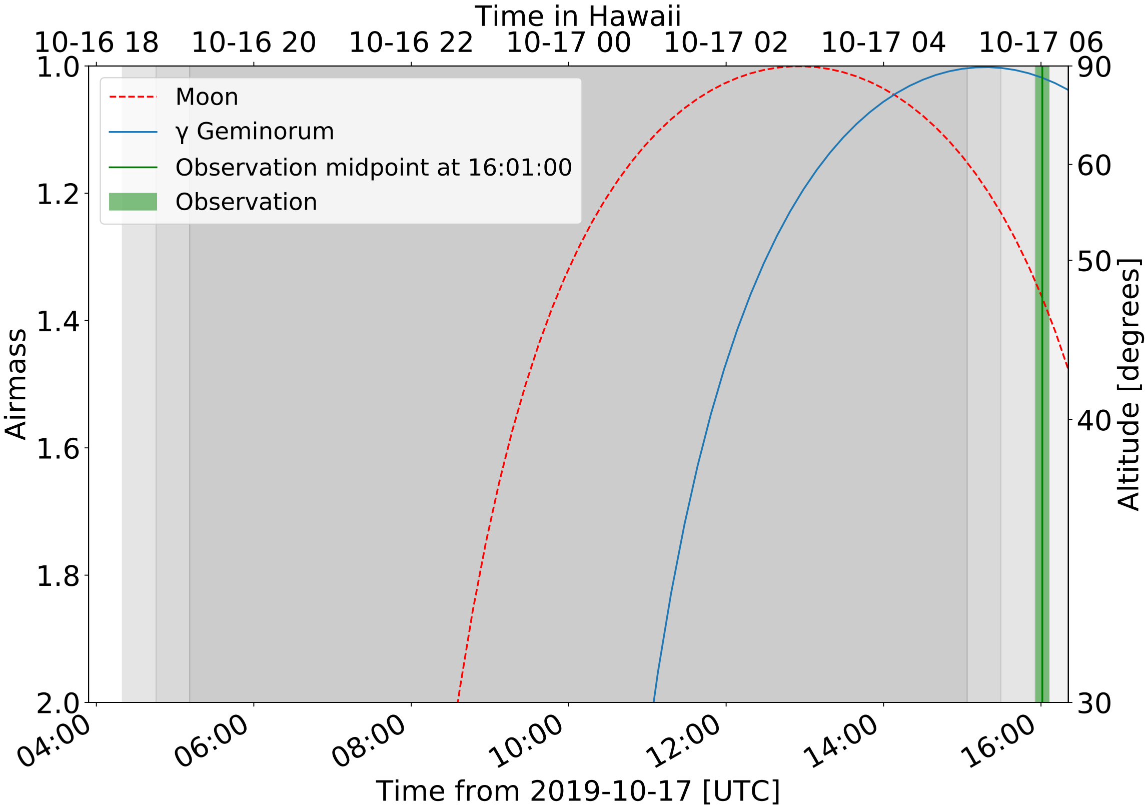

Figure 6.9: Illustration of time vs. airmass/altitude of the observation at 6:01 UTC -10 on the 17th of Oct. 2019 from Mauna Kea Observatory (green vertical region), for $\gamma$ Geminorum (solid blue line) and the moon (red dashed). Exposure started at the very end of observing time, close to sunrise.

---

[1] http://mkwc.ifa.hawaii.edu/current/seeing/?night=20191017&lastURLnight=20191017

As explained in Section 6.1.2, starlight from Subaru Telescope enters through the AO188 (Minowa et al. 2010) and then into the SCExAO instrument. With the intent of maximising the starlight coupling into the IFU, the PyWFS loop was closed and the PIAA optics deployed. Specifically, additional software modules that improve the sensitivity by predictive control applied on the PyWFS to remove resonances (Poyneer et al. 2014) and enhance the wavefront correction. In addition, PIAA optics apodize the injected beam as was the case for the laboratory experiments.

After the end of the observation, PSF data of the focal point of the injected beam were collected for $\sim$4 min in order to assess the on-sky conditions. However, the acquired data were from a non-common focal plane with the IFU, so there were expected non-common path errors to bias my measurement (see bottom left of Figure 6.2).

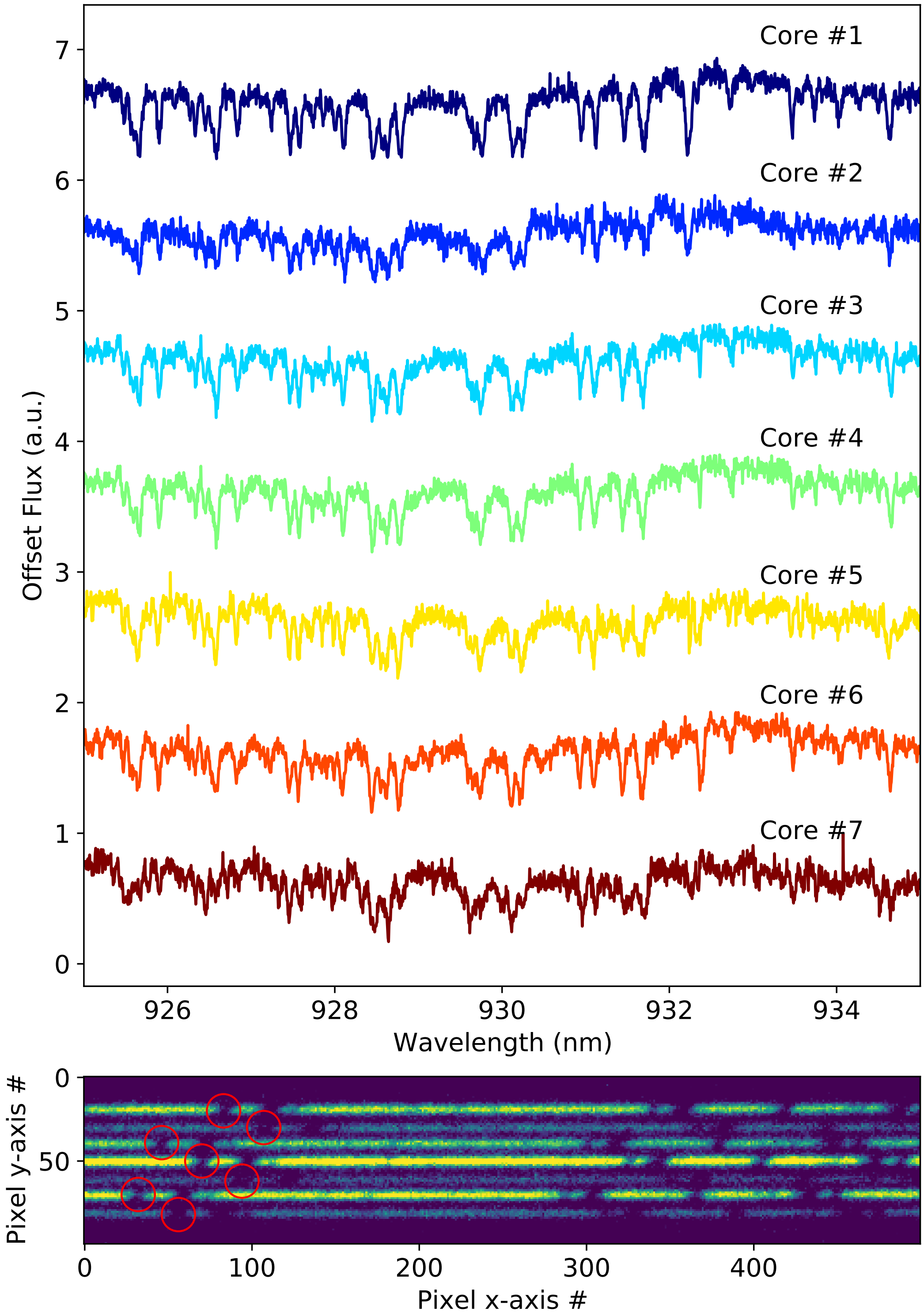

Figure 6.10: **Top panel:** Comparison spectra of $\gamma$ Geminorum from the 7 individual cores of the MCF at wavelength range of 925-935 nm where the many absorption features are visible. Each of the spectra is self-normalised and offset in respect to its intensity for clarity. **Bottom panel:** 2D detector image of a part of a spectral order from $\gamma$ Geminorum. Visible are all the 7 cores with sampled starlight. Notice the rotated pattern of the MCF formed by absorption features marked in red circles. On both axes numbers represent the detector pixels 4.8x4.8 µm.

The spectroscopic image data was acquired with the ASI-183MM-pro mono CMOS detector with an 8 min exposure time. For the spectroscopic analysis four types of data images were collected: 1) output data images were taken at the focal plane of the spectrograph, 2) dark frames that were used for the background subtraction of the the output data images, 3) bias frames for correction of the pixel-to-pixel variations and 4) flat frames for the output frames normalisation. Following the acquisition of data-images, the averaged dark and bias frames were subtracted from the output images to filter the detector noise background and abnormal (hot, dead) pixels and the averaged flat frames were used to normalise the final spectrum image data. The reduced frame is presented in Figure 6.11.

The resulting spectrum from this observation is illustrated in Figure 6.10 where only the spectrum of the range 925-935 nm is presented (900-950 nm is the full range) focusing on a narrow region where the spectral absorption features that are caused by the earth's telluric absorption lines are more intense. The target under observation was $\gamma$ Geminorum (HD 47105-Alhena), which is an A1.5IV+ spectral type sub-giant star in the constellation of Gemini and it is expected to be almost free of absorption features. The figure shows the spectra for all of the 7 cores individually. At the bottom panel of the figure, the 2D image of a part of the full spectrum is included. The hexagonal pattern of the MCF at optimal rotation appears as 7 lines for each order.

On the next step the spectra from each of the 7 cores were summed together in order to further increase the signal to noise ratio (SNR), representative of the case of a single unresolved star spectrum observation. The resulted combined spectrum is presented in Figure 6.12. The observed $\gamma$ Geminorum spectrum is represented with red colour and with blue colour the model spectrum for an $\gamma$ Geminorum-like star modeled from the PHOENIX spectral library (Husser et al. 2013) without the effect of earth's absorption spectral features. The observed spectrum appears quite noisy which is in part due to the forest of the absorption telluric features in the NIR wavelengths.

The coupling was only 6% of the expected value as shown in Figure 6.13 due to due to the poor wavefront correction because of the atmospheric conditions (variable wind of 16 km/h, 70% relative humidity, observing at the sunrise) and the wind causing vibrations of the telescope structure. Consequently, the injected starlight was not constant in position and shape (explained further below) and shifting around through all the 7 cores of the MCF. Thus, no spatial information was retained as the coupled PSF was not stable.

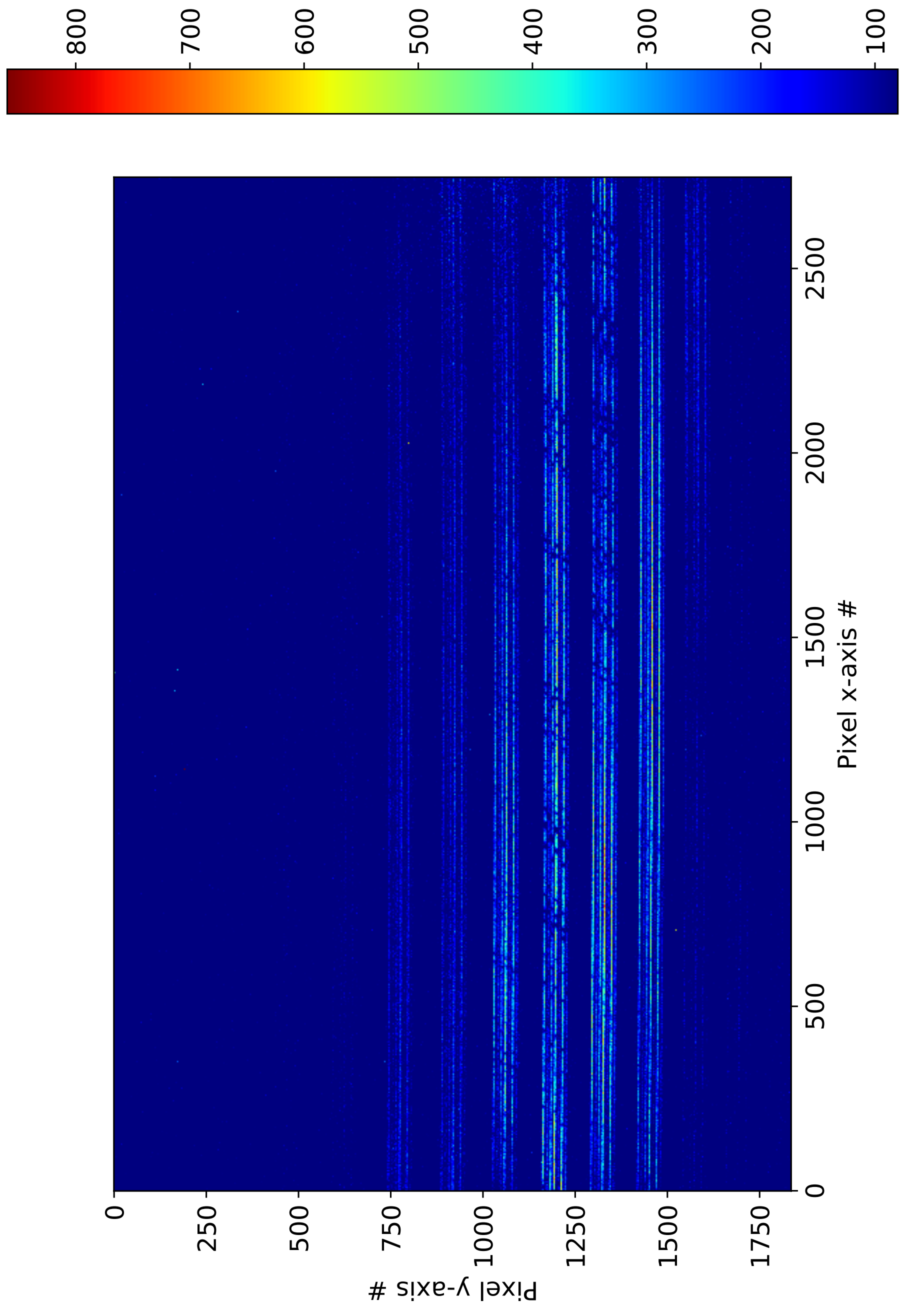

Figure 6.11: Full frame spectrum of $\gamma$ Geminorum.

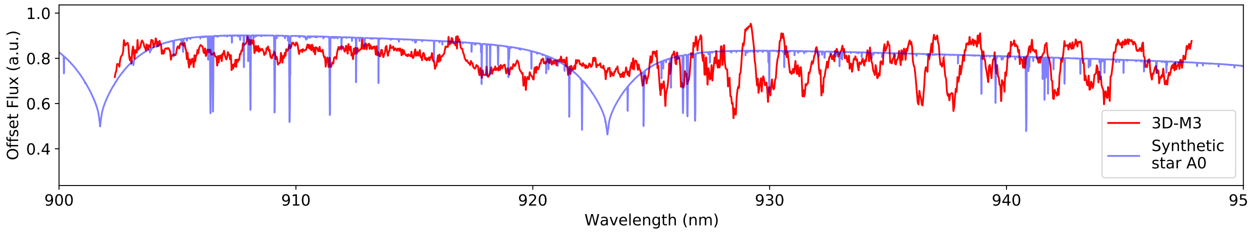

Figure 6.12: Full spectrum derived from the sum of all of the fiber cores observing $\gamma$ Geminorum overplotted against a PHOENIX synthetic star spectrum akin to the target (Husser et al. 2013). The observed spectrum is influenced by the numerous telluric lines of the earth while the synthetic spectrum has no influence of the them.

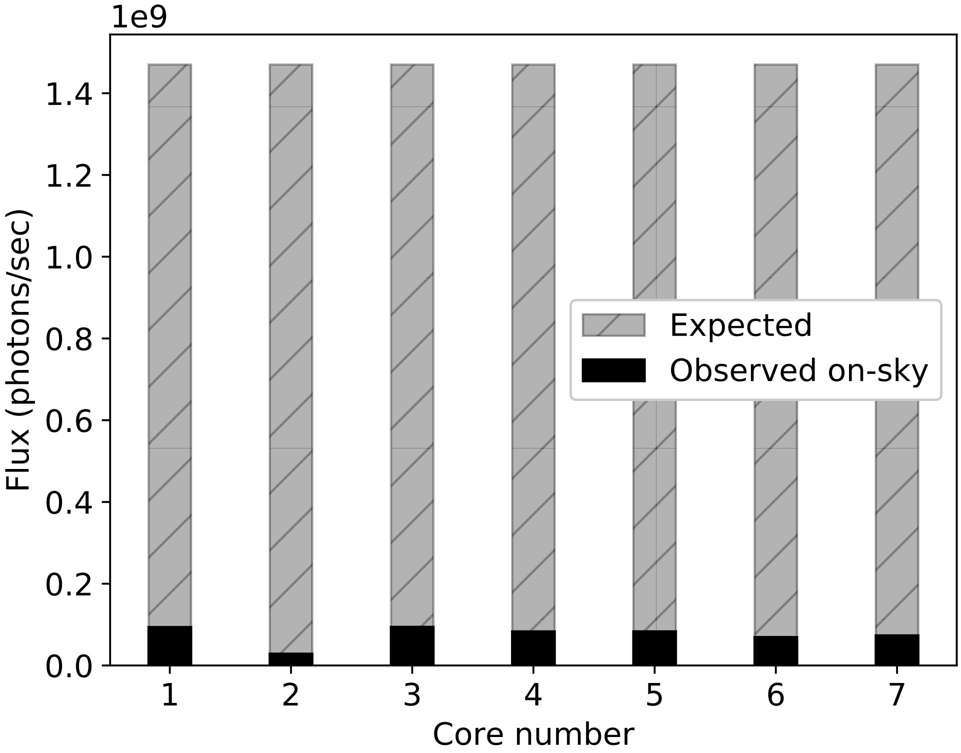

Figure 6.13: Flux performance of the 3D printed MCF as observed on-sky compared to the expected performance.

### 6.2.3 Adaptive optics performance

To quantify and evaluate the performance of the AO correction, the on-sky PSF profile data were captured as explained in section 6.2.2. The PSF was recorded in FITS format data-cubes composed of 1000 instantaneous frames each where the total exposure time of each data-cube was ~0.83 sec in total. For calibration purposes, additional PSF data-cubes were captured off-sky as well using the internal calibration source of SCExAO that follows the same optical path as the starlight (see centre left of Figure 6.2) and represents the case of an ideally shaped and stabilised target. Lastly, dark frames were collected for background current subtraction.

Initially, each of the 1000 frames into the data-cubes, for off an on-sky data, were dark current subtracted and averaged. After this, the ratio of the maximum intensity ($I\mathrm{max}$) to 90% of corresponding flux ($Flux$) was calculated and stores for all of the data. To approximate the Strehl ratio during the observation time, the stored maximum to flux ratios for each data-set (off and on-sky) were divided; this results in

$$S = \frac{I\mathrm{max}_{\mathrm{on-sky}}}{Flux_{\mathrm{on-sky}}} \frac{Flux_{\mathrm{off-sky}}}{I\mathrm{max}_{\mathrm{off-sky}}}. \tag{6.1}$$

The result of the calculation was $S$=0.2, representing an estimation of the Strehl on-sky. In the next step, the averaged intensity of an averaged data-cube was over-plotted along with its Gaussian fit. This was done for the laboratory PSF data as well. The resulted profile and fit are presented in Figure 6.14. On the top panel of the figure the normalised intensity profile of the averaged on-sky data along one axis, its Gaussian fit and the profile from the laboratory ideal beam measurements were plotted together. On the bottom panels the 2D image of the on-sky PSF is plotted in linear and logarithmic scale for better clarity.

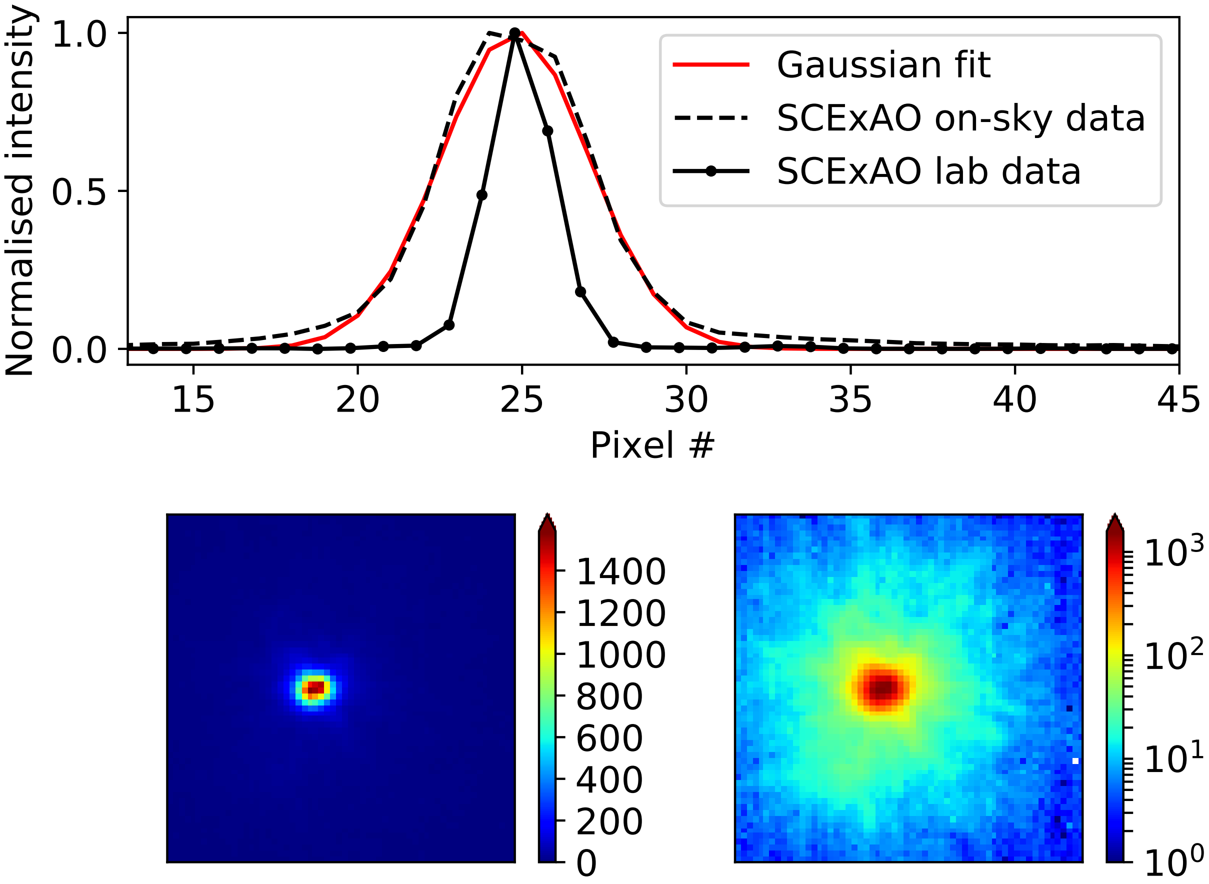

Figure 6.14: **Top panel:** Intensity line profile of the apodized injected point spread function normalised to its peak using the Phase-Induced Amplitude Apodization optics, for the on-sky and laboratory data. A Gaussian fit was performed on the on-sky data. **Bottom panel:** 2D image of the PSF in linear (left) and logarithmic (right) colour scale for better clarity. The exposure time was ∼0.83 sec.

Following that, the 1000 data images from each data-cube of the on-sky data, were averaged per data-cube. Afterwards, the centre of mass for each of them was calculated. In addition to that, the ratio of the on-sky to the laboratory beam FWHM was calculated as a function of time evolution through the exposure to visualise the beam's diameter deformation as experienced on-sky. Results are presented in Figure 6.15; they suggest that the on-sky's beam centre of mass shift was rather big where the FWHMs of the on-sky and the laboratory beam were over-plotted to manifest that the on-sky was twice as large in size compared to the laboratory one as illustrated on the bottom panel. Consequently, the position stability of the PSF was not representative of the SCExAO system performance but it was a consequence of the atmospheric conditions mentioned in section 6.2.2 and the time of the observation.

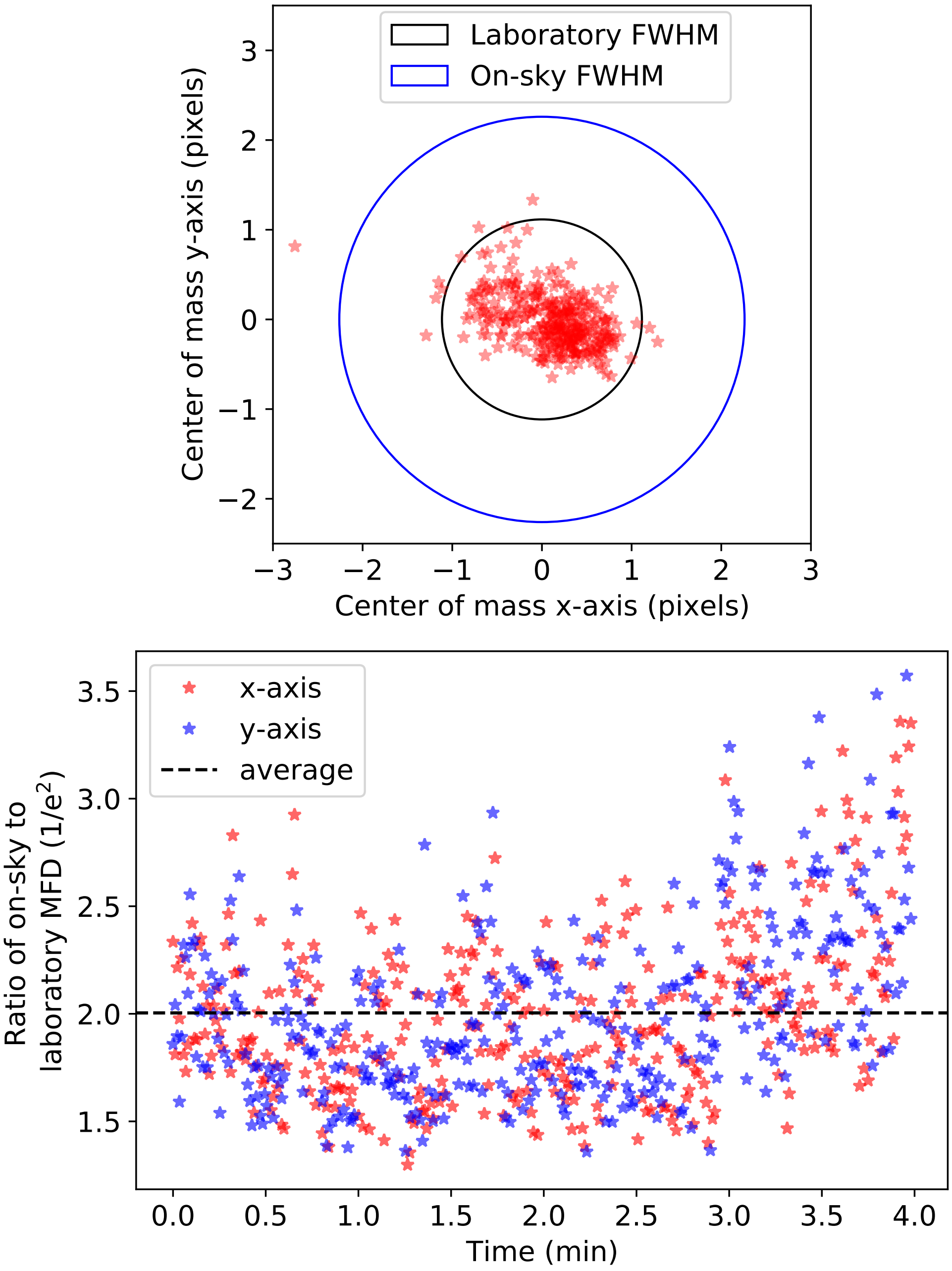

Figure 6.15: **Top sub-figure:** Centre of mass shift of the on-sky beam during the observation. Over-plotted with two circles are the FWHM of the on-sky beam and the laboratory, over time right after the time of observation. The average is represented with the black dashed line. **Bottom sub-figure:** The ratio of on-sky to the laboratory FWHM on both detector axes over time.

## 6.3 Discussion

### 6.3.1 Opto-mechanical parts limitations

The short on-sky run of 3D-M3 proved to work reasonably well considering the observation conditions as well as the non-optimised components, manifesting a SM-IFS with high-resolving power at NIR wavelengths.

A few key areas need improvement for future iterations. The selected detector ASI-183 (mono) CMOS camera model from ZWO had low efficiency. Its rather large detector size of 20.18 Mega pixels with a 2.4 µm pixel-to-pixel pitch was outweighed by the low quantum efficiency (QE) performance ($\leq$15% of the IMX 183 sensor in the 900-1000 nm wavelength regime. In addition to this, amp glow[2] was present for exposures longer than one minute, making spectrum calibration difficult. The efficiency losses were compounded by the non-optimal anti-reflective coating of the lenses and the efficiency of the cross dispersing transmission grating. All this is due to my approach to assemble an inexpensive benchtop spectrometer with commercial off-the-shelf (COTS) components, for a proof of concept observation run. Using custom made optics with coatings optimised for our wavelength range, as well as employing a detector with larger pixels and higher quantum efficiency at red wavelengths is a straight-forward, if costly, next step. Nonetheless, the successful demonstration of our MCF IFU concept on-sky is a critical step towards implementing a more efficient spectrometer in the near future.

## 6.4 Conclusions

In this study I accomplished the first technology demonstration of a high-resolution diffraction-limited integral field spectrograph, namely the 3D-M3. It utilises a custom MCF with 3D printed micro-optics on top of its cores in order to increase the coupling efficiency of starlight from SCExAO@Subaru 8.2 m telescope while the the spatial information of the input is retained.

The injection MCF system is optimised for an on-sky angular dimension of 54 mas using the output beam profile of the SCExAO@Subaru telescope that make use of PIAA optics shaping the output PSF to a near Gaussian profile.

---

[2] https://astronomy-imaging-camera.com/tutorials/what-is-amp-glow.html

The MCF had a SM cut-off limit at ∼ 800 nm and was composed of 19 SM cores in a hexagonal formation, with a pitch of 40 µm and a 5.3 µm MFD @980 nm ($1/e^2$) with a negligible cross-coupling between the neighbouring cores. The SM spectrograph's compact footprint is 300 × 600 mm; it was made completely out of-the-self parts providing a resolving power of ∼30,000 at 1 µm.

The MCF was directly 3D printed using two-photon lithography, considerably improving the coupling of light to each of the fiber's cores from a few percent levels up to a theoretical maximum of 48.8% with the MLA. In addition to this, the mis-alignment tolerances of the injected beam were relaxed with this method, performing reasonably well even for a lateral ∼18 µm off-axis injection.

The throughput results on SCExAO confirm the theoretical expectation. A maximum of 40.7% of throughput per core was achieved (value corresponding to 83% of the theoretical value) reaching an average of 35.8% per-core. The throughput performance of the 3D printed fiber across all the 7 lenslets of it, representing the case of a single unresolved target was measured at 70% (value corresponding to ∼85% of the theoretical value). The difference between the theoretical and measured values is likely due to the manufacturing errors as well as the polishing of the fiber's facets. These results were obtained with SCExAO and an artificial light source, which closely represents the performance of the facility under good observing conditions. A short on-sky suffered from windshake and bad seeing, resulting in lower throughout of less than 1% compared to the laboratory measurements.

The results suggest that SM astrophotonic technologies are mature enough to operate on 8-m class telescopes with ExAO systems and the opportunity exists to harnesses their potential, accuracy and precision over MM technologies. Even though, the system met the expectations and performed reasonably well given the given conditions, the results highlight the importance of correct on-sky conditions for the system to work properly.

Aims for future work include further optimisation of the optical design, by performing more simulations using `Zemax`, replacing the spectrometer optics with custom build ones using wavelength appropriate coatings, and investing in the stabilisation of the instrument with enclosures and controls.

Observation aims for the future involve a target list with a variety of targets (resolvable star, non-resolvable, double star system, massive confirmed exoplanets, spectroscopic standard stars) for evaluating its science potential.

# Chapter 7

# Conclusions and future work

In this thesis I investigated the potential of astrophotonic components within astronomical instrumentation using modelling and experimentation. In this chapter an overview of the previous chapters is provided commenting on the impact of this study within the field, ending with further potential areas of improvement.

## 7.1 Synopsis

In the beginning I introduced the necessary theory of conventional spectroscopy including the astrophotonics view point. I began with a description of the most common astronomical instrumentation techniques used to date, and following with an introduction to the field of astrophotonics including its most commonly-used component, the fiber waveguide. Lastly, relevant work from the literature of astrophotonic spectroscopy was presented. The introduction is based on the existing literature.

Following that, I presented a study on simulating the performance of an astrophotonic component named the photonic dicer, tested previously on-sky. Through geometrical re-designing of the reformatter, the throughput and noise properties of the component were explored and optimised using two sophisticated simulation tools in conjunction. The simulation results complemented well the on-sky performance while a further geometrical optimisation improved its throughput by 6.4%. Simulation results indicate that there is modal noise in the photonic dicer; however, three orders of magnitude less compared to a standard multi-mode fiber. This chapter is largely drawn from Anagnos et al. (2018a).

In the next step, I used the developed technique from the previous chapter to optimise the hybrid reformatter. This is a previously optimised version of the photonic dicer tested on-sky. In the optimisation I examined various parameters of these astrophotonic devices for making them more efficient for conventional high resolving power spectrographs to suit astronomical observations. Results are in agreement with literature, however, I achieved a 6% optimisation of its performance. It is largely drawn from Anagnos et al. (2018b).

Afterwards, I performed the lab characterisation of a variety of astrophotonic reformatters in the visible wavelengths inscribed in two glass substrates using the ultra-fast laser inscription technique. These were manufactured by Optofab at Macquarie University. The chips include twenty-two different inscribed waveguide geometries for two different pulse laser energy inscription parameters. Laboratory throughput measurement showed a maximum throughput of 14.4%. Results suggest that astrophotonic reformatters in the visible wavelength regime using the ultra-fast laser inscription inscription technique are considerably lower in throughput performance than their near infrared counterparts. This section is about to be published in Anagnos et al. (2020b, in prep.).

Finally, I harnessed the knowledge gathered from previous chapters and presented the design and manufacture of a custom astrophotonic component. This is a combination of 3D printed micro-lenses on top of a custom multi-core fiber aiming to optimise the throughput and coupling into the cores of the fiber while feeding a compact-size close-to diffraction-limit spectrograph. The instrument was tested on-sky at the Subaru 8.2 m telescope and Subaru Coronagraphic Extreme Adaptive Optics facility. The maximum throughput results in laboratory environment for the integral field unit were found to be 40.7% per core, while the throughput across all the lenslets when the target was an unresolved star was measured to be 70%. Both throughput results are ∼83% of the simulated performance. I am in the process of publishing the results of this chapter in Anagnos et al. (2020a, MNRAS, in prep.).

To summarise, in this thesis I presented the theoretical performance and laboratory results showing the capabilities and the limitations of multiple astrophotonic reformatters both in the visible and near infrared wavelength regime. Additionally, I describe the implementation of a novel high resolution spectrograph concept and show first on-sky results of such an instrument equipped with novel astrophotonic parts such as 3D printed micro-optics on top of a custom multi-core fiber.

## 7.2 Further Work

Aims for future work with respect to astrophotonic reformatters at visible wavelengths involve an investigation on selecting better performing optical substrate materials in conjunction with the ultrafast laser inscription inscription technique. Once the optimal combination of substrate materials with laser inscription parameters has been established to generate low-loss devices, the next step is to manufacture reformatters with these characteristics and permanently integrate them with fibers to transfer the light from the focal point of the telescope to the spectrograph. After that, on-sky observations of spectroscopic standard targets can be obtained to evaluate the actual performance of the concept.

Future activities for improving the 3D-printed Mono-Mode Multi-core fiber spectrograph instrument include the optimisation of the instrument's optical design using custom optics with appropriate coatings for the wavelength range, and investing in the environmental stabilisation of the instrument with hermetic enclosures and active temperature and pressure control. Plans for future observing runs involve a target list with a variety of targets (resolvable star, non-resolvable, double star system, massive confirmed exoplanets, spectroscopic standard stars) for evaluating the potential of our instrument concept to enable new discoveries at the highest spatial and spectral resolution attainable today.

# Bibliography

Agapito G., Arcidiacono C., Quirós-Pacheco F., Esposito S., 2014, Experimental Astronomy, 37, 503

Allington-Smith J., 2006, New A Rev, 50, 244

Allington-Smith J., 2007, Science Perspectives for 3D Spectroscopy, pp 3–13

Allington-Smith J., Content R., 1998, Publications of the Astronomical Society of the Pacific, 110, 1216

Anagnos T., et al., 2018a, MNRAS, 478, 4881

Anagnos T., et al., 2018b, Proc.SPIE, 10706, 10706

Arriola A., Gross S., Jovanovic N., Charles N., Tuthill P. G., Olaizola S. M., Fuerbach A., Withford M. J., 2013, Opt. Express, 21, 2978

Bacon R., et al., 1995, A&AS, 113, 347

Barden S. C., 1998, Fiber Optics in Astronomy III, ASP Conference Series, 152, 14

Barden S. C., Ramsey L. W., Truax R. J., 1981, Publications of the Astronomical Society of the Pacific, 93, 154

Bechter A., et al., 2016, Proc SPIE, 9909, 99092X

Bechter A. J., Crass J., Tesch J., Crepp J. R., Bechter E. B., 2020, PASP, 132, 015001

Bilodeau F., Hill K., Faucher S., Johnson D., 1988, Optical Fiber Sensors, p. ThCC10

Birks T. A., Mangan B. J., Díez A., Cruz J. L., Murphy D. F., 2012, Optics Express, 20, 13996

Birks T. A., Gris-Sánchez I., Yerolatsitis S., Leon-Saval S. G., Thomson R. R., 2015, Adv. Opt. Photon., 7, 107

Bland-Hawthorn J., Kern P., 2009, Opt. Express, 17, 1880

Bland-Hawthorn J., Buryak A., Kolossovski K., 2008, J. Opt. Soc. Am. A, 25, 153

Bland-Hawthorn J., et al., 2011, Nature Communications, 2, 581

Bouchy F., Díaz R. F., Hébrard G., Arnold L., Boisse I., Delfosse X., Perruchot S., Santerne A., 2013, A&A, 549, A49

Brown D. M., et al., 2014, Proc. SPIE, 9151, 426

Bryant J. J., et al., 2016, Proc SPIE, 9908, 99081F

Chang D. H., Azfar T., Kim S.-K., Fetterman H. R., Zhang C., Steier W. H., 2003, Opt. Lett., 28, 869

Chen C.-H., Reynolds R. O., Kost A., 2006, Appl. Opt., 45, 519

Coudé du Foresto V., Ridgway S. T., 1992, European Southern Observatory Conference and Workshop Proceedings, 39, 731

Coudé du Foresto V., Faucherre M., Hubin N., Gitton P., 2000, A&AS, 145, 305

Courtes G., 1982, IAU, 92, 123

Crepp J. R., et al., 2016, Proc SPIE, 9908, 990819

Croom S. M., et al., 2012, MNRAS, 421, 872

Cvetojevic N., Lawrence J. S., Ellis S. C., Bland-Hawthorn J., Haynes R., Horton A., 2009, Opt. Express, 17, 18643

Cvetojevic N., Jovanovic N., Lawrence J., Withford M., Bland-Hawthorn J., 2012, Opt. Express, 20, 2062

Cvetojevic N., et al., 2017, Opt. Express, 25, 25546

Davis K. M., Miura K., Sugimoto N., Hirao K., 1996, Opt. Lett., 21, 1729

Dekany R., et al., 2013, ApJ, 776, 130

Dietrich P.-I., et al., 2016, Conference on Lasers and Electro-Optics, p. SM1G.4

Dietrich P.-I., Harris R. J., Blaicher M., Corrigan M. K., Morris T. J., Freude W., Quirrenbach A., Koos C., 2017, Opt. Express, 25, 18288

Dietrich P.-I., et al., 2018, Nature Photonics, 12, 241

Eaton S. M., Zhang H., Herman P. R., Yoshino F., Shah L., Bovatsek J., Arai A. Y., 2005, Opt. Express, 13, 4708

Feger T., Brucalassi A., Grupp F. U., Lang-Bardl F., Holzwarth R., Hopp U., Bender R., 2012, Proc. SPIE, 8446, 844692

Feger T., et al., 2014, Proc. SPIE, 9147, 91477I

Fontaine N. K., Ryf R., Bland-Hawthorn J., Leon-Saval S. G., 2012, Opt. Express, 20, 27123

Fuhrmeister, B. et al., 2019, A&A, 632, A24

Ge J., Angel J. R. P., Shelton J. C., 1998, Proc SPIE, 3355, 253

Ghasempour A., Kelly J., Muterspaugh M. W., Williamson M. H., 2012, Proc SPIE, 8450, 845045

Gissibl T., Thiele S., Herkommer A., Giessen H., 2016, Nature Photonics, 10, 554

Glezer E. N., Milosavljevic M., Huang L., Finlay R. J., Her T. H., Callan J. P., Mazur E., 1996, Optics Letters, 21, 2023

Gottlieb D., Shu C.-W., 1997, SIAM Review, 39, 644

Gurevich Y. V., Stürmer J., Schwab C., Führer T., Lamoreaux S. K., Quirrenbach A., Walther T., 2014, Proc SPIE, 9147, 91477M

Guyon O., et al., 2020, American Astronomical Society, 51, 280.06

Halverson S., Roy A., Mahadevan S., Schwab C., 2015, ApJ, 814, L22

Harris R. J., et al., 2015, MNRAS, 450, 428

Harris R. J., Labadie L., Lemke U., MacLachlan D. G., Thomson R. R., Reffert S., Quirrenbach A., 2016, Proc. SPIE, 9912, 1722

Hayano Y., et al., 2008, Proc SPIE, 7015, 701510

Hayano Y., et al., 2010, Proc SPIE, 7736, 77360N

Hecht E., 2002, Optics. Addison-Wesley

Hill J. M., 1988, Fiber Optics in Astronomy (San Francisco: ASP), 3, 77

Hill J. M., Angel J. R. P., Scott J. S., Lindley D., Hintzen P., 1980, ApJ, 242, L69

Hottinger P., et al., 2018, Proc. SPIE, 10706, 1070629

Husser T. O., Wende-von Berg S., Dreizler S., Homeier D., Reiners A., Barman T., Hauschildt P. H., 2013, A&A, 553, A6

Iuzzolino M., Tozzi A., Sanna N., Zangrilli L., Oliva E., 2014, Proc. SPIE, 9147, 914766

Jovanovic N., et al., 2012, MNRAS, 427, 806

Jovanovic N., et al., 2015, PASP, 127, 890

Jovanovic N., et al., 2017, A&A, 604, A122

Karovska M., de Val-Borro M., Hack W., Raymond J., Sasselov D., Lee N. P., 2011, AAS, 218, 228.03

Khouri T., 2018, Proceedings of the ESO Garching conference, p. 17

Le Bouquin, J.-B. et al., 2011, A&A, 535, A67

Le Coarer E., et al., 2007, Nature Photonics, 1, 473

Lemke U., Corbett J., Allington-Smith J., Murray G., 2011, MNRAS, 417, 689

Leon-Saval S. G., Birks T. A., Bland-Hawthorn J., Englund M., 2005, Optics Letters, 30, 2545

Leon-Saval S. G., Betters C. H., Bland-Hawthorn J., 2012, Proc. SPIE, 8450, 84501K

Leon-Saval S. G., Argyros A., Bland-Hawthorn J., 2013, Nanophotonics, 2, 429

Lobel A., Dupree A. K., Gilliland R. L., 1999, American Astronomical Society Meeting Abstracts, 195, 45.03

Lobel A., Aufdenberg J., Dupree A. K., Kurucz R. L., Stefanik R. P., Torres G., 2004, IAU Symposium, 219, 641

Love J. D., 1987, Electronics Letters, 23, 993

Lozi J., Martinache F., Guyon O., 2009, PASP, 121, 1232

Lozi J., et al., 2018, Journal of Astronomical Telescopes, Instruments, and Systems, 4, 049001

MacLachlan D. G., Harris R., Choudhury D., Arriola A., Brown G., Allington-Smith J., Thomson R. R., 2014, Proc. SPIE, 9151, 91511W

MacLachlan D. G., et al., 2017, MNRAS, 464, 4950

Macintosh B., et al., 2014, Proceedings of the National Academy of Science, 111, 12661

Marcuse D., 1974, Theory of Dielectric Optical Waveguides. Academic Press, New York

Marcuse D., 1977, AT T Technical Journal, 56, 703

Marcuse D., 1989, Light Transmission Optics. Krieger Pub Co.

Marcy G. W., Butler R. P., 1992, PASP, 104, 270

Massey P., Hanson M. M., 2013, Planets, Stars and Stellar Systems. Volume 2: Astronomical Techniques, Software and Data, p. 35

McCoy K. S., Ramsey L., Mahadevan S., Halverson S., Redman S. L., 2012, Proc. SPIE, 8446, 84468J

Meany T., Gross S., Jovanovic N., Arriola A., Steel M. J., Withford M. J., 2014, Applied Physics A: Materials Science & Processing, 114, 113

Menlo Systems GmbH 2020, C-Fiber 780 Femtosecond Erbium Laser, `https://www.menlosystems.com/products/femtosecond-lasers-and-amplifiers/c-fiber-780/`

Minowa Y., et al., 2010, Proc SPIE, 7736, 77363N

Moehler, S. et al., 2014, A&A, 568, A9

Myers R. M., et al., 2008, Proc. SPIE, 7015, 70150E

Nanoscribe GmbH 2018, IP Photoresists, `http://www.nanoscribe.de/en/products/ip-photoresists/`

Nasu Y., Kohtoku M., Hibino Y., 2005, Opt. Lett., 30, 723

Noordegraaf D., Skovgaard P. M. W., Nielsen M. D., Bland-Hawthorn J., 2009, Opt. Express, 17, 1988

Noordegraaf D., Skovgaard P. M. W., Maack M. D., Bland-Hawthorn J., Haynes R., Lægsgaard J., 2010, Opt. Express, 18, 4673

Norris B. R. M., et al., 2012, Nature, 484, 220

Ohnaka K., 2009, Mem Soc Astron Italiana, 80, 715

Ohnaka K., Morales Marín C. A. L., 2018, A&A, 620, A23

Okamoto K., 2010, Fundamentals of Optical Waveguides. Elsevier Science

Olaya J.-C., Leon-Saval S. G., Schirdewahn D., Ehrlich K., Haynes D. M., Haynes R., 2012, MNRAS, 427, 1194

OptiBPM 2020, Optiwave Systems Inc., `https://optiwave.com/`

Parry I., 1998, Fiber Optics in Astronomy III ASP Conference Series, 152, 3

Parry I. R., 2006, New Astronomy Reviews, 50, 301

Peacock A., et al., 1996, Nature, 381, 135

Perruchot S., et al., 2011, Proc. SPIE, 8151, 815115

Petersburg R. R., McCracken T. M., Eggerman D., Jurgenson C. A., Sawyer D., Szymkowiak A. E., Fischer D. A., 2018, The Astrophysical Journal, 853, 181

Picqu N., Hnsch T. W., 2019, Nature Photonics, 13, 146157

Poyneer L. A., et al., 2014, Proc. SPIE, 9148, 166

Radder A. C., 1979, Journal of Fluid Mechanics, 95, 159176

Rains A. D., et al., 2016, Proc SPIE, 9908, 990876

Ramsey L. W., 1988, IN: Fiber optics in astronomy; Proceedings of the Conference, 3, 26

Ramstedt S., et al., 2014, A&A, 570, L14

Raskin, G. et al., 2011, A&A, 526, A69

Rawson E. G., Goodman J. W., Norton R. E., 1980, J. Opt. Soc. Am., 70, 968

Reeves A., 2016, Proc. SPIE, 9909, 99097F

Roey J. V., van der Donk J., Lagasse P. E., 1981, J. Opt. Soc. Am., 71, 803

Romani R. W., Miller A. J., Cabrera B., Figueroa-Feliciano E., Nam S. W., 1999, The Astrophysical Journal, 521, L153

Snyder A., Love J., 1984, Optical Waveguide Theory. Springer US

Spaleniak I., Jovanovic N., Gross S., Ireland M. J., Lawrence J. S., Withford M. J., 2013, Optics Express, 21, 27197

Spaleniak I., et al., 2016, Proc. SPIE, 9912, 991228

Synopsys 2018, RSoft Photonic System Design Suite Version 2017.03, `https://optics.synopsys.com/rsoft/`

Szypryt P., 2017, PhD thesis, University of California, Santa Barbara

Tamir T., Garmire E., Hammer J., Kogelnik H., Zernike F., 2013, Integrated Optics. Topics in Applied Physics, Springer Berlin Heidelberg

Tamura M., et al., 2012, Proc SPIE, 8446, 84461T

Thomson R. R., Kar A. K., Allington-Smith J., 2009, Optics Express, 17, 1963

Thomson R. R., Brown G., Kar A. K., Birks T. A., Bland-Hawthorn J., 2010, Frontiers in Optics 2010/Laser Science XXVI, p. PDPA3

Thomson R., Birks T., Leon-Saval S., Kar A., Bland-Hawthorn J., 2011, Optics Express, 19, 5698

Tozzi A., et al., 2018, Proc SPIE, 10702, 107028Q

Tremblay Y., Kawasaki B. S., Hill K. O., 1981, Appl. Opt., 20, 1652

Trinh C. Q., et al., 2013, The Astronomical Journal, 145, 51

Tsuji T., 2008, A&A, 489, 1271

Vigan A., et al., 2016, A&A, 587, A55

Vlemmings W. H. T., Ramstedt S., O'Gorman E., Humphreys E. M. L., Wittkowski M., Baudry A., Karovska M., 2015, A&A, 577, L4

Watson F. G., 1995, Proc.SPIE, 2476, 2476

Wikipedia 2019, Transverse mode — Wikipedia, The Free Encyclopedia, `http://en.wikipedia.org/w/index.php?title=Transverse%20mode&oldid=895527773`

Wood B. E., Harper G. M., Mueller H.-R., 2019, Spatially Resolving the Winds of Red Giant Stars, HST Proposal

Zemax 2016, OpticStudio - Zemax, `http://www.zemax.com/os/opticstudio`

Zuiderwijk E. J., Knapen J., 1989, A spectral atlas of calibration lamps in use with the INT IDS, Technical Note 70 (Santa Cruz de la Palma)